

DEMOGRAPHICS AND PHYSICAL PROPERTIES OF GAS OUT/INFLOWS AT $0.4 < Z < 1.4$ CRYSTAL L. MARTIN¹ ALICE E. SHAPLEY^{2,8} ALISON L. COIL^{3,9} KATHERINE A. KORNEI² KEVIN BUNDY⁴ BENJAMIN J. WEINER⁵ KAI G. NOESKE⁶ DAVID SCHIMINOVICH⁷*Draft version October 19, 2019*

ABSTRACT

We present Keck/LRIS spectra of over 200 galaxies with well-determined redshifts between 0.4 and 1.4. We combine new measurements of near-ultraviolet, low-ionization absorption lines with previously measured masses, luminosities, colors, and star formation rates to describe the demographics and properties of galactic flows. Among star-forming galaxies with blue colors, we find a net blueshift of the Fe II absorption greater than 200 km s^{-1} (100 km s^{-1}) towards 2.5% (20%) of the galaxies. The fraction of spectra with blueshifts decreases significantly among galaxies with specific star formation rates less than roughly 0.8 Gyr^{-1} and does not vary significantly with stellar mass, color, or luminosity. The insensitivity of the blueshifted fraction to galaxy properties favors collimated outflows, and in this context we demonstrate how the solid angle of the outflow declines with increasing outflow velocity. We also detect enriched infall towards 3-6% of the galaxies, apparently observed at an optimal viewing angle. At least 3 (1) of the 9 infalling streams have a large cross section and velocities commensurate with an extended disk (satellite galaxy). We explain the strong dependence of the Mg II absorption equivalent width on stellar mass, *B*-band luminosity, and *U* – *B* color by resonance emission partially filling in the intrinsic absorption troughs; emission filling can also explain the significant differences often observed between the shape of the Mg II line profile and the absorption troughs of those Fe II transitions that decay primarily by fluorescence. This study provides a new quantitative understanding of gas flows between galaxies and the circumgalactic medium over a critical period in galaxy evolution.

Subject headings:

1. INTRODUCTION

Key processes in the evolution of galaxies include the flow of cool gas into galaxies, the conversion of these baryons into stars, and the ejection of gas enriched with heavy elements. Determining the factors that govern the circulation of baryons remains a critical, unsolved problem in cosmology.

The measured properties of galaxies indicate strong evolution in this baryon cycle between the peak in star-formation activity at redshift $z \approx 2$ and the current epoch (Lilly et al. 1996; Madau et al. 1996; Hopkins & Beacom 2006). At any redshift during this period, star-forming galaxies populate a fairly well-defined locus in the star formation rate (SFR) – stellar mass plane (Bell et al. 2005; Elbaz et al. 2007; Noeske et al. 2007). However, the observed SFR at a fixed stellar mass declines by about a factor of 20 from $z \sim 2$ to the present. The Tully-Fisher relation also evolves in the sense that present-day galaxies have about 2.5 times more stellar mass than do

galaxies at $z \approx 2.2$ with the same circular velocity (Cresci et al. 2009). Since redshift $z \approx 1$ when roughly half the mass in present-day galaxies was assembled (Drory et al. 2005; Faber et al. 2007; Marchesini et al. 2009), the stellar mass in red sequence galaxies has continued to grow; but the mass in blue galaxies has remained essentially constant (Faber et al. 2007). Over this period, some process quenches star formation in massive galaxies, yet observational efforts to identify this process with feedback from active galactic nuclei (AGN) have not reached a consensus (cf., Schawinski et al. 2007; Aird et al. 2012).

The leading explanation for this drop in cosmic star-formation activity is a decline in the accretion rate of cool gas onto galaxies. The simplest form of this idea, that the mean growth rate of dark matter halos regulates the gas inflow rate onto galaxies, fails; it yields too much star formation in low mass halos at early times (Bouché et al. 2010) and does not shut down star formation in high mass halos at later times (Somerville et al. 2008). Introducing gas physics – heating by virial shocks in massive halos *and* outflows in both low-mass and high-mass halos – effectively tilts the underlying relationship between halo accretion rate and mass (described by the simplest model) into the observed SFR – stellar mass relation and Tully-Fisher relation (Bouché et al. 2010; Davé, Oppenheimer, & Finlator et al. 2011a; van de Voort et al. 2011a, b; Davé, Finlator, & Oppenheimer 2012). The balance between gas outflow and inflow then determines the relationship between the gas-phase metallicity and stellar mass (Davé, Finlator, & Oppenheimer 2011b). The problem with this scenario is that this baryon-driven picture of galaxy formation rests on a rather rudimentary understanding of which galaxies have outflows and in-

¹ Department of Physics, University of California, Santa Barbara, CA, 93106, cmartin@physics.ucsb.edu

² Department of Physics and Astronomy, University of California, Los Angeles, CA, 90025

³ Center for Astrophysics and Space Sciences, Department of Physics, University of California, San Diego, CA 92093

⁴ Kavli Institute for the Physics and Mathematics of the Universe, Todai Institutes for Advanced Study, University of Tokyo, Kashiwa, Japan 277-8583 (Kavli IPMU, WPI)

⁵ Steward Observatory, 933 N. Cherry St., University of Arizona, Tucson, AZ 85721, USA

⁶ Space Telescope Science Institute, Baltimore, MD 21218, USA

⁷ Department of Astronomy, Columbia University, New York, NY 10027, USA

⁸ Packard Fellow

⁹ Alfred P. Sloan Fellow

flows and how the physical properties of flows vary with fundamental galaxy properties.

Gas flows imprint resonance absorption lines on the spectra of their host galaxies that can often be kinematically distinguished from interstellar gas at the systemic velocity (Heckman et al. 2000; Schwartz & Martin 2004; Martin 2005, 2006; Rupke et al. 2005; Schwartz et al. 2006; Tremonti et al. 2007; Martin & Bouché 2009; Rubin et al. 2010a). Thus far, studies of gas flows at $0.5 < z < 2$ have either been based on just a few individual galaxies (Sato et al. 2009; Coil et al. 2011; Rubin et al. 2011) or on *composite spectra*, i.e., the average of many low S/N ratio spectra (Weiner et al. 2009; Rubin et al. 2010b). The pioneering study of Weiner et al. (2009) concluded that blueshifted Mg II absorption was ubiquitous in spectra of star-forming galaxies at $z \sim 1.4$ and demonstrated that the Doppler shift and absorption equivalent width of this absorption increase (rather slowly) with both stellar mass and SFR. At lower redshift, however, Rubin et al. (2010) did not find blueshifted Mg II absorption in a composite spectrum of galaxies with stellar masses similar to the Weiner et al. (2009) sample and speculated that the higher specific SFRs (i.e., SFR per unit stellar mass) characterizing $z \approx 1.4$ galaxies might be required to host such outflows. These two studies have demonstrated the existence of outflows and their possible evolution over a key period in the assembly of galaxies but are limited by their reliance on the *mean* spectrum of a population. Averaging many spectra together in a composite hides less common features like gas inflows (Sato et al. 2009; Rubin et al. 2012) and does not allow de-projection of the line-of-sight Doppler shift into an outflow velocity.

Here, we present the results of a survey of near-ultraviolet spectral features in 208 galaxies with redshifts between $0.4 < z < 1.4$ to provide an empirical measurement of how outflow and inflow properties change with cosmic time and galaxy properties. The galaxies were selected from the DEEP2 (Deep Extragalactic Evolutionary Probe 2) survey (Davis et al. 2003; Newman et al. 2012). This redshift survey provides a relatively unbiased sample for investigating the demographics of outflows and inflows in galaxies brighter than $R_{AB} = 24.1$ in four fields. More importantly though, selecting from the DEEP2 survey ensures that fundamental galaxy parameters – such as stellar mass, *B*-band luminosity, and *U* – *B* color – have been measured for the sample in a systematic manner (Bundy et al. 2006; Willmer et al. 2006). The additional photometry obtained for the AEGIS (All-Wavelength Extended Groth Strip International Survey) field allows us to measure SFRs for 51 of these galaxies; and these SFRs provide important information about the energy and momentum produced by supernovae, stellar winds, and radiation from massive stars and therefore available to drive outflows (Chevalier & Clegg 1985; Murray et al. 2005).

In this paper, we focus on the diagnostics provided by low-ionization, resonance-absorption lines, reserving the presentation of high-ionization interstellar absorption and stellar features, resonance emission, and fluorescent emission for future papers. Low-ionization, resonance lines in near-ultraviolet (rest-frame) spectra provide an empirical bridge between the optical transitions typically observed for low-redshift galaxies and the far-UV transitions studied extensively in spectra of high-redshift

galaxies (Steidel et al. 2010) because the Mg II $\lambda\lambda 2796, 2803$ doublet is accessible from the ground over the broad redshift range from roughly $0.25 < z < 2.5$ (Martin & Bouché 2009; Tremonti et al. 2007; Weiner et al. 2009; Rubin et al. 2010; Coil et al. 2011). At the lower end of this redshift range, Mg II absorption properties can be cross calibrated with rest-frame optical lines such as Na I 5890,96 and Ca II. At $z \gtrsim 1.19$, the Mg II absorption properties can be directly compared to far-UV transitions such as Si II, Al II, C II, and C IV commonly employed to study outflows in much higher redshift galaxies (Shapley et al. 2003; Steidel et al. 2010; Jones et al. 2012). The Mg II doublet provides a very sensitive probe of outflows for several reasons: singly-ionized magnesium is a dominant ionization state over a broad range of conditions, both lines have large oscillator strength, and the cosmic abundance of Mg is fairly high. Scattered Mg II emission, however, partially fills in the intrinsic absorption troughs in galaxy spectra and complicates the interpretation of the Doppler shift of the absorption trough. Spectral coverage blueward of the Mg II $\lambda\lambda 2796, 2803$ doublet provides access to a series of strong Fe II resonance lines which alleviate the concern about emission filling. The Fe II absorption troughs provide a cleaner view of the intrinsic absorption profile because fluorescence (rather than resonance emission) often follows absorption in several of these Fe II transitions (Prochaska et al. 2011; Erb et al. 2012). Another advantage of Fe II lines over the Mg II doublet arises from the large number of Fe II transitions in the NUV. The oscillator strengths of the NUV Fe II transitions span a substantial range and therefore make it possible to place useful bounds on the column density of singly-ionized iron, thereby constraining the total gas columns for an assumed (i.e., model dependent) metallicity and ionization fraction.

The paper is organized as follows. Section 2 introduces the sample and describes our new Keck observations, including a discussion of the systemic velocity determination and absorption-line sensitivity. After providing a broad overview of the near-UV spectral features, Section 3 explains the complications caused by emission filling and how we identify and measure galactic gas flows. We then compare the line profiles of the Mg II and Fe II absorption troughs in Section 4. In Section 5, we calculate the fraction of galaxies with a Doppler shift of low-ionization absorption relative to the systemic velocity and use previously measured galaxy properties to illustrate the demographics of the galaxies showing blueshifts. We then discuss the physical properties of the outflows and show how the outflow properties scale with galaxy properties. In Section 6, we expound on our discovery of net inflows of enriched gas. Section 7 summarizes our conclusions.

Throughout this paper we assume a cosmological model with $\Omega_m = 0.3$, $\Omega_\Lambda = 0.7$, and $H_0 = 70 \text{ km s}^{-1} \text{ Mpc}^{-1}$. We adopt the atomic oscillator strengths and cosmic abundance ratios given by Morton (2003) as well as the associated vacuum wavelengths for transitions shortward of 3200\AA . We refer to optical transitions by their wavelengths in air (for ease of comparison to previously published work), but we work with their vacuum wavelengths.

2. DATA

We present rest-frame, ultraviolet spectroscopy of $z \sim 1$ galaxies drawn from the Deep Extragalactic Evolutionary Probe 2 survey (Davis et al. 2003; Newman et al. 2012) using the Low Resolution Imager and Spectrometer (LRIS) on the Keck I telescope (Oke et al. 1995). Building a sample of 208 spectra required a significant observational campaign, custom-designed masks for the focal plane, and the remarkable blue sensitivity of Keck/LRIS-B (Steidel et al. 2004). We describe the sample selection in Section 2.1 and the new observations in Section 2.

2.1. Sample

The DEEP2 survey obtained redshifts for approximately 38,000 galaxies (Newman et al. 2012). The targets are spread over four fields widely separated in right ascension. In three of the four fields, the galaxies were color-selected to have redshifts $z > 0.7$. The fourth field, without color selection, is also the target of a deep imaging effort from the X-ray through the radio known as the All-Wavelength Extended Groth Strip International Survey, AEGIS (Davis et al. 2007). The panchromatic data in AEGIS provide more accurate estimates of galactic SFRs than are currently available for the other three fields (e.g., Noeske et al. 2007). Figure 1 summarizes the properties of the galaxies observed with LRIS.

Our primary sample of galaxies was chosen for spectroscopic follow-up based on redshift, $1.19 \leq z \leq 1.35$, and apparent magnitude $B < 24.0$. The magnitude cut ensures adequate continuum S/N ratio for absorption-line spectroscopy. This lower bound on the redshift guarantees that the C IV $\lambda\lambda 1548, 1550$ doublet lands longward of the atmospheric cut-off in the blue; and requiring $z < 1.35$ ensures that the Mg I 2853 transition is covered by the blue spectrum. The simultaneous coverage of far-ultraviolet (FUV) and near-ultraviolet (NUV) resonance lines allows a direct comparison of the transitions used to measure outflow velocities in $z \geq 2$ galaxies (Steidel et al. 2010) and $z \sim 1$ galaxies (Weiner et al. 2009; Rubin et al. 2010). In total, 68 galaxies meeting these criteria were observed on 6 masks. Each mask subtends a 5.5×5.5 field of view (Steidel et al. 2004). With an average of 11 primary targets per mask, we filled the masks with the following types of galaxies: (1) lower redshift ($z < 1.19$) galaxies with $EW([O II]) > 10 \text{ \AA}$ and $B < 24.5$ magnitudes, green valley galaxies, and K+A galaxy candidates (Yan et al. 2009). In total, 145 galaxy spectra were obtained through these masks with the 400 l mm^{-1} configuration of LRIS described below.

To utilize less than optimal observing conditions, a second set of masks were designed to obtain NUV spectroscopy of brighter galaxies. Spectra were obtained through 3 masks with galaxies prioritized as follows: (1) $B \leq 23.6$, $z \geq 0.7$, and $EW([O II]) > 20 \text{ \AA}$ (41 objects); (2) $B \leq 23.6$, $z \geq 0.7$, and $EW([O II]) < 20 \text{ \AA}$ (12 objects); (3) $B = 23.6 - 24.0$ and $z > 0.7$ (7 objects), $B \leq 23.6$ and $z < 0.7$ (1 object), and 6 foreground galaxies that lie at small angular separation from another target. Among these 67 galaxies, the spectra of four foreground objects with $z < 0.4$ are not discussed further in this paper due to their much lower redshifts. Hence, the second sample includes 63 galaxies observed with the 600 l mm^{-1} configuration of LRIS described below.

The primary sample ($z > 1.19$) includes three galaxies with colors that place them between the red sequence and blue cloud, a region of the color-magnitude diagram known as the green valley (Bell et al. 2003; Mendez et al. 2011). A total of 21 green valley galaxies were included on the 600 l mm^{-1} and 400 l mm^{-1} masks including the filler objects; most have $EW([O II]) < 10 \text{ \AA}$. The sample includes just two K+A (post-starburst) galaxies identified by Yan et al. (2009). One of these is a green valley galaxy and the other is a K+A galaxy with colors just redward of the green valley in the color - magnitude diagram.

As illustrated in Figure 1, these targets span the redshift range from 0.4 to 1.4, have luminosities between $-17 > M_B > -22$, and sample the stellar mass function between $8.9 < \log(M/M_\odot) < 11.6$. With a few exceptions noted above, the galaxies have blue $U - B$ colors. These spectra therefore probe the properties of low-ionization gas in and around typical star-forming galaxies 4.3 to 9.0 Gyr ago. The broad range in stellar mass makes this an appropriate sample to compare gas outflows and inflows over about 3 dex in dark-matter halo mass. The clustering of the population studied suggests that the most massive tertile of our sample resides in halos with $\log(M_h/M_\odot) > 12$ and that some of the galaxies in the lowest mass tertile populate halos with $\log(M_h/M_\odot) < 11$. In the stellar mass range $\log(M_*/M_\odot) = 9.0 - 11.5$, abundance matching suggests $\log(M_h/M_\odot) = 11.25 - 14.24$ at $z = 1.0$ and $\log(M_h/M_\odot) = 11.2 - 14.7$ at $z = 0.5$ (Behroozi, Conroy, and Wechsler 2010), consistent with the halo masses measured from galaxy clustering.

2.2. LRIS Observations

Multislit spectroscopy of the fields listed in Table 1 was obtained with LRIS on the Keck I telescope between 2007 October and 2009 June. Our primary instrumental configuration used the D680 dichroic, the LRISb 400 mm^{-1} grism blazed at $\lambda 3400 \text{ \AA}$, and the 831 mm^{-1} grating blazed at 8200 \AA on the red side. For the backup program, we configured LRIS with the D560 dichroic, 600 mm^{-1} grism blazed at 4000 \AA , and the 600 mm^{-1} red grating blazed at 7500 \AA ; this setup generally provided continuous spectral coverage between the red and blue spectra. In both configurations, the red-channel wavelength coverage usually included rest-frame-optical emission lines, most commonly $[O II] \lambda\lambda 3726, 29$. For all observations, the Cassegrain Atmospheric Dispersion Corrector (ADC) (Phillips et al. 2006) was enabled; and the width of the slitlets subtended $1''.2$ on the sky. We observed a total of 9 slitmasks, 6 in our primary configuration, and 3 in our back-up configuration, as described below. Conditions during the observing runs ranged from excellent (clear with $0''.6$ seeing) to variable (intermittent clouds with variable seeing up to $2''.0$). Details of these observations are presented in Table 1.

The data were primarily reduced using IRAF tasks, with scripts designed for cutting up the multi-object slit mask images into individual slitlets, flat-fielding using spectra of the twilight sky for the blue side and dome flats for the red side, rejecting cosmic rays, subtracting the sky background, averaging individual exposures into final stacked two-dimensional spectra, extracting to one dimension, wavelength and flux calibrating, and shifting

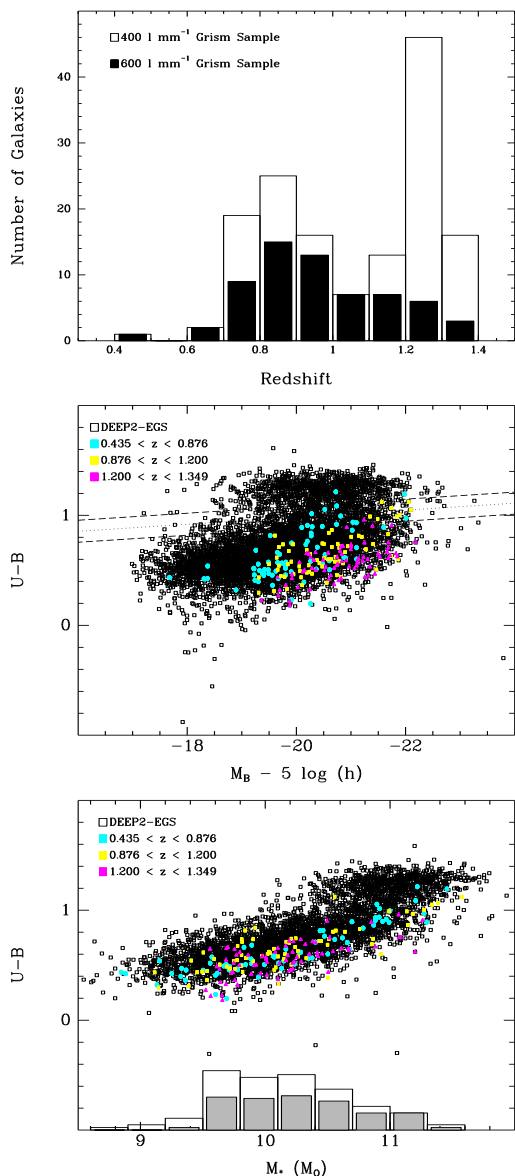


FIG. 1.— Properties of the galaxies observed with LRIS. (*Top*.) Redshift histogram. Higher redshift galaxies were specifically targeted for the lower resolution observations in order to obtain spectral coverage of resonance lines in the far-UV spectrum. The median redshifts of the galaxies observed with the 600 l mm^{-1} (282 km s^{-1} FWHM) and 400 l mm^{-1} (435 km s^{-1} FWHM) configurations are 0.94 and 1.12, respectively. (*Middle*.) Color – magnitude diagram (Willmer et al. 2006). The diagonal, dashed line marks the division between the red sequence and the blue cloud at $z \sim 1$. For the LRIS sample, galaxy color is anti-correlated with absolute magnitude ($r_S = -0.54$ at 7.8σ significance). The rest-frame optical colors of the galaxies (Willmer et al. 2006) become slightly bluer with increasing redshift due to the R -band selection of DEEP2 galaxies, and the lowest redshift tertile includes lower luminosity galaxies that would not pass our apparent magnitude cut at higher redshift. (*Bottom*.) Color vs. stellar mass and histogram of stellar mass (Bundy et al. 2006). Stellar mass was derived from SED fitting using a Chabrier stellar initial mass function (IMF; Chabrier 2003). The stellar masses would be 0.25 dex larger for a Salpeter IMF. The histogram distinguishes the most secure stellar masses (solid bars), obtained for 127 galaxies detected in the K-band, from the full sample of 208 galaxies with LRIS spectroscopy. The median stellar mass of the K-band-detected galaxies in our sample is $1.60 \times 10^{10} M_\odot$, and the galaxies not detected in the K-band have a median mass of $7.23 \times 10^9 M_\odot$ as estimated from optical photometry. Color and stellar mass are strongly correlated ($r_S = 0.77$ at 11σ significance).

into the vacuum frame. These procedures are described in detail in Steidel et al. (2003). We also followed the procedures outlined in Shapley et al. (2006) for background subtraction of deep mask spectra. Accordingly, to avoid potential oversubtraction of the background, the object continuum location was excluded from the estimate of the background fit at each dispersion point. Along with each target science spectrum, we extracted an error spectrum from the standard deviation of the mean of the individual exposures. We paid particularly close attention to deriving accurate wavelength solutions, adjusting an initial wavelength calibration derived from arc lamp exposures such that sky lines in our spectra appeared at the correct wavelengths. Finally, spectra were flux calibrated using observations of spectrophotometric standards throughout the run. To calibrate the entire observed wavelength range, spectra of these stars were obtained through slits at multiple positions in the focal plane because the standard longslit spectral coverage is too blue relative to that of the multislit coverage.

The spectral resolution realized differed between the two configurations. In the primary configuration (400 l mm^{-1} grism), the atmospheric seeing rather than the slit width determined the spectral resolution because the angular sizes of the galaxies (measured along the spatial direction of the slit) were slightly smaller than the slit. Scaling the width of arc lamp lines by this ratio, the average effective resolution was 435 km s^{-1} FWHM (full width at half maximum intensity) in the grism spectra and 150 km s^{-1} in the grating spectra. In the 600 l mm^{-1} configuration (used to observe lower redshift galaxies in non-optimal conditions), the galaxies typically filled the $1''.2$ aperture; and the slit width set the spectral resolution. We measured line widths of 282 km s^{-1} FWHM in the blue spectra and 220 km s^{-1} FWHM in the red spectra.

2.2.1. Determination of the Systemic Velocity

Identifying net outflows or inflows requires accurate *relative redshifts* between the galaxy and the low-ionization gas. We derive the galaxy redshifts directly from the LRIS spectra whenever possible. The ADC used for the LRIS observations compensates for atmospheric differential refraction and eliminates systematic errors caused by the aperture subtending different regions of a spatially-resolved galaxy at widely separated wavelengths. In most of our spectra, line emission in the [O II] doublet drives the determination of the galaxy redshift. Since dense, photoionized gas near star-forming regions produce this emission, we expect these redshifts to accurately describe the *systemic velocity*.

We derived LRIS redshifts for 167 galaxies using only the spectrum redward of the strong NUV Mg II and Mg I transitions ($\lambda_r > 3000 \text{ \AA}$). The most prominent spectral feature is usually the [O II] $\lambda\lambda 3726, 29$ doublet. However, strong [O III] $\lambda\lambda 4959, 5007$ and Balmer emission lines appear in spectra of the lower redshift galaxies; and Balmer absorption and the 4000 \AA break are prominent in some spectra. Although we have attempted to avoid strong resonance lines that are blends of photospheric and interstellar lines, interstellar Ca II $\lambda 3933, 69$ absorption could lower some of the LRIS redshifts relative to the purely stellar/nebular redshift in a few spectra. To esti-

mate a redshift, each spectrum was cross-correlated with 3 templates - an emission line galaxy, a quiescent galaxy, and a K+A galaxy - using the DEEP2 IDL pipeline; the best fit to a linear combination of these 3 templates was adopted as the LRIS redshift. In the absence of systematic errors introduced by line blending or slit placement, the error in the systemic velocity is the statistical error defined by the accuracy of centroiding an emission line, $\delta(v) \approx 19 \text{ km s}^{-1} (\sigma/190 \text{ km s}^{-1}) (S/N/10)^{-1}$, where $\sigma = FWHM/2.35$ is the spectral resolution.

For the other 41 galaxies with no LRIS coverage of [O II], we adopted the DEEP2 redshift and estimated the typical error in the systemic velocity from the redshift differences measured among the 167 galaxies. A positive redshift difference, $z_{DEEP2} - z_{LRIS} > 0$, means that adopting the DEEP2 redshift increases the inferred outflow speed (makes it more negative) by an amount $\Delta v_{sys} = c(z_{DEEP2} - z_{LRIS})/(1 + z_{LRIS})$. The mean offset computed from 167 spectra is $\Delta v_{sys} = -14 \pm 3 \text{ km s}^{-1}$, quite small compared to typical outflow/inflow speeds. The standard deviation of 41 km s^{-1} indicates the size of the systematic error in the redshift estimate. For a spatially-resolved source, uncertainties of this magnitude can result from an offset between the slit center and the brightest line emission; and although we use the same galaxy coordinates as the DEEP2 survey, the position angle of the slitlets generally differ.

2.2.2. Sensitivity to Absorption Lines

Prior to making measurements, we deredshifted the spectra to the rest-frame. We fit a low-order spline to the continuum in each galaxy spectrum avoiding regions near spectral lines. We divided the spectra by the fitted continuum to produce normalized spectra.

The resulting sensitivity to absorption lines is described by the minimum detectable equivalent width. Our observing strategy was designed to reach a rest-frame equivalent width $W_r(2796) \simeq 1 \text{ \AA}$ because the distribution function of intervening absorbers presents a break here which may signal association with galaxy halos (Nestor et al. 2006). The weakest line that we detect depends on the continuum S/N ratio (per pixel) at the observed wavelength of the transition as well as the intrinsic width of the absorption trough. In the 2400-2500Å bandpass, the median S/N ratios of the 400 l mm^{-1} and 600 l mm^{-1} spectra are 6.5 and 5.5, respectively. For purposes of illustration, a typical equivalent width limit can be estimated assuming $S/N \sim 5$ and the FWHM of an unresolved line. In the near-UV Fe II series, absorption troughs with rest-frame equivalent widths stronger than

$$W_{3\sigma} = 0.92 \text{ \AA} (6.5/SNR)_{\lambda 2450} \quad (1)$$

in 400 l mm^{-1} spectra, or larger than

$$W_{3\sigma} = 0.65 \text{ \AA} (5.0/SNR)_{\lambda 2450} \quad (2)$$

in 600 l mm^{-1} spectra, are easily detected. Just blueward of the Mg II doublet, the median continuum S/N ratios of the 400 l mm^{-1} and 600 l mm^{-1} spectra are, respectively, 4.6 and 6.6. The typical rest-frame sensitivities of the 400 l mm^{-1} and 600 l mm^{-1} spectra are, respectively,

$$W_{3\sigma} = 2.02 \text{ \AA} (5.0/SNR)_{\lambda 2790} \quad (3)$$

and

$$W_{3\sigma} = 0.58 \text{ \AA} (5.0/SNR)_{\lambda 2790}. \quad (4)$$

Farther to the red near the Mg II doublet, the continuum S/N in a particular spectrum is usually a bit lower than it is near Fe II 2587, $\lambda 2600$ due to the blue blaze of both grisms, so some of the spectra do not quite reach the target sensitivity in Mg II. Spectra with S/N ratio adequate to detect equivalent widths of 1-2 Å in individual galaxies at $z \sim 1$ have never been previously presented however in such large numbers.

3. DIAGNOSTICS OF OUTFLOWS AND INFLOWS

In this paper, we explore the diagnostics in the near-UV absorption-line spectrum longward of 2000Å. The emission line spectra are discussed further in two companion papers (Kornei et al. 2012b; Martin et al. 2012b). We defer the discussion of the far-UV spectral features to a future paper.

3.1. Near-UV Spectral Features

In Figure 2, we show the spectral region around the following NUV resonance lines: Fe II $\lambda 2249.88, 2260.78, 2344.21, 2374.46, 2382.77, 2586.65$, and 2600.17 ; Mg II $\lambda \lambda 2796.35, 2803.53$; and Mg I $\lambda 2852.96$. The absence of strong absorption in some individual spectra will partially fill in the absorption troughs in the composite spectra. Inspection of the individual spectra, however, shows that other factors prevent the absorption troughs from appearing completely black. Foremost, instrumental resolution smooths the spectrum and explains why the absorption troughs are slightly deeper in the 600 l mm^{-1} composite than in the 400 l mm^{-1} composite. In addition, the absorbing gas likely only partially covers the continuum source allowing some continuum light to leak out and fill in the absorption troughs; this partial covering has been fitted as a function of velocity using higher resolution spectra of brighter galaxies (Martin & Bouché 2009). All three of these factors – partial covering, instrumental resolution, and averaging spectra – imply that saturated absorption troughs need not be black.

Nebular emission lines mark dense gas near star-forming regions excited by either photoionization or shocks. The LRIS red-side spectra typically show strong [O II] $\lambda \lambda 3726, 29$ emission and cover an increasing number of rest-frame optical lines with decreasing redshift. In the NUV composite spectra, the [O II] $\lambda \lambda 2470.97, 2471.09$ lines are detected and blended. We attribute the broader width of the strong emission feature at $\lambda 2326$ to a blend of various C II] transitions rather than the Fe II $\lambda 2328$ feature suggested previously by Rubin et al. (2010a).

Line blending complicates measurements of the absorption troughs. The individual transitions of the Mg II doublet blend together in the 600 l mm^{-1} composite in Figure 2. The Fe II $\lambda \lambda 2587, 2600$ doublet can blend with the Mn II $\lambda \lambda \lambda 2576.88, 2594.50$, and 2606.26 triplet, recognizable in the higher resolution composite in Figure 2. Strong C II] $\lambda 2326$ emission often blends with the blue wing of $\lambda 2344$. In some individual spectra, the Mn II or C II] contamination compromises measurements of the maximum blueshift of absorption in the Fe II $\lambda 2587$ and

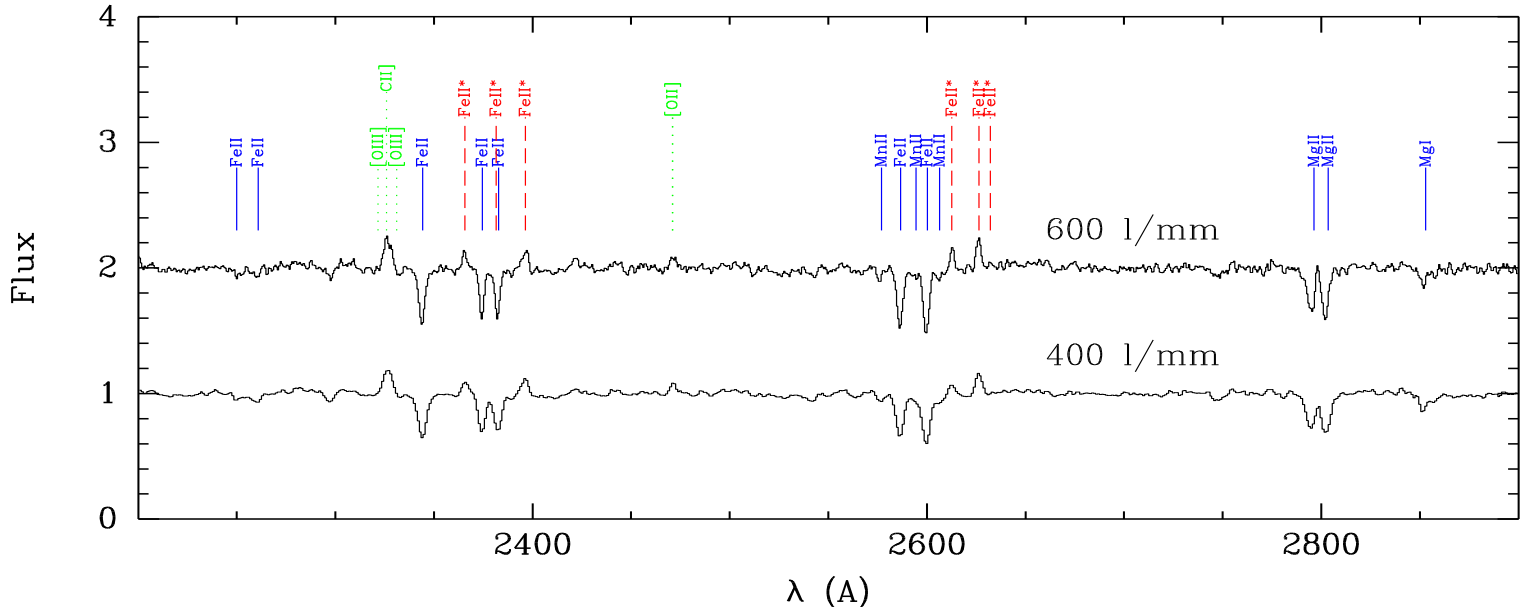


FIG. 2.— Composite, near-ultraviolet spectra of star-forming galaxies at $z \sim 1$. The continuum level has been normalized to unity. The lower spectrum in Figure 2 shows the addition of all 208 continuum normalized spectra after smoothing them to a common resolution of 435 km s^{-1} FWHM. The upper spectrum is the average 63 spectra observed at a resolution of 282 km s^{-1} FWHM. Resonance absorption lines, fluorescent emission lines, and nebular emission lines are labeled in blue, red, and green respectively; see Martin et al. (2012b) for a linelist.

Fe II $\lambda 2344$ line profiles, respectively. In contrast, the Fe II* $\lambda 2365$ emission blueward of Fe II $\lambda 2374$ is much weaker than the C II] $\lambda 2326$ emission, leaving $\lambda 2374$ as the preferred transition for looking for highly blueshifted Fe II absorption.

The Fe II $\lambda 2374$ transition has the lowest oscillator strength among the NUV Fe II transitions routinely detected in the individual spectra. The oscillator strength of Fe II $\lambda 2374$ is only a tenth that of the strongest transition, Fe II $\lambda 2383$. The oscillator strengths of Fe II $\lambda 2383$ and Mg II $\lambda 2803$, the weaker line in the Mg II doublet, are nearly equal. The shorter wavelength transition in the Mg II doublet has an oscillator strength twice that of the longer wavelength transition. The rough equality of the absorption equivalent widths in all these transitions in Figure 2 demonstrates the resonance absorption is typically optically thick. The weak Fe II $\lambda 2250$ and $\lambda 2261$ transitions, just barely detected in Figure 2, are optically thin and particularly useful for constraining the column density of single-ionized iron, $N(\text{Fe}^+)$.

In Figure 2, the longer wavelength, lower oscillator strength transition in the Mg II doublet has the larger equivalent width. Many of the individual spectra show prominent Mg II emission lines, and the unphysical absorption equivalent width ratio appears to arise from the troughs being partially filled in by resonance emission. A similar contradiction appears in the Fe II equivalent widths; the equivalent width of Fe II $\lambda 2383$ absorption is low relative to other Fe II transitions. This *emission filling* complicates direct measurement of the intrinsic absorption troughs, so a strategy for measuring the Doppler shift and equivalent width of the resonance absorption features requires careful development.

3.2. Emission Filling

In the normal situation for intervening absorption in quasar spectra, where the continuum source subtends a small angular size compared to the gas clouds, a negligible fraction of photons absorbed in the resonance transitions are re-emitted along our sightline. For extended sources like galaxies, however, the equivalent width of the emission can be comparable to the absorption equivalent width. Since emission may be detected from the entire galaxy but only gas on the near side of the galaxy contributes to the absorption trough, the emission and absorption lines do not normally cancel each other out completely (even in the absence of dust or non-spherical geometry). We will refer to resonance emission filling the intrinsic absorption trough as *emission filling*. In spectra of nearby galaxies, the near absence of emission filling in Na I $\lambda\lambda 5890, 96$ has long been attributed to the high gas densities (and therefore high dust content) in regions with a significant neutral sodium fraction (Heckman et al. 2000; Martin 2005, 2006; Chen et al.). At the same time, emission filling is quite often detected in Mg II (Weiner et al. 2009; Martin & Bouché 2009; Rubin et al. 2011a; Coil et al. 2011; Erb et al. 2012).

Absorption from the ground state necessarily leads to resonance emission when the ground state has a single level, such as in the cases of Na I, Mg II, and C IV ions, but can be followed by fluorescent emission when the ground state has fine structure, such as for the Fe⁺ and Si⁺ ions. In the composite spectra in Figure 2, we identify fluorescent Fe II* lines at $\lambda 2365.56$, 2396.26 , 2612.56 , and 2626.45 ; the Fe II* $\lambda 2632.10$ line may be marginally detected in a few individual spectra. Because these Fe II* emission lines all have upper levels that are populated by absorption from the ground state, we can attribute them to fluorescence. No absorption from excited levels in Fe II is detected consistent with densities well below the critical densities of the Fe II transitions.

We understand the reduction in Fe II $\lambda 2383$ equivalent width relative to Fe II $\lambda 2374$ in terms of emission filling. The spectroscopic selection rules for total angular momentum imply that the Fe II $\lambda 2383$ photons will scatter like the common transitions (such as Mg II $\lambda\lambda 2796, 2803$) with a singlet, ground state. Absorption of Fe II $\lambda 2374$ photons, however, can produce fluorescent Fe II* $\lambda 2396.26$ photons that do not fill in the resonance absorption trough. The relative radiative decay rates suggest that 88% of Fe II $\lambda 2374$ absorptions will decay as Fe II* $\lambda 2396.26$ photons.

Fluorescent emission following Fe II $\lambda 2344$ absorption in Fe II* $\lambda 2381.49$ will also contribute to filling in the Fe II $\lambda 2383$ absorption trough, but the resonance scattering of the latter will dominate the emission filling of the Fe II $\lambda 2383$ trough. An analogous situation arises in the longer wavelength Fe II multiplet shown in the middle panel of Figure 3, where absorption in the transition with the higher oscillator strength, Fe II $\lambda 2600$, usually results in emission of a photon at the same wavelength. In contrast, the excited level of the weaker transition Fe II $\lambda 2587$ typically decays via a longer wavelength, and therefore fluorescent, photon. Comparison of the Einstein A coefficients among all the transitions from the excited level indicates a decay via Fe II* $\lambda 2612.65$ 45% of the time, through Fe II* $\lambda 2632.10$ 23% of the time, and in the resonance transition $\lambda 2587$ the remaining 32% of the time. These fluorescent emission lines, and the Fe II* $\lambda 2626$ fluorescence that follows the absorption in the Fe II $\lambda 2600\text{\AA}$ resonance transition (13% of the time), are clearly detected in the spectra shown in Figures 2-5 and will be discussed further in a forthcoming paper (Kornei et al. 2012b; Martin et al. 2012b).

Photons absorbed in the Mg I $\lambda 2853$ transition will scatter (rather than fluorescence) because the ground state is again a singlet. Could emission filling also explain the decreasing equivalent width of Mg I $\lambda 2853$ in the spectra of lower mass galaxies seen in Figure 1. It would be premature to draw this conclusion from the equivalent widths of the Mg I $\lambda 2853$ feature alone; any of a number of factors – such as a decrease in the gas velocity dispersion, an increase in the Mg II ionization fraction, or a reduced covering fraction – would systematically decrease the equivalent width with decreasing stellar mass. Factors favoring this interpretation, however, include the resonance emission seen in other transitions and the observation (see the rightmost panel of Figure 3) that the emission is preferentially decreased near and redward of the systemic velocity.

The presence of Mg II emission in galaxy spectra (Martin & Bouché 2009; Weiner et al. 2009) can often be attributed to resonant scattering (Rubin et al. 2011; Coil et al. 2011; Erb et al. 2012). Emission that fills in part of the absorption trough greatly complicates the interpretation of the Doppler shift and equivalent width of Mg II absorption in galaxy spectra. Radiative transfer models, however, predict little emission at the highest outflow speeds (Prochaska et al. 2011). The maximum blueshift of the Mg II $\lambda 2796$ absorption is therefore the only property of the intrinsic absorption profile that we can routinely measure directly. The maximum blueshift of the absorbing gas has also been used previously to discuss whether outflowing gas is bound to the galaxy (e.g., Heckman et al. 2000; Martin 2005; Martin & Bouché;

Weiner et al. 2009; Coil et al. 2011; Heckman et al. 2011).

3.3. Fitting Fe II Absorption Troughs

Examination of our spectra showed that emission filling complicates the direct measurement of intrinsic absorption properties, especially in the Mg II $\lambda\lambda 2796, 2803$, Fe II $\lambda 2383$, and Fe II $\lambda 2600$ transitions. First, the equivalent widths measured for transitions from a single ion do not always follow the curve of growth (Spitzer 1978). In the Figure 2 spectra, the highest oscillator strength Fe II transition at $\lambda 2383$ has a lower equivalent width than other Fe II transitions. Secondly, a partially filled absorption trough has a centroid velocity that is bluer than the centroid of the intrinsic absorption profile because the resonance line emission is closer to the systemic velocity than is the absorption. This prevents robust measurement of the Doppler shift without detailed modeling (Prochaska et al. 2011). Figures 7 and 8 in the recent work of Erb et al. (2012) further illustrate these points quantitatively.

We circumvent these problems by adopting the centroid velocity of Fe II absorption rather than Mg II as our primary indicator of the net Doppler shift of the low-ionization gas. In our discussion of emission filling, we explained why we expect the Fe II $\lambda 2344, 2374$, and 2587 absorption troughs to reflect the outflow opacity more closely than does the Mg II profile. Absorption in these transitions usually leads to fluorescence (i.e., emission of a longer wavelength photon) rather than scattering, so the intrinsic shape of the absorption trough is much less affected by emission filling than the Mg II or Fe II $\lambda 2383$ lines. We therefore fit only those transitions that have a high probability of fluorescence, i.e., decaying via a longer wavelength photon rather than scattering and thereby filling in the absorption trough.

We detect resonance absorption lines at high significance in the individual LRIS spectra. Since the spectral resolution does not fully resolve the shapes of most absorption troughs, we can only robustly measure the Doppler shifts and equivalent widths of these absorption troughs in general. Centroid velocities have been widely used to describe galactic outflows in the past, but we caution the reader that interstellar absorption near the systemic velocity blends with the absorption profile from outflowing (inflowing) gas in a low resolution spectrum. In Section 3.3.2, we will examine how interstellar absorption at the systemic velocity biases the estimates of outflow properties.

3.3.1. Single-Component Fits Describing the Absorption Centroid Velocity

In Figure 5, we show examples of the Fe II absorption-line profiles from our LRIS data. The Doppler shift was jointly fit to five Fe II transitions: Fe II λ 2250, 2261, 2344, 2374, and 2587. The Fe II transitions at $\lambda 2383$ and $\lambda 2600\text{\AA}$ are excluded from the fit because they show the strongest emission filling. Even though they significantly constrain the column density, the weak Fe II 2250 and 2261 transitions provide little constraint on the Doppler shift. The fitted model simply describes the net Doppler shift of the intrinsic Fe II absorption.

The shapes of the absorption troughs are strongly influenced by the instrumental response and are therefore often well-described by a Gaussian line profile. We adopted

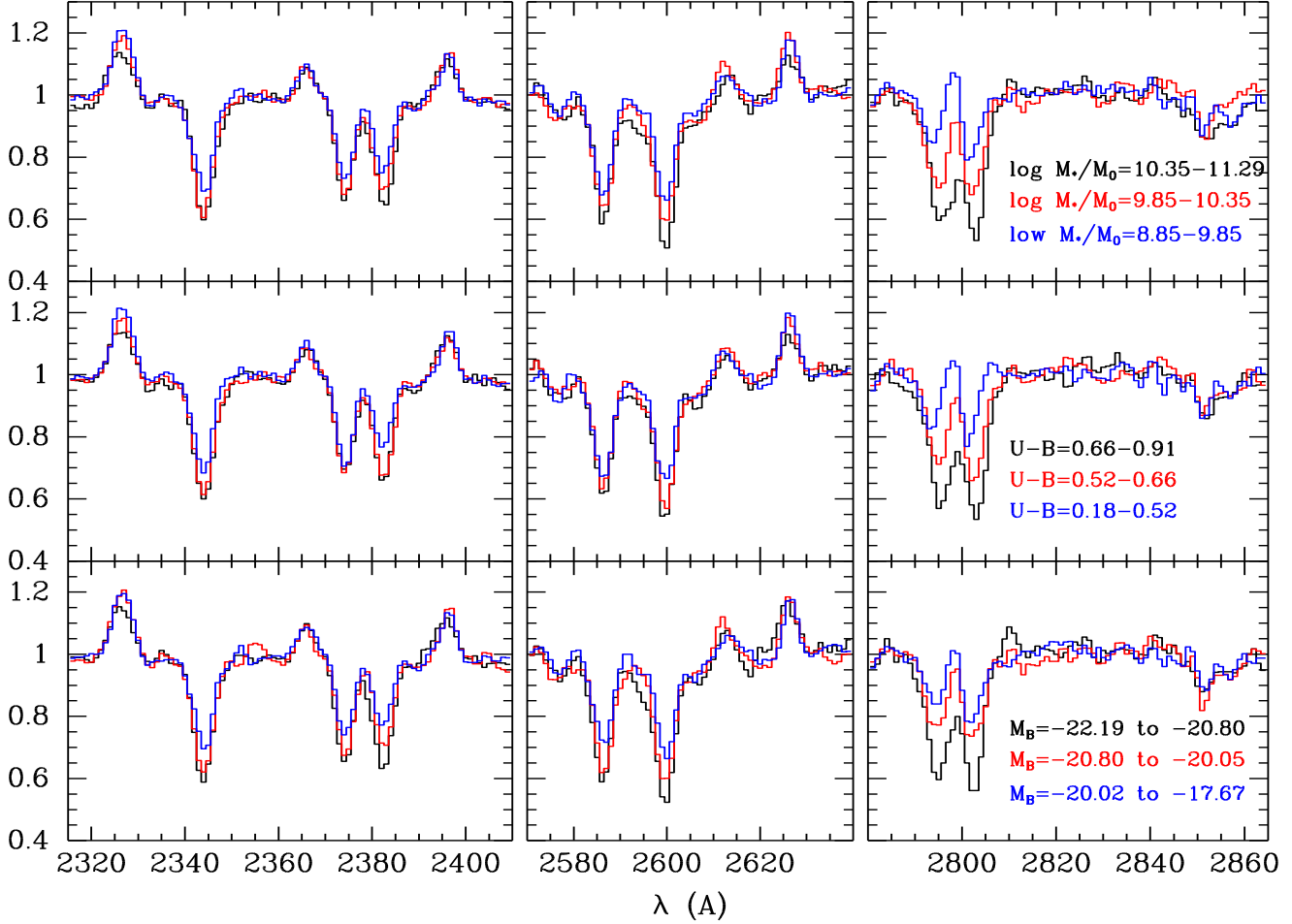


FIG. 3.— Comparison of the Fe II and Mg II line profiles in average spectra of galaxies with different properties. *Top:* Towards lower mass galaxies, the Mg II absorption troughs become shallower, the Mg II emission becomes stronger, and the Fe II* emission in $\lambda 2612, 2626$ increases. In the highest mass tertile, the Mg II doublet ratio is not inverted, and Fe II $\lambda 2383$ has a higher equivalent width than Fe II $\lambda 2374$, as it should in the absence of emission filling. *Middle:* We see similar trends with color because color is strongly correlated with stellar mass (redder galaxies are more massive on average). *Bottom:* The resonance absorption troughs become deeper in more luminous galaxies. See the text for a full explanation of why the stronger absorption in more luminous, redder, more massive galaxies is largely attributable to emission filling.

a more physical description of the line profile in order to properly model the relative line strengths in the Fe II series. For each transition, j , our fitting function takes the form

$$I_j(\lambda) = I_{c,j}(\lambda)e^{-\tau_j(\lambda)}. \quad (5)$$

The optical depth distribution,

$$\tau_j(\lambda) = \tau_{0,j}e^{-(\lambda-\lambda_{0,j})^2c^2/(b^2\lambda_{0,j}^2)}, \quad (6)$$

introduces the Doppler parameter b in order to describe the location of the absorbing clouds in velocity space relative to line center. The central wavelengths of the five Fe II transitions, $\lambda_{0,j}$, are tied together to define a single Doppler shift, V_1 . The optical depths of the different transitions are tied together by the ratio of their oscillator strengths (and the rest wavelengths of the transitions), so one parameter $\tau_0(\lambda 2344)$ is sufficient to define the absorption optical depth at line center for each transition. Equivalently, the column density $N(Fe^+)$ determines the optical depth in each transition. When line profiles from multiple transitions overlap at a given wavelength, e.g. redshifted Fe II $\lambda 2374$ and blueshifted Fe II

$\lambda 2383$, we add their respective contributions to the total optical depth, $\tau(\lambda)$, at that wavelength. Provided the form of the optical depth distribution is symmetric about the centroid of the line profile, λ_0 , the shape of this distribution does not affect the fitted central wavelength λ_0 , which defines the Doppler shift V_1 .¹⁰

The free parameters V_1 , b , and $\tau_0(\lambda 2344)$ were fitted

¹⁰ In our schematic picture, the angular extent of the stellar population producing the continuum emission is much larger than that of a gas cloud. This partial covering of the continuum source has often been described by a covering factor, C , which represents the fractional area of the continuum source covered by gas clouds. Since a fraction $(1-C)$ of the galaxy continuum is observed directly without any absorption, a widely used, alternative parameterization of the line profile is $I(\lambda)/I_c(\lambda) = 1 - C + Ce^{-\tau(\lambda)}$ (e.g., Rupke et al. 2005). This parameterization of the absorption trough, however, does not capture the strong velocity dependence of the covering factor found by Martin & Bouché (2009). For this reason, and because velocity-dependent covering factors (Arav et al. 2005) introduce structure in the line profile that cannot be observed at the resolution of our spectra, we simply fitted the 3-parameter model of Eqn. 5. For any symmetric $C(v)$ distribution, partial covering will clearly not impact the fitted Doppler shift. In our simple parameterization of the line profile, Eqn. 5 where $C \equiv 1$, the width of the absorption trough depends on both b and τ_0 . When we at-

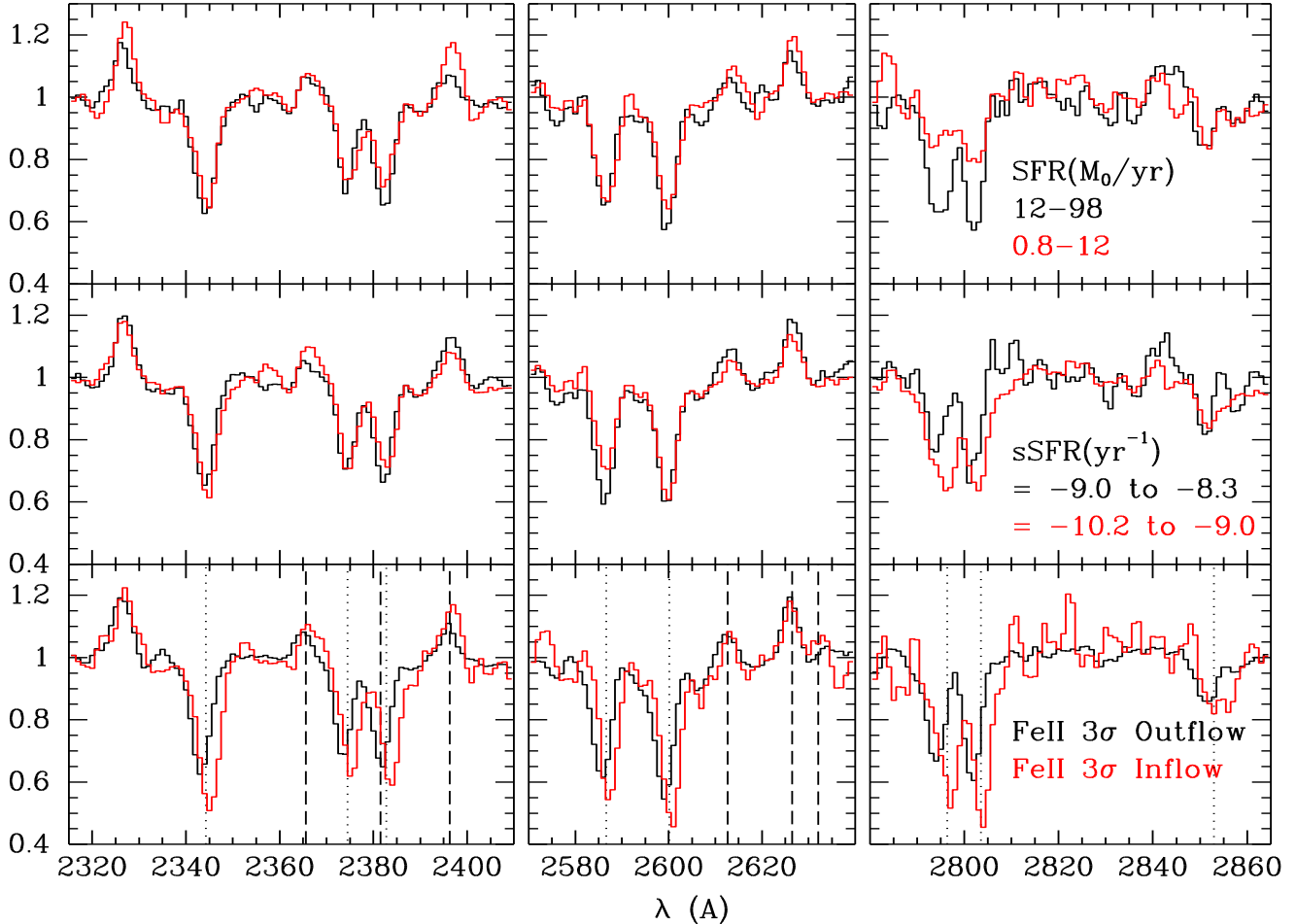


FIG. 4.— Composite spectra for subsets of galaxies with measured SFR or significant bulk flows. *Top*: The subset of galaxies in AEGIS with measured SFRs. The higher SFR galaxies have higher equivalent widths in Mg II, Fe II $\lambda 2600$, and Fe II $\lambda 2383$. *Middle*: These absorption equivalent widths have a weaker dependence on specific SFR. The Mg II equivalent width is slightly lower in the half of the sub-sample with the highest SFRs. The inverted equivalent width ratio in Mg II clearly indicates this is due to the emission filling. *Bottom*: The subset of galaxies with the most significant Fe II blueshifts is compared to the subset with significant Fe II redshifts. Unlike the other composite spectra shown here and in Figure 3, the continuum S/N ratio is lower in the “inflow” spectrum (10 galaxies) than the “outflow” spectrum (35 galaxies). The wavelengths of the resonance absorption lines are marked with dotted lines for reference; and the Fe II* transitions are marked with dashed lines.

as follows using custom software. Each galaxy spectrum was de-redshifted to the rest frame and normalized by the continuum. A model with line profiles centered at zero velocity was created assuming $b = 200 \text{ km s}^{-1}$ and $\tau_0 = 1$. The model was convolved with a Gaussian profile of width $\sigma = 120 \text{ (185) km s}^{-1}$, which describes the instrumental response for the 600 l mm^{-1} (400 l mm^{-1}) spectra. The residuals between the model and the data were minimized iteratively using the Levenberg-Marquardt algorithm (Press et al. 1992) to make successive parameter estimations. The resulting covariance matrix provides a good estimate of the uncertainty in a fitted parameter when the errors are normally distributed. We tested this assumption by bootstrap resampling typical spectra. The resulting distributions of Doppler shift measurements were found to be normally distributed, so we use the corresponding element of the covariance matrix to estimate the 68% confidence interval on V_1 ,

$\delta V_1 \equiv \sqrt{\sigma_{V_1, V_1}^2}$. The Doppler shifts from the joint fit, V_1 , were also found to be consistent with the average of the velocities measured in the individual fits to Fe II $\lambda 2344$, $\lambda 2374$, and $\lambda 2587$. The error distributions for τ_0 and b , in contrast, are often not normally distributed, so we do not use these fitted parameters in our analysis; we choose instead to discuss measurements of equivalent width and (in a later section) the bluest absorption velocity V_{max} .

These joint fits to five Fe II lines describe the Doppler shift of the entire absorption trough with one velocity, so we will refer to them as the *single-component* fits. They avoid transitions with strong emission filling and beat down statistical error by combining information from multiple transitions. Among 165 single-component fits, we find significant blueshifts, $V_1/\delta(V_1) \leq -3$, for 35 spectra and significant redshifts, $V_1/\delta(V_1) \geq 3$, for 11 spectra.¹¹ Within the LRIS sample of 208 spectra, 36

tempted to include a covering factor in the description of the line profile, we found b , C , and τ_0 were all strongly covariant due to the low resolution of our data.

¹¹ As discussed further in Section 6, two of the inflows are not significant due to systematic errors.

had no good Fe II lines to fit due sky line residuals (5 cases) or low equivalent widths (31 spectra). The fit failed to converge for an additional 7 spectra. Since the 43 spectra without a fit have low continuum S/N ratio, the absence of significant absorption does not provide much information; and we drop these from the analysis of V_1 Doppler shifts.

3.3.2. Two-Component Fits Illustrating ISM Absorption at the Systemic Velocity

Having identified bulk outflows and inflows with the single-component fitting, we next model the contribution of the interstellar medium (at the systemic velocity) to obtain an estimate of the velocity that characterizes the absorption equivalent width produced by the bulk flow. In spectra of nearby star-forming galaxies, interstellar gas is generally the primary source of absorption in resonance lines near the systemic velocity (Heckman et al. 2001; Martin 2005; Martin 2006; Rupke et al. 2005; Soto et al. 2009). Stronger interstellar absorption at the systemic velocity is observed towards low redshift galaxies with higher inclinations (Chen et al. 2010). In these resonance lines, the equivalent width of the interstellar absorption only becomes weaker than the stellar photospheric absorption in post-starburst galaxies, which can be recognized by the presence of absorption lines from excited states that are populated in photospheres but not in diffuse gas. For our purposes here, we will use the term *maximum interstellar component* in the broadest sense to represent all absorption at the systemic velocity, possibly including some contribution from stellar photospheres.

We modeled the Fe II series, again excluding the $\lambda 2383$ and $\lambda 2600$ lines due to emission filling, using two velocity components – a *systemic component* with no Doppler shift and a *Doppler component* with a fitted velocity, V_{Dop} . Since the absorption troughs are not well resolved, we found that five parameter fits allow many degenerate solutions. To produce meaningful Doppler velocities, we fixed the width of the systemic component. Because the systemic component represents interstellar gas, we set its Doppler parameter to be consistent with the measured velocity dispersion of nebular gas previously fitted to the [O II] doublet. These photoionized, emission regions are believed to reside in a gaseous disk; and their velocity dispersions have been directly measured from the [O II] $\lambda\lambda 3726, 29$ doublet. The doublet is resolved in the 831 mm^{-1} (red channel) spectra, and the fitted Gaussian σ has been corrected for instrumental broadening. We choose $b_{sys} = \sqrt{2}\sigma([OII])$. We then fitted the maximum interstellar absorption to the Fe II series by varying the optical depth at line center, obtaining the deepest absorption trough at $v = 0$ consistent with the data. With the interstellar component now fully specified, we next fitted the Doppler shift, Doppler parameter, and central optical depth of the Doppler component.

This two-component fitting approach has two critical advantages over simply reflecting the redshifted portion of the fitted absorption trough to create a model of the systemic absorption, as implemented for example by Weiner et al. (2009). First, it does not require fully resolved troughs because the model is convolved with the instrumental response. Second, it can be used to estimate the effect of the interstellar medium (ISM) on the inferred velocity of redshifted absorption (gas inflows) as

well as blueshifted absorption (gas outflows). We only fit two components when the single-component fit indicated a significant outflow or inflow. The low resolution of our spectra does not constrain the two-component fits well enough to use them to determine whether the spectrum shows a net flow in the first place.

Figure 5 shows examples of the two-component fits relative to the single-component fits. The V_{Dop} velocity from the two-component fit is bluer than the single-component Doppler shift V_1 , but the difference is typically less than the error bar δV_1 . The maximum single-component blueshift is -330 km s^{-1} ; but the blueshift of the Doppler component reaches -550 km s^{-1} in the two-component fits. This trend is consistent with that shown in Coil et al. (2011), where the impact of the systemic component on the outflow velocity is quantified. While the one- and two-component fits yield consistent outflow velocities for many spectra, there is a subset for which accounting for a symmetric absorption component at the systemic velocity significantly increases the estimated outflow velocity. It is therefore of interest to understand which galaxies have this stronger interstellar absorption component.

The equivalent width of the systemic component rises strongly with increasing stellar mass. Hence modeling the systemic component results in fitted outflow velocities about 200 to 300 km s^{-1} bluer regardless of whether the systemic absorption is strong or weak. Only the most massive galaxies in our sample, however, exhibit exceptionally strong interstellar absorption with $W_{sys} \gtrsim 2.3 \text{ \AA}$. In this paper, we use the V_1 values to determine whether a net flow is present; and, when it is, we use the values of V_{Dop} and W_{sys} to illustrate how the interstellar absorption at the systemic velocity may influence the conclusions drawn from the single-component fits.

3.3.3. Equivalent Widths and Ionic Column Density

In general, the *intrinsic* equivalent width of each Fe II line in a spectrum is determined by a combination of the ionic column density, $N(\text{Fe}^+)$, and the Doppler parameter, b , called the curve of growth (Spitzer 1978). The equivalent width of optically-thin transitions is sensitive to Fe II column density, but the equivalent width of optically-thick transitions depends primarily on the velocity spread of the absorbing gas. The measured equivalent widths do not necessarily follow this theoretical curve of growth, however, because emission filling reduces the intrinsic area of each absorption trough in a given spectrum by a different amount. Here we discuss the measured equivalent widths of a line not affected much by emission filling, Fe II $\lambda 2374$, and the upper limit on the equivalent width of a weak line, Fe II $\lambda 2261$, detected in composite spectra. Since the Fe II 2261 transition has an oscillator strength 12.8 times lower than that of Fe II 2374, the equivalent width measurement and upper limit together constrain the ionic column density to order-of-magnitude accuracy.

How accurately the ionic column density can be estimated from a single line depends on the optical depth of the transition. The column density at which the absorbing gas becomes optically thick, i.e., $\tau(\lambda) \equiv 1$, depends on the absorption cross section. At line center, the optical depth can be expressed as

$$\tau_0 = 1.498 \times 10^{-15} \lambda_0 f N b^{-1}, \quad (7)$$

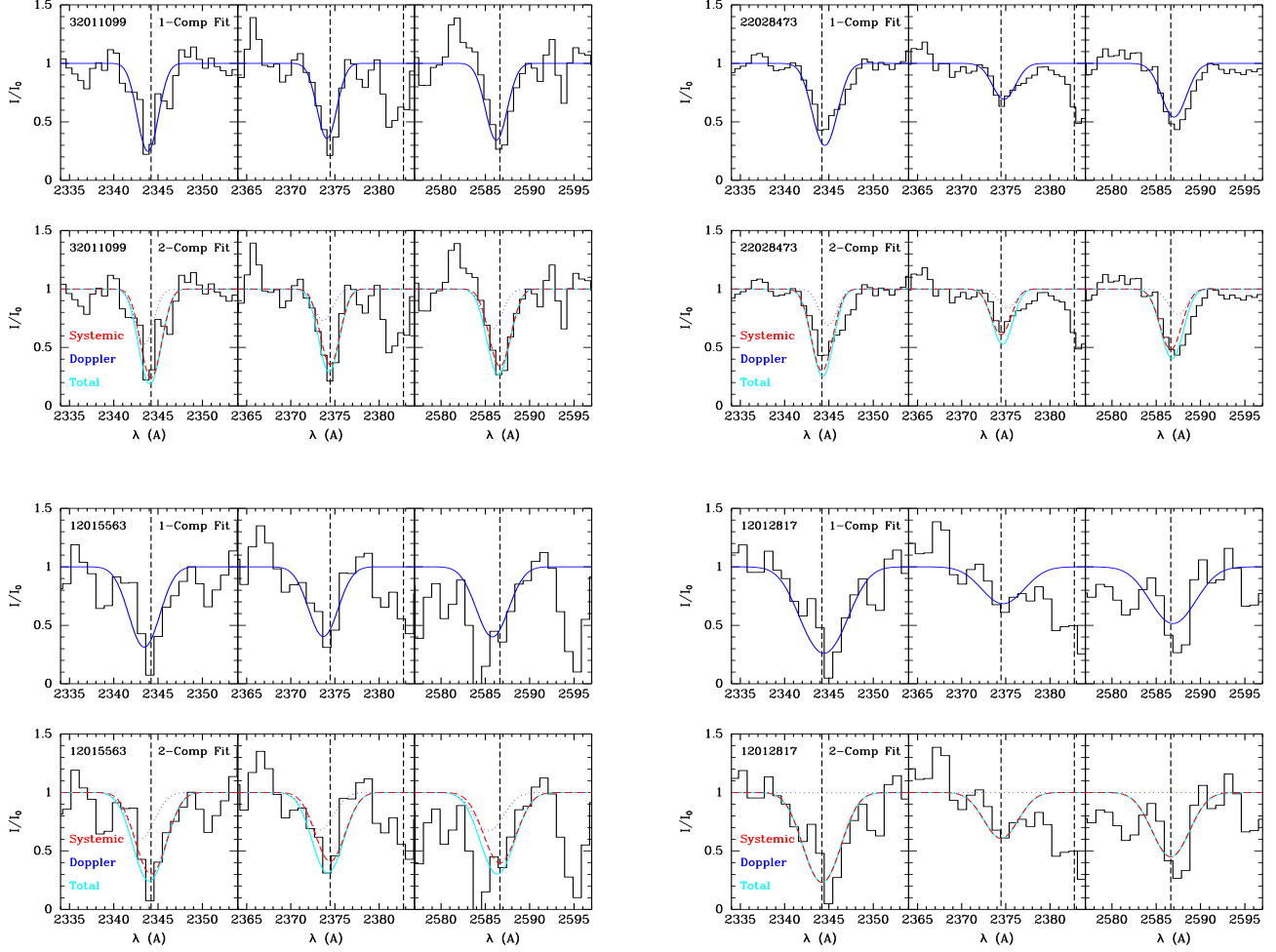


FIG. 5.— Four comparisons of single-component (top panels) and two-component (bottom panels) fits to the Fe II series. The two component fits increase the estimated velocity of the flow, relative to the single component fit. *Top Left Panels:* The single-component fit to the 600 l mm⁻¹ spectrum of 32011099 yields an outflow velocity of -46 ± 14 km s⁻¹. In a two-component fit, a systemic component at zero velocity describes much of the total absorption equivalent width; but the fit also requires a blueshifted Doppler component ($V_{Dop} = -101 \pm 25$ km s⁻¹, $W_{Dop} = 1.16\text{\AA}$) to model the net blueshift of the absorption trough. *Top Right Panels:* The single-component fit to the 600 l mm⁻¹ spectrum of 22028473 yields an inflow velocity of 42 ± 10 km s⁻¹. In a two-component fit, a systemic component at zero velocity describes much of the total absorption equivalent width; but the fit also requires a redshifted Doppler component ($V_{Dop} = 133 \pm 47$ km s⁻¹ for the inflow and $W_{Dop} = 0.46\text{\AA}$) to model the net redshift of the absorption trough. *Bottom Left Panels:* The single-component fit to the 400 l mm⁻¹ spectrum of 12015563 yields an outflow velocity of -98 ± 42 km s⁻¹. In a two-component fit, a systemic component at zero velocity describes much of the total absorption equivalent width; but the fit also requires a blueshifted Doppler component ($V_{Dop} = -154 \pm 84$ km s⁻¹, $W_{Dop} = 1.55\text{\AA}$) to model the net blueshift of the absorption trough. *Bottom Right Panels:* The single-component fit to the 400 l mm⁻¹ spectrum of 12012817 yields an inflow velocity of 29 ± 44 km s⁻¹. In a two-component fit, a systemic component at zero velocity describes much of the total absorption equivalent width.

where f denotes the oscillator strength of the transition, the wavelength of the transition is in \AA , the column density has units of cm^{-2} , and the Doppler parameter is in km s^{-1} .

The rough equality of the equivalent widths of Fe II $\lambda 2344$, $\lambda 2374$, and $\lambda 2587$ in many of the LRIS spectra indicates these transitions are typically optically thick. The intrinsic equivalent widths of these transitions therefore provide lower bounds on the ionic column density. Our measurement of the equivalent width for the transition with the lowest oscillator strength, Fe II $\lambda 2374$, yields the best lower limit on $N(\text{Fe}^+)$. In this optically-thin limit, the linear relationship between equivalent width and ionic column yields a lower limit

$$N(\text{Fe}^+) \geq 6.30 \times 10^{14} \text{ cm}^{-2} W_{2374}(\text{\AA}). \quad (8)$$

The Fe II $\lambda 2261$ absorption trough is generally much

weaker than the Fe II $\lambda 2374$ line, so we can be certain that the Fe II $\lambda 2261$ transition falls on the linear part of the curve-of-growth. In individual spectra, we measure an upper limit on the equivalent width of Fe II $\lambda 2261$. We place an upper bound on the ionic column density,

$$N(\text{Fe}^+) \leq 9.06 \times 10^{15} \text{ cm}^{-2} [3\sigma(W_{2261})], \quad (9)$$

where the 3σ upper limit on the equivalent width has units of \AA .

3.4. Highest Velocity Mg II Absorption

Resonance emission is not expected to fill in the high velocity wings of the the intrinsic Mg II absorption profile (e.g., Figure 5 of Prochaska et al. 2011). If the gas column is low at high velocities we expect to detect Mg II absorption even though the Fe II absorption is too weak

to detect for several reasons. First, consider equal column densities of Fe^+ and Mg^+ . In the optically thin limit, the Fe II $\lambda 2374$ equivalent width would be a factor of 20 lower than the intrinsic Mg II $\lambda 2796$ equivalent width. Next, this equivalent width ratio could be higher because the cosmic abundance ratio of Mg to Fe is a factor of 1.2, and Fe is more depleted onto grains than is Mg (Savage & Sembach 1996). Finally, since the first and second ionization potentials of iron are similar to those of magnesium, we might expect Fe II and Mg II ions to be present in the same phase of the wind.¹² The column density ratios calculated from grids of photoionization models show, however, that the relative fraction of Fe and Mg in the singly-ionized state is sensitive to the ionization parameter. Over the range of likely ionization parameters near galaxies, the Fe II column density can be similar to or significantly less than the Mg II column density (Churchill et al. 2003). Hence, the relative optical depths in Fe II $\lambda 2383$ and Mg II $\lambda 2803$ can be similar, but the Mg II optical depth can easily be much larger for a range of physical reasons.

3.4.1. Measurement Technique

The LRIS spectra of 186 of the 208 galaxies cover the Mg II doublet. In 13 spectra, no significant absorption trough was detected at a rest wavelength of 2796 Å. In an additional 44 spectra, the absorption spikes were more narrow than a resolution element, $FWHM = 435(282) \text{ km s}^{-1}$ for 400 l mm^{-1} (600 l mm^{-1}) respectively. Some galaxies among these 57 galaxies are characterized by strong Mg II emission that fills the absorption trough. Among the most prominent Fe II outflows, i.e., the 35 with 3σ outflows, 33 spectra provide Mg II coverage. We measured the properties of the Mg II absorption for composite spectra and 104 individual spectra excluding spectra that had weak $\lambda 2796$ absorption or sky-subtraction artifacts near the doublet.

Some of the individual spectra show a Mg II profile with a blue wing. To characterize the minimum (maximum) velocity of the Mg II absorption, we measure the velocity, V_{max} , blueward (or redward) of the systemic velocity at which the spectral intensity is consistent with the continuum level (at the 1σ level); specifically, we define $I(\lambda_{vmax}) = 1 - \delta I(\lambda_{vmax})$, where $\delta I(\lambda)$ is the error spectrum. To measure V_{max} , we added a Gaussian random deviate to the original value of the intensity (with standard deviation matched to the error spectrum at each wavelength), remeasured the maximum velocity of the absorption trough in this modified spectrum, and calculated the average V_{max} and standard deviation after 1000 iterations. The statistical error was taken to be the standard deviation or half a pixel width, whichever was larger.

Clearly, this definition is only meaningful when the blue wing of the line profile is well resolved. Furthermore, comparisons of V_{max} must be made at similar spectral S/N ratio. The Mg II $\lambda 2796$ absorption trough provides our most sensitive measurement of V_{max} and is not blended with another transition. When the Fe II lines have a significant redshift, i.e., the 9 inflow galax-

ies discussed in Section 6, we measure the the maximum (inflow) velocity from the red wing of Mg II 2803; but this measurement can be affected by emission filling.

The absence of blue wings on line profiles in our LRIS spectra does not rule out the presence of an outflow due to sensitivity issues caused by instrumental smoothing and the variation in S/N ratio among spectra. The V_{max} measurements should *not* be compared among the entire sample to determine which galaxies have outflows but do serve two useful purposes. First, values of V_{max} blueward of approximately -435 km s^{-1} in 400 l mm^{-1} spectra identify a resolved line wing, as does absorption blueward of roughly -282 km s^{-1} in 600 l mm^{-1} spectra. Second, we can compare the Mg II blue wings among galaxies with different properties by measuring the V_{max} feature in composite spectra constructed to have the same S/N ratio. Previous studies have done this type of analysis at spectral resolution higher our LRIS spectra (Weiner et al. 2009; Rubin et al. 2010b).

3.4.2. Contamination from Stellar Absorption

The analysis of both composite and individual presented in this paper excludes galaxies with colors placing them in the green valley or red sequence or K+A spectral classification. The LRIS spectra of many of these 22 galaxies show significant stellar absorption. The stellar lines become stronger as with the mass of the intermediate age stellar population, so we recognized the contamination by comparing absorption features (from excited states rather than resonance transitions) in spectra of post-starburst galaxies to our spectra. The excited absorption features are absent or weak in our spectra of blue-cloud galaxies.

This rejection affects the measurement of the maximum absorption blueshift because the stellar line profiles have broad wings. We measure high V_{max} values for several of the 22 rejected galaxies. Because these galaxies are mostly in the high mass tertile of our sample, they generate a positive correlation between V_{max} and stellar mass when we include them. Without them, the maximum blueshift of the Mg II $\lambda\lambda 2796, 2803$ absorption in Figure 3 does not vary significantly with stellar mass, B-band luminosity, or color.

In principle, broad stellar line profiles could be differentiated from outflowing gas by the symmetry of the former about the systemic velocity. In practice, however, the Mg II $\lambda 2803$ line is filled in by resonance emission. In Figure 6 for example, visual comparison of the maximum blueshifted Mg II $\lambda 2374$ and the maximum redshifted Mg II 2803 absorption, shows that the latter is often clearly affected by emission filling (e.g., in the cases 12012777, 22013210, and 32011682) leaving a significant excess of absorption on the blue side. Exceptions to this rule include the spectra of 22004858, 22005270, and 42014138, where the symmetry might be used to argue for broad, stellar wings on the line profile. A definitive answer requires fitting the spectra with stellar population models to determine the net difference in stellar ages and is beyond the scope of this paper. However, in general, we think it would be very hard to fill in a red wing from stellar absorption with resonance emission because the emission is narrow compared to the stellar absorption. Hence, it seems clear that high velocity gas is required

¹² The first and second ionization potentials are 0.6 and 1.2 ryd. Their values are $\text{IP}(\text{Mg I}) = 7.646 \text{ eV}$, $\text{IP}(\text{Mg II}) = 15.035 \text{ eV}$, $\text{IP}(\text{Fe I}) = 7.870 \text{ eV}$, and $\text{IP}(\text{Fe II}) = 16.18 \text{ eV}$.

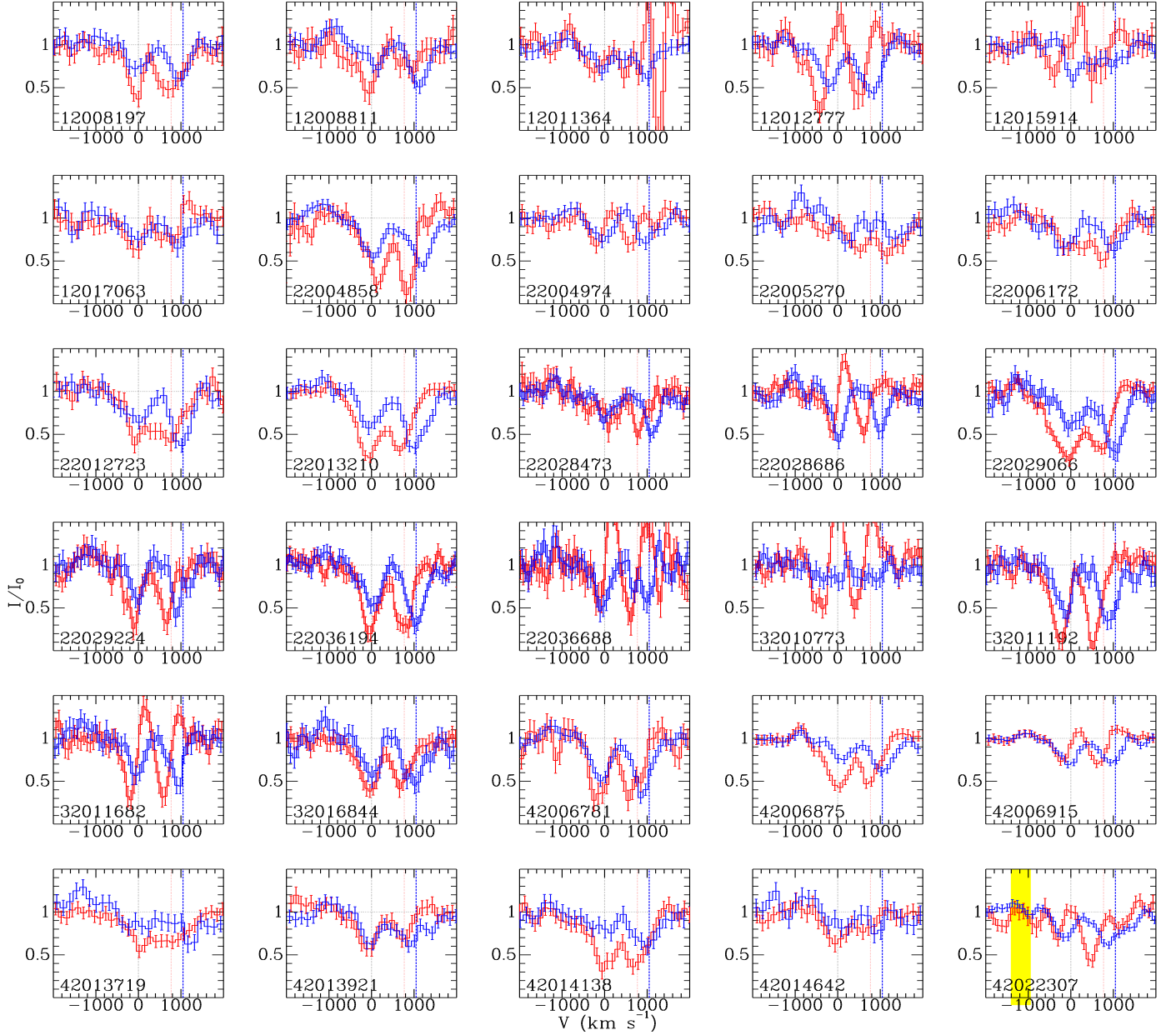


FIG. 6.— Comparison of the blue wings of the Mg II $\lambda 2796$ (red line) and Fe II $\lambda 2374$ (blue line) line profiles. Only spectra with continuum S/N ratio greater than 10 at $\lambda 2450$ are shown. Near Fe II $\lambda 2374$, note the location of Fe II* 2365 at -1124 km s^{-1} (blueward) and Fe II $\lambda 2383$ at 1048 km s^{-1} (redward). Near Mg II $\lambda 2796$, note the Mg II 2803 line at 769 km s^{-1} . Bold, short lines mark v_{max} in both transitions. This comparison illustrates that resonance emission frequently fills part of the Mg II $\lambda 2796$ trough and that the Mg II lines generally have higher equivalent width than the Fe II $\lambda 2374$ line. (The location of strong telluric lines that interfere with measurement of the blue wing are noted in yellow. Spectra with no coverage of one these lines or an unresolved Mg II profile are not shown.) For example, let us consider 42014154, 42014618, and 42021266. Their Mg II $\lambda 2796$ absorption troughs look almost identical to the Fe II $\lambda 2374$ troughs. The largest differences are the Mg II $\lambda 2796$ emission filling the reddest portion of the absorption trough in 42021266 and the Fe II* 2365 emission just past the blue limit of the $\lambda 2374$ trough in 42014618 and possibly 42014154. Emission fills in the absorption trough near systemic velocity in 12012777. Spectra like 12012777 and 22029066 (5th down) present essentially the same v_{max} in Mg II and Fe II.

to produce the blue wings of many Mg II absorption profiles.

4. COMPARISON OF Mg II AND Fe II ABSORPTION TROUGHS

Composite spectra allow comparisons between subsets of galaxies at equal continuum S/N ratio. Before considering individual spectra, it is useful to establish the overall trends between absorption properties and galaxy properties in composite spectra. Table 2 gives the velocity and equivalent width measurements for the composite spectra discussed below. To make the comparison

between individual spectra more meaningful, we focus on 400 l mm^{-1} (600 l mm^{-1}) spectra with continuum S/N ratio greater than 10 (7.7) in this section, excluding the 22 spectra with the strongest stellar absorption (based on their classification as K+A, red-sequence, or green-valley galaxies). Table 3 summarizes the correlations between the absorption measurements for these individual spectra and the galaxy properties.

4.1. Absorption Equivalent Widths

4.1.1. Composite Spectra

In Figure 3, we show composite spectra by tertiles in stellar mass, $U - B$ color, and rest-frame B -band luminosity. The equivalent width of the Mg II absorption increases quite strongly with stellar mass, redder color, and higher B -band luminosity. The lower Mg II equivalent width in the less massive, bluer, and intrinsically fainter galaxies appears to result largely from increased resonance emission filling in the absorption troughs. First, only the composite spectrum of the highest mass quartile of galaxies has a physical ratio of the $\lambda 2796$ to $\lambda 2803$ equivalent widths; composite spectra of the lower mass quartiles have larger equivalent widths in the transition with the lower oscillator strength. Second, the composite spectrum of the lowest masses show a P-Cygni emission line in the Mg II $\lambda 2796$ transition. Third, towards lower mass and bluer color, the absorption is more suppressed in the red wing of Mg II $\lambda 2803$ than it is in the blue wing of Mg II $\lambda 2796$. Since models predict the strongest emission near (and redward of) the systemic velocity, this trend is consistent with emission filling reducing the equivalent width and maximum absorption velocity of the red wing.

The Fe II multiplets in the left and center panels of Figure 3 also show the impact of increased emission filling at lower mass, bluer color, and fainter luminosities. In spectra of lower mass, bluer, and lower luminosity galaxies, the equivalent width of Fe II $\lambda 2383$ decreases much more than that of Fe II $\lambda 2374$. In contrast to what we observed, decreasing the Fe II column density would reduce the equivalent width of Fe II $\lambda 2374$ faster than the Fe II $\lambda 2383$ equivalent width because the Fe II $\lambda 2374$ transition, due to its lower oscillator strength, becomes optically thin when $\tau_0(2383) \approx 10$.

In Figure 4 and in Kornei et al. (2012), we show composite spectra for galaxies with lower and higher SFRs. Robust SFRs have only been measured for the AEGIS subset of our sample, so the S/N ratios of these composites are lower than those in Figure 3. The Mg II EW increases towards higher SFR. The equivalent width evidently increases more strongly with mass than with SFR, however, because the Mg II equivalent width declines with increasing specific SFR in the middle panel of Figure 4.

4.1.2. Individual Spectra

In Figure 6, we overlay the Fe II $\lambda 2374$ and Mg II $\lambda 2796$ absorption profiles. When the absorption troughs are weak, these line profiles can be indistinguishable as seen in the 12011364, 12017063, and 42013921 spectra. Among the better resolved line profiles, however, the absorption trough of the weaker transition (Fe II $\lambda 2374$) is often deeper near the systemic velocity than the Mg II $\lambda 2796$ trough. The prominent Mg II emission in spectra like 12012777, 22028686, 22036688, and 32011682 is clearly the reason why the Fe II trough is deeper. Hence, we argue that resonance emission is filling in the Mg II absorption troughs in spectra like 22004974, 42006915, and 42022307. To summarize, the most striking difference between the Fe II and Mg II line profiles is the paucity of Mg II absorption (relative to Fe II) near the systemic velocity, which we attribute in large part to emission filling.

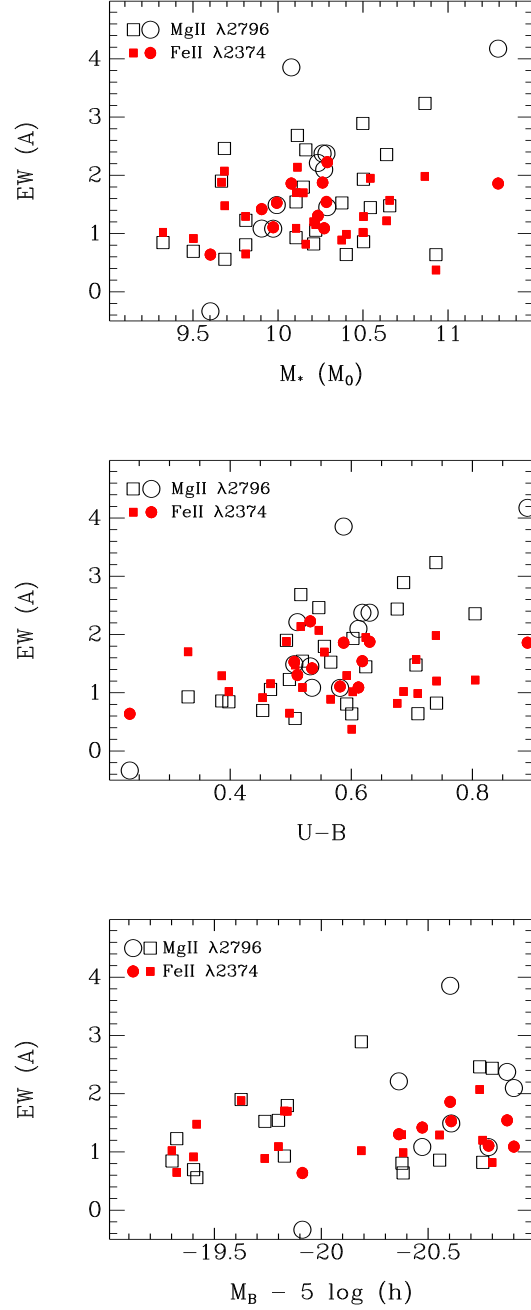


FIG. 7.— Equivalent widths of the Mg II $\lambda 2796$ and Fe II $\lambda 2374$ absorption troughs in individual, high S/N ratio spectra. Squares and circles represent the 400 km s^{-1} and 600 km s^{-1} spectra, respectively. The Mg II equivalent width is positively correlated with stellar mass, color, and B -band luminosity; see Table 3. (To mitigate the impact of emission filling on the Mg II absorption measurement, we have integrated the area of the absorption from -1000 to 0 km s^{-1} .)

Figure 7 shows the absorption equivalent widths measured in these individual spectra over the full range in stellar mass, color, and luminosity. As anticipated from our inspection of the composite spectra, the Mg II equivalent width measurements for individual spectra are also positively correlated with stellar mass, color, and blue luminosity. Among these trends, the correlation with color is both the most significant (2.58 standard deviations

from the null hypothesis) and strongest ($r_s = 0.44$). The Mg II absorption equivalent width is significantly more correlated with these galaxy properties than is the Fe II $\lambda 2374$ equivalent width; i.e., comparison of columns 3 and 4 in Table 3 quantitatively confirms the impression obtained from the composite spectra in this regard. Even though the Mg II equivalent width is correlated with the Fe II equivalent width, the ratio $W(2796)/W(2374)$ increases towards redder, more massive galaxies.

In column 2 of Table 3, we show that the Doppler shift of the Fe II absorption has a negative correlation with specific SFR. Since our sign convention assigns negative velocities to Fe II blueshifts, the Fe II absorption is more blueshifted in galaxies that are undergoing a more significant episode of star formation. This correlation with specific SFR supports the expectation that the blueshifts mark galactic outflows.

We might expect larger blueshifts to generate broader lines and therefore have larger Fe II equivalent width; but the measured correlation is in the opposite sense. The Doppler shift V_1 (from single-component fitting) is positively correlated with the Fe II $\lambda 2374$ equivalent width – a trend that may arise, for example, from a significant interstellar absorption component at the systemic velocity.

4.1.3. Implications of Emission Filling

In this section, we have presented evidence for increased emission filling in lower mass, lower luminosity, bluer galaxies. Since more massive galaxies are dustier on average, the reduced emission in high mass galaxies is consistent with a simple picture. Resonant photons are less likely to escape from a dustier galaxy, so we see less emission filling in spectra of more massive, and dustier, galaxies. We find examples of good agreement between the shape of the Mg II and Fe II absorption troughs among individual spectra, so we conclude that the emission is sometimes strongly suppressed. Even though $U - B$ color is correlated with reddening, we cannot directly conclude the increased emission filling in bluer galaxies is due to a lower dust content because the color is also very sensitive to age. Dust is a plausible, but a not a required, explanation.

Viewing geometry is another way to select for (or against) emission. By exploring several outflow geometries, for example, Prochaska et al. (2011) show that line emission is weaker in more collimated outflows where the half-opening angle of the outflow cone, θ_B , is less than 45° instead of 90° (i.e., spherical). Emission is also suppressed by dust attenuation, which can be enhanced several ways. Besides simply increasing the dust-to-gas ratio, adding absorption from the interstellar medium to the calculation reduces the number of emission-line photons, thereby reducing the emission filling. Hence, we expect the absorption line profiles in Mg II to track those of Fe II $\lambda 2374$ and 2587 most closely when some set of these conditions are met: strong ISM absorption, dusty galaxies, and/or smaller opening angles for the outflows.

4.2. Identifying Fast Outflows with Mg II Absorption

In some spectra, such as 22013210, 22029066, and 32011682, the Mg II absorption is detected to significantly higher blueshifts than is Fe II. At the same time, the maximum blueshifts of the Mg II and

Fe II absorption are consistent in many spectra even though $W(\text{Mg II } 2796) \gg W(\text{Fe II } 2374)$, e.g., 12008197, 22004858, 22012723, and 42006781. Overall, we find no significant correlations between V_{max} and mass ($r_s = -0.31; 1.8\sigma$) or color ($r_s = -0.21; 1.2\sigma$) among the individual spectra, consistent with the lack of any trend in the composite spectra constructed by these galaxy properties. In addition, the Fe II Doppler shift is not significantly correlated with $V_{max}(\text{Mg II})$; and $V_1(\text{Fe II})$ has the stronger correlation with SFR and specific SFR. We summarize our observations as follows: (1) nearly all of the high S/N ratio spectra show a blue wing indicating outflowing material; (2) spectra with a blueshifted Fe II centroid usually show Mg II absorption at highly blueshifted velocities; but (3) roughly half of the spectra with Mg II absorption at a large blueshift do not show a net blueshift of the centroid of the Fe II absorption.

Among the high S/N ratio spectra, the equivalent widths of the Mg II absorption troughs tend to be larger when the absorption extends to higher blueshifts ($r_s = -0.45$ at 2.64σ in Table 3). We measured the Mg II $\lambda 2796$ equivalent width by integrating the line profile from the systemic velocity blueward 1000 km s^{-1} . Defined this way, the equivalent width ranged from 0.25 to 1.0 times the total equivalent width integrated over the emission and absorption in both transitions. For the purpose of measuring the outflow equivalent width, and velocity range, this definition mitigates the impact of emission filling allowing a more direct comparison among spectra. The correlation between equivalent width and maximum absorption blueshift suggests that higher equivalent widths require larger spreads in velocity (rather than larger column densities).

Figure 6 compares the Mg II and Fe II line profiles in spectra with high continuum S/N ratio. Most galaxies with 3σ blueshifts of the Fe II lines show a resolved blue wing on the Mg II profile. The blue wing in these spectra is typically detected in Mg II to velocities more than twice the fitted single-component Fe II velocity. In spectra where the $V_{max}(\text{Mg II})$ and $V_1(\text{Fe II})$ measurements differ, the Mg II $\lambda 2796$ absorption is detected to larger blueshifts, as expected at low gas column densities. It is difficult to determine, however, whether the Fe II centroid fitting fails to identify some galaxies with outflowing gas. Some spectra, for example, have a well detected blue wing of Mg II even though the centroids of their Fe II profiles do not show a significant outflow; these include 7 among the nine 3σ -inflow galaxies whose spectra will be discussed in a Section 6. In the absence of broad line wings from stellar absorption, measurements of this maximum absorption velocity, V_{max} , may be more directly related to the physical speeds in galactic outflows than the centroid of the Mg II absorption trough.

Among the composite spectra shown in Figure 3, the wavelengths where the Fe II absorption troughs meet the continuum do not vary with stellar mass, B -band luminosity, color, SFR, or specific SFR. In Table 2, the most significant change in $V_{max}(\text{Mg II})$ is with the Doppler shift of the Fe II absorption. A composite spectra built from individual spectra with significant (3σ) Fe II absorption blueshifts show Mg II absorption at larger blueshifts than does the typical spectrum with redshifted Fe II absorption. In the bottom panel of Figure 4, we show the Mg II absorption at large blueshifts in the com-

posite spectrum constructed from the individual spectra with the most significant Fe II outflows. The composite spectrum of the 3σ outflow galaxies has an Fe II Doppler shift of $-119 \pm 6 \text{ km s}^{-1}$. This outflow composite shows Mg II absorption out to $-901 \pm 99 \text{ km s}^{-1}$. The $V_{\text{max}}(\text{Mg II})$ of the outflow composite is higher than that of the mass or luminosity composites, so we argue that (at least among star-forming galaxies) higher velocity outflowing gas is the most likely reason for the blue wings on the Mg II profiles. In Kornei et al. (2012), we further show that $V_{\text{max}}(\text{Mg II})$ becomes more blueshifted in composite spectra as the surface density of star formation increases.

5. GAS OUTFLOWS

Resonance absorption lines from Mg II and Fe II are the primary near-UV spectral diagnostics of galactic outflows. At spectral resolutions of a 285 to 435 km s^{-1} , we can robustly measure the Doppler shifts and equivalent widths of the absorption troughs in nearly all spectra. A net blueshift of the transitions that decay primarily by fluorescence, $V_1(\text{Fe II})$, best identifies net outflows of low-ionization gas. The maximum blueshift of the absorption in the strongest line, Mg II $\lambda 2796$, provides a complementary diagnostic of the outflow when spectrally resolved.

To describe the demographics of outflows in Section 5.1, we introduce a methodology for computing the fraction of spectra showing blueshifted Fe II absorption or blue absorption wing in Mg II and examine how the outflow fraction varies with galaxy properties. We then discuss the outflow properties and how they depend on galaxy parameters in Section 5.2, and Section 5.3, respectively.

5.1. Demographics of Outflow Galaxies

Since blueshifts mark gas with a net outflow relative to the stellar system, we want to compute the fraction of galaxies with Fe II blueshifts in order to determine which galaxies host outflows. The challenge is that a blueshifted line detected in a high quality spectrum is not necessarily detectable in a lower quality spectrum. We illustrate this problem Section 5.1.1 and introduce a statistical method for quantifying the prevalence of outflows in Appendix A. We discuss the results in Section 5.1.2.

5.1.1. Fraction of Galaxies with Net Flows

Figure 8 shows a histogram of continuum S/N ratio. As anticipated, at increased spectral S/N ratio, a higher fraction of net outflow (and inflow) galaxies are detected. The continuum S/N ratio is not significantly correlated with B -band luminosity, stellar mass, color, or SFR; hence spectral sensitivity rather than galaxy properties shape this growth in the outflow fraction. The continuum S/N ratio is anti-correlated with the apparent B magnitude of the galaxy (4σ deviation from the null hypothesis), but the correlation is not very strong ($r_S = -0.32$) for two reasons: the galaxies have a range of sizes, and the observations were obtained under a wide range of conditions. Since the sample selection was by apparent magnitude, the anti-correlation between S/N ratio and redshift is not very significant.

Spectral resolution also influences whether a Doppler shift is detected. At the same S/N ratio (per pixel),

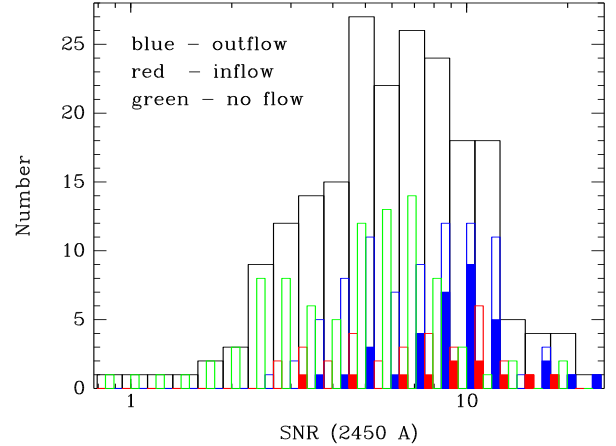


FIG. 8.— Histogram of continuum S/N ratio measured between 2400Å and 2500Å (computed from the full sample of 208 galaxies). Outflows/inflows are selected by the sign of the Doppler shift, V_1 , fitted to the Fe II absorption troughs. The more secure 3σ blueshifts/redshifts are denoted by the solid histograms, and a more generous 1σ cut denoted by the extended open histogram of the same color. Among the full sample of 208 spectra, the fraction of Fe II outflows is very sensitive to the sample's distribution of S/N ratios. Net flows at the 3σ confidence level are extremely rare in spectra with $SNR < 5$; yet their fraction grows to about 58% at $SNR \approx 9$ (36% with S/N ratio > 9). A significant fraction of high S/N ratio spectra present no net flow.

a 600 l mm^{-1} spectrum is more likely to yield a net Doppler shift than a 400 l mm^{-1} spectrum because the higher resolution improves sensitivity to small Doppler shifts. For a Gaussian line profile, for example, the spectral resolution and continuum S/N ratio together determine how well we can find the centroid of a single line; this is the standard deviation of the mean, $SDOM \approx \sigma/SNR$, where the standard deviation σ is 1.54 times larger for the 400 l mm^{-1} spectra than the 600 l mm^{-1} spectra; but these sensitivity differences are partly offset by the fact the lower resolution 400 l mm^{-1} subsample includes higher S/N ratio spectra than does the 600 l mm^{-1} subsample. In summary, for single lines in our best 400 l mm^{-1} and 600 l mm^{-1} spectra, this statistical error is similar – about $\delta V \approx 185/25 \approx 7 \text{ km s}^{-1}$ and $\delta V \approx 120/10 \approx 10 \text{ km s}^{-1}$, respectively. The statistical error on V_1 is reduced further by fitting multiple lines. In practice, Doppler shifts $|V_1| < 41 \text{ km s}^{-1}$ in our data are dominated by systematic errors, and we do not attempt to measure the outflow fraction at these low speeds.

In Appendix A, we describe a methodology for calculating outflow fraction that takes into account the detection biases introduced by the variations in S/N ratio and resolution among our spectra. Rather than arbitrarily picking a minimum Doppler shift to define an outflow, we consider *threshold velocities* ranging from the largest blueshift measured down to the minimum Doppler shift that we can reliably measure, roughly 41 km s^{-1} . We assign to each spectrum a probability that the Doppler shift of the low-ionization gas is larger than a threshold velocity. Finally, we obtain the outflow fraction for that threshold velocity by averaging these probabilities over the entire sample computing the uncertainty directly

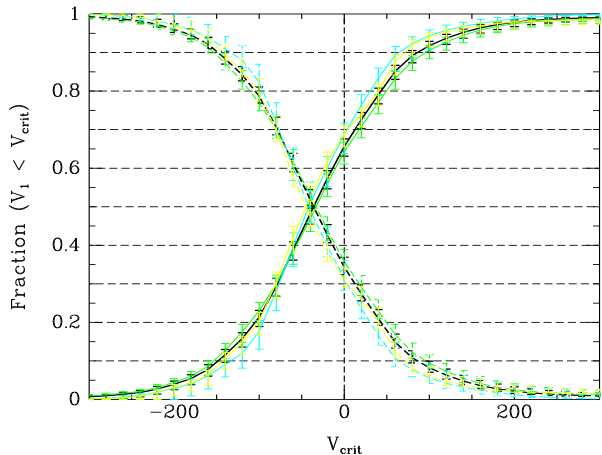


FIG. 9.— Fraction of spectra with a net Doppler-shift of the Fe II lines for four samples. The solid lines show fraction of blueshifted spectra with $V_1 < V_{crit}$; and the dashed lines illustrate the complementary quantity, the fraction of galaxies with $V_1 > V_{crit}$. The dominance of net outflows (65%) over net inflows (35%) is apparent at $V_{crit} = 0$; and the fraction of galaxies with $V_1 < V_{crit}$ (solid line) rises steadily as the threshold speed for an outflow decreases. The black, green, cyan, and yellow curves show the results of the calculation defined in Appendix A for the following subsamples, respectively: all spectra, all 400 l mm^{-1} spectra, all 600 l mm^{-1} spectra, and the highest quality spectra defined as $S/N > 8.5(6.5)$ for 400 l mm^{-1} (600 l mm^{-1}). Since the curves for these four samples give consistent results, this method of calculating the outflow and inflow fractions appears to do a good job of correcting for the wide range in spectral S/N ratio and our two spectral resolutions. The error bars show the 68.27% confidence interval. To the extent that these galaxies all have similar properties, we can interpret the variation of outflow fraction with speed as an indication of the relative solid angles subtended by outflowing gas at different speeds.

from the probability distribution. This definition of outflow fraction is quite general and can be applied under a broad range of circumstances. For example, the Doppler shift may represent the fitted Fe II centroid velocity V_1 , the Doppler shift of the blue wing of the Mg II absorption trough V_{max} , or the velocity derived from a more complex model. This methodology can also be applied to describe the inflow fraction if we use the net Doppler shift or velocity of the red wing of a line profile.

In Figure 9, we show the outflow and inflow fractions computed for four samples. Roughly 5%, 20%, and 45% of the spectra in our full sample (black lines) show Fe II blueshifts faster than -200 km s^{-1} , -100 km s^{-1} , and -50 km s^{-1} , respectively. In contrast, less than 8% of the spectra have redshifts higher than 90 km s^{-1} . Repeating the analysis with just the highest S/N ratio spectra (yellow lines), we obtain the same result. Similarly, with the sample restricted to either the lower resolution (400 l mm^{-1}) spectra or the higher resolution (600 l mm^{-1}) spectra, the outflow fraction remains consistent with the results obtained for the full sample. This test demonstrates that our results for the outflow fraction are insensitive to S/N ratio and spectral resolution. Because many more of the LRIS spectra have blueshifts than redshifts, the results for the outflow fraction are better constrained (than for inflow) and we describe the outflow results in Section 5.1.2.

5.1.2. Dependence of Outflow Fraction on Galaxy Properties

We apply the computational method introduced here to compare the outflow fraction among galaxies with different properties. We divide our sample into tertiles (thirds) by redshift, mass, color, luminosity, and SFR. To obtain insight about the importance of starbursts, we also normalize the SFR by the stellar mass; this specific SFR is the reciprocal of the timescale required to assemble the stellar mass at the current SFR. We present the fraction of galaxies with a blueshifted Fe II centroid velocity and then compare to the fraction of galaxies with significant blue absorption wings in Mg II. It is important to keep in mind that all the galaxies in our sample are star-forming galaxies; the post-starburst, green valley, and red sequence galaxies are excluded from this analysis.

The galaxy properties measured for DEEP2 galaxies were a primary motivation for our study. Stellar mass is perhaps the most fundamental property measured for the entire sample; and relative masses are determined to within a factor of two (Bundy et al. 2006). Measurements of B -band luminosity and $U - B$ color are described in Willmer et al. (2006) for the full sample. Star formation rates have been measured for 51 galaxies in our LRIS sample. In Kornei et al. (2012), we show that these extinction-corrected SFRs (derived from GALEX imaging of the AEGIS field) agree with the sum of the SFRs derived from uncorrected UV and $24 \mu\text{m}$ photometry.

In Figure 10, we show the fraction of spectra with V_1 bluer than V_{crit} . The outflow fraction measured this way is clearly independent of stellar mass. The outflow fraction is enhanced among galaxies in the highest tertile by SFR (relative to the lowest tertile). The largest variation with galaxy properties, however, is seen between the tertiles with the highest and lowest specific SFRs. Outflows faster than roughly 100 km s^{-1} are nearly absent at low specific SFR, $-10 < \log s\text{SFR} (\text{yr}^{-1}) < -9.15$. Among galaxies with high specific SFR, $-8.8 < \log s\text{SFR} (\text{yr}^{-1}) < -8.2$, the fraction of galaxies with Fe II Doppler shifts (from -200 to -100 km s^{-1}) is boosted by up to a factor of 1.8 relative to the entire subsample with measured SFR.

In the LRIS sample, B -band luminosity is more significantly correlated with SFR (6.1σ from the null hypothesis, $r_S = -0.87$) than is any other galaxy property.¹³ Hence, within the full LRIS sample, we might expect to find the outflow fraction elevated among the more luminous galaxies. In Figure 10, the outflow fraction is indeed highest at all V_{crit} for the most luminous galaxies, but the significance of the distinction is hardly compelling ($\lesssim 1\sigma$).

The high specific SFR galaxies have bluer colors on average (4.1σ from the null hypothesis, $r_S = -0.58$). Since we find a higher outflow fraction among galaxies with high specific SFR, we might expect an enhanced outflow fraction among bluer galaxies in the full sample. From Figure 10, we simply note that any enhancement in outflow fraction with bluer color is weaker than the marginal one seen with B -band luminosity. These results

¹³ A weaker correlation of somewhat lower significance is found between SFR and stellar mass (4.3σ from the null hypothesis, $r_S = 0.61$).

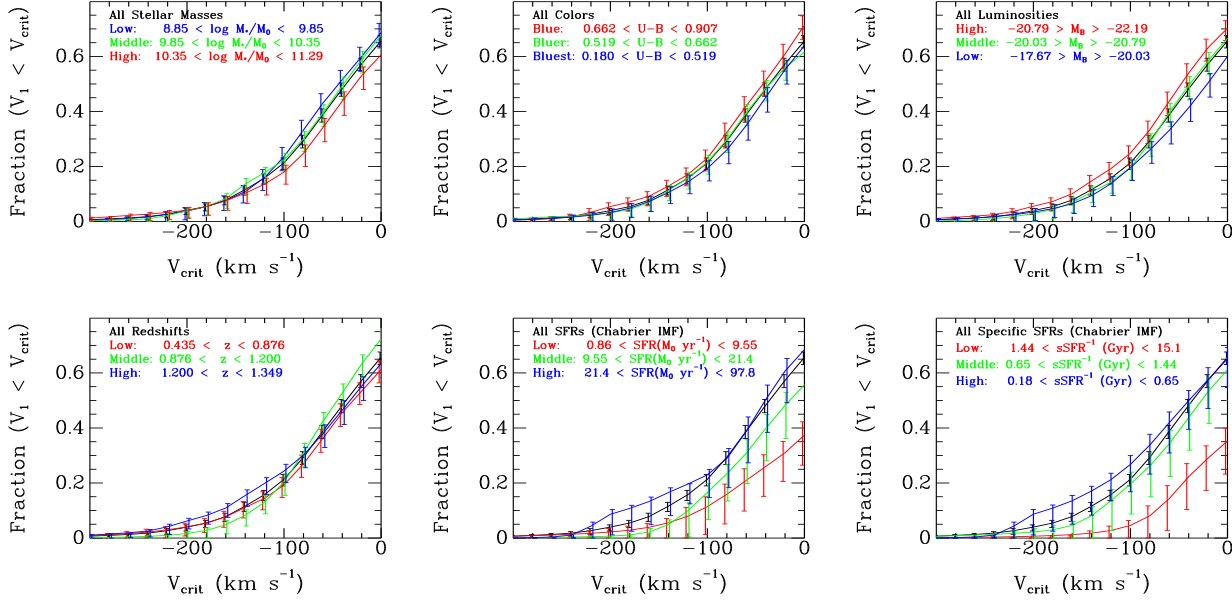


FIG. 10.— Fraction of galaxies with V_1 bluer than V_{crit} . This measure of the outflow fraction shows no dependence on stellar mass (upper left). The outflow fraction is slightly higher among higher luminosity galaxies (middle left) and higher redshift galaxies (middle right). In the velocity range $-250 < V_1 < -100$, the outflow fraction among the galaxies in the highest SFR tertile ($34 < SFR(\text{M}_\odot \text{ yr}^{-1}) < 175$) is about a factor of four higher than the outflow fraction measured among the galaxies in the lowest SFR tertile ($1.5 < SFR(\text{M}_\odot \text{ yr}^{-1}) < 17$). Among the galaxies with the lowest specific star formation rates ($-10 < sSFR(\text{Gyr}^{-1}) < -9.15$), outflows appear to be strongly suppressed at all velocities relative to the average. The outflow fraction is enhanced by a factor of 1.8 over the average among the tertile of galaxies with the highest sSFRs ($-8.8 < sSFR(\text{Gyr}^{-1}) < -8.2$). The calculation of the outflow fraction follows the methods outlined in Appendix A.

are consistent with outflow fraction depending primarily on specific SFR, and color being strongly dependent on galaxy luminosity and mass as well as specific SFR. In light of the increasing outflow fraction with specific SFR, the absence of any variation in the outflow fraction over the redshift range from 0.4 to 1.4 deserves further inspection because galaxies have larger SFRs and specific SFRs at higher redshift.

The three redshift tertiles for the LRIS sample with GALEX photometry are shown in the SFR – stellar mass plane in Figure 11. We show the $SFR - M_*$ main sequence (Noeske et al. 2007; Elbaz et al. 2007) fitted to the GALEX-detected subsample of 6102 DEEP2 galaxies with stellar mass measurements. The specific SFRs of the galaxies with Fe II blueshifts are 1σ larger than the average sSFR at the same stellar mass. Furthermore, the main sequence fitted to the GALEX-detected subsample is entirely consistent with our fit to the SFRs and stellar masses estimated for the full sample of blue cloud galaxies in DEEP2 (Mostek et al. 2011).¹⁴ We can therefore conclude that the galaxies with Fe II blueshifts have slightly higher sSFR than the typical blue cloud galaxy.

Among our subsample of galaxies with measured SFRs, only galaxies with $sSFR > 0.8 \text{ Gyr}^{-1}$ show secure, 3σ blueshifts. Since the slope of the main sequence is less than unity, the typical sSFR falls gradually with

increasing stellar mass and this may explain why the Fe II blueshifts will be detected up to larger stellar masses at higher redshift. A sSFR threshold for Fe II blueshifts around 0.8 Gyr^{-1} would explain the paucity of 3σ blueshifts in the low redshift tertile. Inspection of Figure 11, however, shows that not all galaxies with high sSFRs have blueshifted Fe II absorption in their spectra. Hence, it will be important to measure SFRs for the remainder of the LRIS sample and determine whether the minimum sSFR criterion remains a necessary condition for seeing blueshifted Fe II absorption in galaxy spectra.

Given the distinct shapes of the Fe II and Mg II absorption troughs in some spectra, we compare the demographics of galaxies with blueshifted Fe II absorption and those with highly blueshifted Mg II absorption. Figure 12 shows the fraction of galaxies with Mg II absorption at blueshifts larger than a threshold velocity, V_{crit} . Once again (as for Fe II blueshifts), galaxies with high specific SFR appear more likely to show highly blueshifted Mg II absorption in their spectra; the fraction of spectra with highly blueshifted Mg II absorption (as measured by $V_{max}(\text{Mg II})$) shows no trend with redshift. In contrast to the case for Fe II blueshifts, however, the outflow fraction derived from the Mg II blue wing shows not even a weak dependence on SFR alone.

While the outflow fraction curves in Figure 12 are highest for galaxies with higher masses, higher luminosity, and redder color, the enhancement with each of these properties is not statistically significant. The larger error bars in Figure 12 relative to Figure 10 arise from not all spectra showing resolved Mg II absorption troughs (and therefore no V_{max} estimate). Within the measurement uncertainties, however, we conclude that the fraction of galaxies with outflows as determined by $V_{max}(\text{Mg II})$ ap-

¹⁴ Mostek et al. (2011) use the AEGIS data to calibrate the results of SED fitting to optical photometry. Comparison of this SFR – stellar mass relation to previous work is complicated by differences in both redshift range and methods used to derive stellar mass and SFR. For example, the Noeske et al. (2007) relation was measured at lower redshift $0.2 < z < 0.7$, which may explain why our fit is about ~ 0.2 dex higher with similar slope. For our subsamples at $0.842 < z < 1.349$, the SFR – stellar mass relation in DEEP2 is remarkably shallower in slope than the Elbaz et al. (2007) relation fitted at $0.7 \leq z \leq 1.2$.

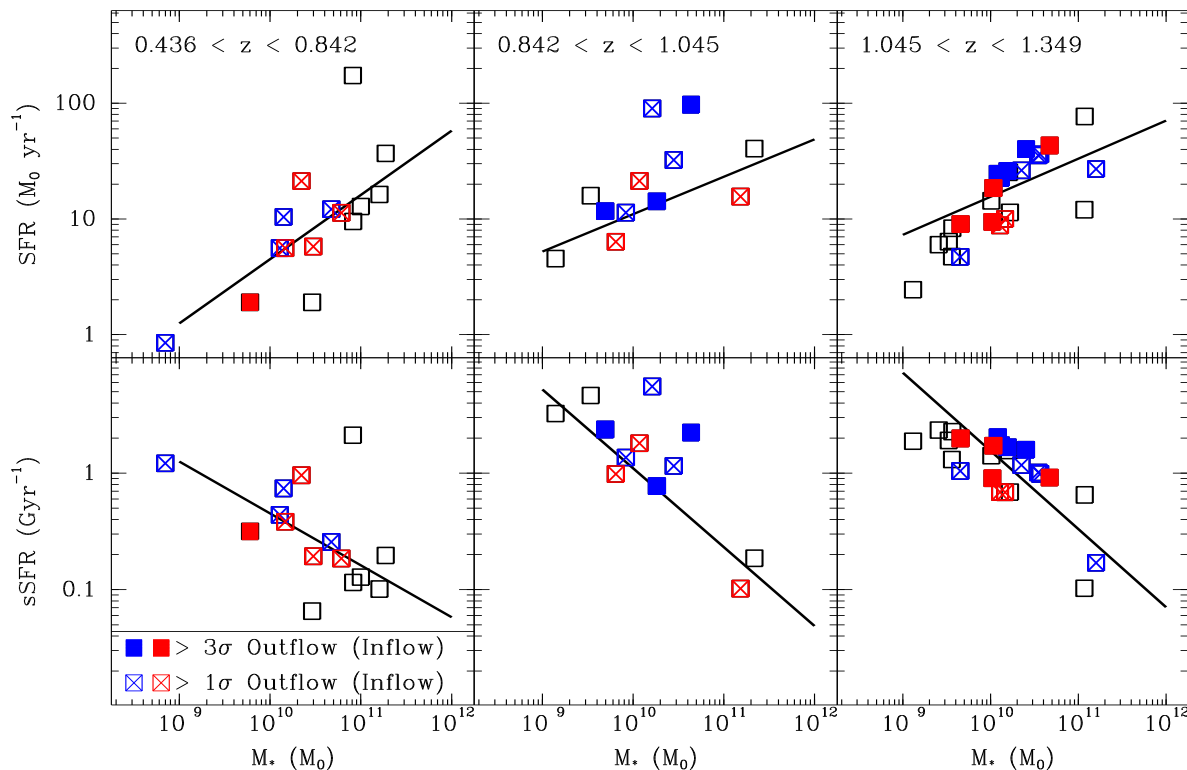


FIG. 11.— Location of galaxies with Fe II blueshifts in the $SFR-M_*$ and $sSFR-M_*$ diagram. The UV-corrected SFRs have been divided by 1.8 to put both the SFR and stellar mass on a Chabrier IMF. Within each redshift tertile, the bold (red) line marks the main sequence of star-forming galaxies fitted to the subsample of DEEP2 galaxies with GALEX photometry. We excluded galaxies with $U - B$ redder than the green valley, i.e., $U - B > 1.135 - 0.032(M_B + 21.18)$, and fitted the main sequence using an iterative clipping routine. The slope of the best fit flattens a bit from the lowest redshift data ($\log\langle SFR \rangle = 0.5419 \log\langle M_* \rangle - 4.7255$) through the middle redshift tertile ($\log\langle SFR \rangle = 0.4020 \log\langle M_* \rangle - 2.9337$) to the highest redshift spectra ($\log\langle SFR \rangle = 0.2975 \log\langle M_* \rangle - 1.7488$). The galaxies with the most robust Fe II blueshifts (3σ , solid) all lie on or above the main sequence as do most galaxies with 1σ (open symbols with cross) blueshifts.

appears to be less dependent on SFR than the outflow fraction determined by $V_1(\text{Fe II})$. Furthermore, both of these outflow indicators are remarkably insensitive to other fundamental galaxy parameters including stellar mass, B -band luminosity, color, and redshift.

5.2. Physical Properties of Outflows

The properties of winds have generally been varied in cosmological simulations in order to fit observations of fundamental galaxy properties such as stellar content, SFR, and metallicity evolution (Davé, Oppenheimer, & Finlator 2011a; Davé, Finlator, & Oppenheimer 2011b). Direct measurements of outflow velocity and mass flux are therefore of great importance for modeling galaxy formation and evolution. Here we discuss the measured Doppler shifts and the Fe II column densities. We will illustrate plausible extrapolations to the wind velocity and mass flux but emphasize that, in order to accurately model the interplay of the various gas phases, well-resolved simulations of galactic outflows need to be projected into the quantities we observe.

The escape of metals from low-mass galaxies in the local universe has been established empirically (Martin 1999; Martin et al. 2002; Tremonti et al. 2007). This enrichment of the circumgalactic medium by winds prob-

ably started very early in cosmic history based on the properties of metal-line systems at high-redshift (Meyer & York 1987; Lu 1991; Songaila & Cowie 1996; Ellison et al. 2000; Schaye et al. 2003; Simcoe et al. 2006; Martin et al. 2010; Simcoe 2011). The main question is whether these outflows transport substantial mass. The winds clearly affect the chemical evolution of galaxies, but their role (if any) in creating the observed baryon deficit remains unclear (e.g., McGaugh et al. 2010).

Since we use low-ionization metal lines to identify the blueshifted absorption, our survey does not probe the hot phase of a galactic wind. The low-ionization gas is entrained in the hot wind by the breakup of supershells (Fujita et al. 2009), the shear between the free wind and the galactic ISM (Heckman et al. 2000), and pre-existing, interstellar clouds (Cooper et al. 2008, 2009). The relationship between this warm gas and hot wind fluid is critical to any extrapolation of our measurements to the wind properties. In the recent Hopkins et al. (2012) simulation of a high-redshift galaxy (which has properties typical of our sample) however, the warm, low-ionization gas carries the bulk of the outflowing gas mass; hence we are likely observing the dominant phase of the wind (by mass). The mass-loss rates derived from low-ionization gas should still be viewed as lower limits on the mass

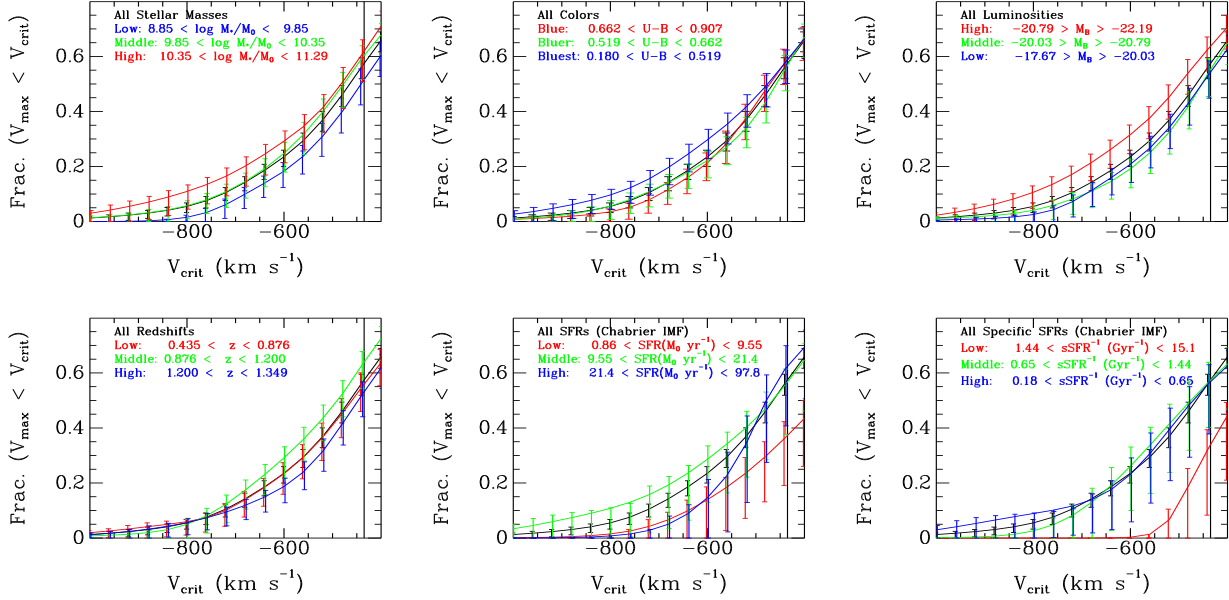


FIG. 12.— Fraction of galaxies with Mg II absorption detected at velocities larger (bluer) than threshold velocity, V_{crit} , adopted to define an outflow. The black curve shows the entire sample with Mg II measurements; and the colored curves break this sample into tertiles by galaxy properties. The V_{max} measurements have not been corrected for instrumental smoothing of the line profile and measure only the instrumental profile at blueshifts less than -435 km s^{-1} (vertical line in each panel) in the 400 m m^{-1} spectra; hence the curves have no significant meaning as this limit is approached from larger blueshifts. A high velocity blue wing is most prevalent among higher mass, higher luminosity, and redder galaxies and does not depend on the SFR.

flux in the multiphase wind; for example, inspection of the other types of galaxies in Figure 4 of Hopkins et al. (2012) shows that the hot wind fluid can carry most of the mass at some outflow velocities.

5.2.1. Outflow Solid Angle

The measurements presented in Section 5.1.2 provide a statistical characterization of which galaxies have spectra with blueshifted low-ionization absorption. Among the various velocity measurements discussed, we have argued that the net Doppler shift of the Fe II lines provides the most robust indication of a net outflow of gas along the sightline. We find that some high S/N ratio spectra of star-forming galaxies show no net outflow. Moreover, the outflow fraction varies very little among the tertiles in each galaxy parameter. The largest variations in outflow fraction are only a factor of two even though the stellar masses of the observed galaxies span more than 2 dex. We therefore make the conjecture that the spectra without Fe II blueshifts are galaxies viewed along a sightline perpendicular to the outflow direction. Additional support for this interpretation comes from the inclinations of the AEGIS galaxies. In Figure 20 of Kornei et al. (2012), we show that the five spectra with 3σ blueshifts of the Fe II lines are found for galaxies viewed face-on, i.e. $i < 45^\circ$. In this scenario, the outflow fraction may be interpreted in terms of the solid angle of the outflow.

For example, we consider a spherical outflow geometry. Let θ_B be the half-angle of a conical outflow, then the outflow subtends a solid angle

$$\Omega = 4\pi(1 - \cos \theta_B), \quad (10)$$

and will be detected in a fraction $\Omega/4\pi$ of the galaxies we observe. An important aspect of our analysis is that the outflow fraction is measured as a function of velocity in Figure 9, which suggests that outflows have a smaller

opening angle at higher velocity. Smaller opening angle at higher velocity is qualitatively consistent with dynamical simulations of outflows where the opening angle is determined by the scale-height of the ISM (DeYoung & Heckman 1994).

Our study provides this first evidence for highly collimated outflows at $z \sim 1$. In Figure 9, we show that the fraction of spectra with blueshifts increases as V_{crit} decreases. Specifically, we measure an outflow fraction of 0.025, 0.20, 0.45, and 0.65 at $V_{crit} = 200, 100, 50$, and 0 km s^{-1} , respectively. The half-angle of the outflow cone would be $13^\circ, 37^\circ, 57^\circ$, and 70° at velocities of 200, 100, 50, and 0 km s^{-1} . Hence our results indicate that the outflows subtend a larger (smaller) solid angle at slower (faster) speeds. Also, at all speeds, the outflow solid angle is much less than 4π steradians. While bipolar outflows are well documented at lower redshift (e.g., Heckman et al. 1990; Chen et al. 2010; Bouché et al. 2012), only recently has evidence for outflow collimation emerged at redshifts from $0.09 < z < 0.9$ (Bordoloi et al. 2011; Kacprzak et al. 2012).

The polar angle of $\theta_B \approx 37^\circ$ for the outflow at 100 km s^{-1} derived from our results appears to be consistent with the distribution of outflowing gas in galactic halos. Bordoloi et al. (2011) mapped the Mg II absorption at impact parameters (to background galaxies) within 40 kpc of star-forming galaxies at $0.5 < z < 0.9$. Around blue, star-forming galaxies, the Mg II absorption equivalent widths are significantly higher at small polar angles, near the minor axis, than those measured closer to the major axis. Their results suggest the outflow cone makes an angle of 45° or less with the minor axis of the galaxy.

5.2.2. Mass Outflow Rates

We have nearly enough information to measure the mass flux in the low-ionization outflow. As described in Section 3.3.3, our measurements bound the Fe II column density on both sides; this is a significant improvement over previous studies that detected outflows only in saturated lines, which yield only lower bounds. We have also shown that the largest Doppler shifts in Fe II are roughly 200 km s^{-1} and provided some evidence that slower outflows may be simply viewed at higher inclinations (Kornei et al. 2012); this result constrains the outflow solid angle, Ω . The ionization correction for Fe II is uncertain but seems likely to lie in the range $\chi(\text{Fe}^+) \equiv n(\text{Fe}^+)/n(\text{Fe}) = 0.1 - 1$ based on photoionization modeling (Churchill et al. 2003; Murray et al. 2007). In the halo gas of the Milky Way, the measured depletion of iron onto grains is much lower than its value in the cold disk; hence we conservatively take $\log d(\text{Fe}) \equiv [\text{Fe}/\text{H}] = -0.69$ from Table 6 of Savage & Sembach (1996) as our best estimate of the depletion. For a spherical flow launched at radius R_0 , the mass flux is

$$\dot{M} = \Omega v R_0 N(H) \bar{m}, \quad (11)$$

where the average mass per hydrogen atom is $\bar{m} = 1.4 \text{ amu}$, Ω represents the solid angle subtended by an outflow with spherical geometry, v is the radial velocity of the outflow, and $N(H)$ the total hydrogen column density.

The galaxy spectra do not uniquely constrain the location of the gas along the sightline. In a radially diverging flow, the column density integral “down the barrel” will be dominated by the densest gas near the launch radius; hence, the linear dependence of the mass flux on the launch radius in Eqn. 11. Simple models relate R_0 to the size of the starburst region (Chevalier & Clegg 1985) and/or several pressure scale heights in a gaseous disk (De Young & Heckman 1994). We therefore assume that $R_0 \lesssim 1 \text{ kpc}$ in order to illustrate the mass fluxes. Some of the absorbing gas is clearly at much larger radii based on the detection of spatially extended Mg II emission (Rubin et al. 2011a; Erb et al. 2012; Martin et al. 2012b, in prep) and intervening Mg II absorption at impact parameters $b \leq 70 \text{ kpc}$ (Bordoloi et al. 2011).

Using the bounds on the Fe II column from Table 5, we note that the total “ISM plus outflow” column is less than $\log N(\text{Fe}^+) (\text{cm}^{-2}) \lesssim 15.8$ in half the outflow galaxies, and the highest upper limit is 16.27. Expressing Eqn. 11 in terms of some favorable, but reasonable, parameter estimates yields

$$\begin{aligned} \dot{M} = & 23 \text{ M}_\odot \text{ yr}^{-1} \left(\frac{\Omega}{\pi} \right) \left(\frac{V}{200 \text{ km s}^{-1}} \right) \\ & \times \left(\frac{R_0}{1 \text{ kpc}} \right) \left(\frac{N(\text{Fe}^+)}{10^{16} \text{ cm}^{-2}} \right) \left(\frac{3.16 \times 10^{-5}}{n(\text{Fe})/n(\text{H})} \right) \\ & \times \left(\frac{0.5}{\chi(\text{Fe}^+)} \right) \left(\frac{0.20}{d(\text{Fe})} \right). \quad (12) \end{aligned}$$

For comparison, the median SFR in the AEGIS subsample is $12.3 \text{ M}_\odot \text{ yr}^{-1}$ for a Chabrier IMF (or, $21.9 \text{ M}_\odot \text{ yr}^{-1}$ for a Salpeter initial mass function), indicating a mass loading parameter $\eta \equiv \frac{\dot{M}}{\text{SFR}} \approx 1.1(1.9)$. If $\chi(\text{Fe}^+)$ approaches 0.1, then the mass loading factor η is five times higher than in Eqn. 12.

Interstellar gas in these galaxies almost certainly accounts for some of the absorption equivalent width. As we discussed in Section 3.3.2, models with multiple velocity components are not well constrained by our low resolution spectra. However, using a model that describes the ISM absorption at the systemic velocity with the maximum equivalent width consistent with the velocity dispersion (of emission lines) and shape of the absorption trough (corrected for the instrumental smearing), we were able to illustrate the typical properties of the Fe II absorption in the Doppler component. From Table 5, the column density in the Doppler component is typically in the range $14.47 < \log N(\text{Fe}^+) (\text{cm}^{-2}) < 15.30$, where the limits are the median values $\log N_{\text{DOP}}(\text{Fe}^+)$. If we again assume the largest blueshift, $V_{\text{Dop}} = -476 \text{ km s}^{-1}$, characterizes the deprojected outflow velocity, then $\dot{M} = 2 - 11 \text{ M}_\odot \text{ yr}^{-1}$ from Eqn. 12. For a Chabrier initial mass function, we estimate $\eta \approx 0.2 - 0.9$, and η would be 1.8 times lower for a Salpeter initial mass function.

Since previous mass-loss rates were derived from lower limits on gas column density (from saturated lines), these new results show, for the first time, that the mass fluxes in the low-ionization gas are not orders of magnitude higher than the typical SFR in these $z \sim 1$ galaxies. Future work should be able to combine our constraint from “down-the-barrel” observations, absorption detections towards background quasars and galaxies, and the extent of scattered resonance emission to improve the accuracy of the mass flux in the metal ions.

5.3. Outflow Scaling Relations

Empirical scaling relations for outflows help us to understand which physical processes shape outflows. For example, for local starbursts, the nearly linear increase in the blueshift of Na I absorption with increasing rotation velocity (Martin 2005) motivated outflow models in which radiation pressure accelerates the low-ionization gas (Murray et al. 2005). Momentum-driven outflows, in general, also predict an inverse scaling between the mass loading parameter and galaxy velocity dispersion, $\eta \equiv \dot{M}/\text{SFR} \propto \sigma^{-1}$ (Murray et al. 2005; Oppenheimer et al. 2010).

The evidence presented in this paper for collimated outflows complicates testing the momentum-drive wind conjecture. The measured Doppler shifts cannot be deprojected into the outflow velocities without knowledge of the galaxy inclination. At this time, the best we can do is to look for trends of the median Doppler shift with galaxy properties. We emphasize, however, that high-resolution images of the sample would allow us to improve our interpretation of the spectral measurements.

In contrast to studies of resolved galaxies at much lower redshifts, we have good statistical constraints on the halo masses of the galaxies in the LRIS sample. The halo masses are of interest because galaxy evolution models invoke feedback to suppress star formation in halos less massive than a *mass floor* at $\log M_h / \text{M}_\odot \lesssim 11$ (e.g., Bouché et al. 2010) and predict halo gas is mostly virialized (and therefore cold accretion and star formation suppressed) when $\log M_h / \text{M}_\odot \gtrsim 12$, the *mass ceiling*. The observed clustering (of star-forming DEEP2 at $z \sim 1$) galaxies with $M_B - 5 \log(h) < -20$, brighter than the faintest tertile of the LRIS sample, indicates a bias of

1.28 (Coil et al. 2008). If 15-20% of those galaxies are satellites, the minimum halo mass is $\log M_h / M_\odot \gtrsim 11.3$ (Zheng, Coil, & Zehavi 2007), and the mean halo mass is $\log M_h / M_\odot \approx 12.0$. Roughly one-third of the galaxies populate halos where gas accretion should occur primarily by hot-mode accretion. Our survey is sensitive to changes in outflow properties below the mass floor and above the mass ceiling.

5.3.1. Outflow Velocity vs. Stellar Mass

In their study of composite spectra, Weiner et al. (2009) found that the Doppler shift of the most blueshifted Mg II absorption increased with stellar mass to the power 0.17. They measured the Doppler shift $V_{10\%}$ at 90% of the continuum intensity, which corresponds closely to our V_{max} measurement for the median continuum S/N ratio of the LRIS spectra. The V_{max} (Mg II) values measured for the LRIS sample, however, do not increase with M_* , as illustrated in Figure 13. We found that V_{max} (Mg II) does increase with M_* when our analysis includes the K+A and green valley galaxies, which have high stellar masses and older stars (contributing broad, stellar Mg II absorption). One reason our results may differ is that our 400 l mm⁻¹ spectra do not resolve the absorption troughs at blueshifts less than 435 km s⁻¹, so we will overestimate the median velocity when a large fraction of spectra have blue wings just below that resolution limit. To test this idea, we identify the 600 l mm⁻¹ spectra by open squares and see that these V_{max} values become less blueshifted with increasing M_* in Figure 13. Furthermore, our measurements for the Fe II centroid velocity V_1 , which are not affected much by the resolution, do not vary strongly with stellar mass either in Figure 13. The centroid velocities systematically underestimate the outflow velocity in more massive galaxies because the interstellar absorption at V_{sys} is stronger; but when we estimated the velocity corrections with two-component fitting, the median blueshifts of the Doppler component did not reveal a significant trend with stellar mass. Spectral resolution is therefore not an obvious explanation for the discrepant result, yet it remains unclear whether stellar absorption significantly biases the Weiner et al. (2009) composite spectrum for high stellar mass.

5.3.2. Do Outflows Escape?

We follow Weiner et al. (2009) and use [OII] velocity dispersions, $\sigma_{[OII]}$ (Weiner et al. 2006), to estimate the depths of the gravitational potentials for galaxies in the LRIS sample.¹⁵ The relationship between the local escape velocity and $\sigma_{[OII]}$ is sensitive to the location of the absorbing gas along the sightline to each galaxy. For a spherical outflow geometry (of any solid angle), much of the column density of an outflow viewed down-the-barrel is necessarily contributed by the gas near the launch radius due to the inverse-square dilution of the gas density.

¹⁵ To the extent that the line-of-sight velocity dispersion measured from the linewidth reflects the gravitational potential, the 3D velocity dispersion will be approximately $\sqrt{3}$ times larger. Averaging over the variation in the relation between the line-of-sight velocity dispersion, $\sigma_{[OII]}$, and the rotation velocity at different disk inclinations (Rix et al. 1997; Kobulnicky & Gebhardt 2000; Weiner et al. 2006), Weiner et al. (2009) argue that $V_c \sim 1.67 - 2\sigma_{[OII]}$ with scatter of $\sim 25\%$.

The most conservative assumption is therefore that the gas lies a few pressure scaleheights above the disk at radius $R = 1$ kpc. For an isothermal halo of radius 100 kpc, the escape velocity at $R = 1$ kpc is $V_{esc} = 6.1\sigma_{[OII]}$. The median values of V_{esc} computed this way are 281, 406, and 643 km s⁻¹ for the low, middle, and high stellar mass tertiles; but the escape speeds are lower if the gas is further away. We detect absorption at velocities higher than these V_{esc} estimates, see bottom panel of Figure 13, and support the conclusion of Weiner et al. (2009) that outflowing gas detected in Mg II may not return to the galaxy.

The absence of observed growth in V_{max} with stellar mass implies that a higher fraction of outflowing gas is recycled in more massive galaxies. In light of the significant uncertainties inherent in interpreting V_{max} – including projection, sensitivity to S/N ratio, dependence on spectra resolution, and possible stellar contamination – the results presented here are probably not the final word on this scaling. In particular, we would not discount models that predict $V_{max} \propto V_{esc}$ (Murray et al. 2005; Zhang & Thompson 2010); their results are supported by observations of small samples of local starbursts observed at much higher resolution and S/N ratio (Martin 2005; Rupke et al. 2005).

Our comparison to the escape velocity also suggests that outflows generate some intervening, absorption-line systems. Bouché et al. (2006) found an anti-correlation between intervening absorber equivalent width and host halo mass and advocated an outflow origin for the intervening systems. A different treatment of the absorber clustering properties indicates the relationship could be due to the shocking of gas in very massive halos (Tinker & Chen 2008). In contrast, we find the largest Mg II equivalent widths in the more massive galaxies, attributed largely to emission filling but also partly to an increase in interstellar absorption (at the systemic velocity). Since our results indicate that outflows from $z \sim 1$ galaxies subtend a solid angle much less than 4π , the intervening absorption from outflows should show a dependence on location of the sightline relative to the projected outflow axis. Simple dynamical arguments show that the “blowout” will be perpendicular to the gaseous disk, so a distinguishing property of outflows is that they would be detected in sightlines passing near the minor axis of a galaxy. The recently discovered excess of Mg II absorption along minor axis of galaxies at these redshifts (Bordoloi et al. 2011; Bouché et al. 2012; Kacprzak et al. 2012) provides the best constraints to date on the extent of the winds. For example, Bordoloi et al. (2011) map Mg II absorption around a typical blue galaxy at $0.5 < z < 0.9$ using stacked spectra of background galaxies at projected distances $\lesssim 200$ kpc and find the Mg II equivalent width has fallen to $W \gtrsim 0.1 \text{ \AA}$ $b \approx 70$ kpc. We have measured Mg II absorption at blueshifts as high as 700 km s⁻¹; hence, these outflows would coast to 70 kpc in 100 Myr, a short enough time period for the host galaxy to remain blue even if the star formation rate were truncated. Together, these observations show that outflows do travel substantial distances.

5.3.3. Scaling with SFR, sSFR, and M_B

In Figure 13, the Fe II centroid velocities are shown against SFR, sSFR, absolute B -band magnitude, and

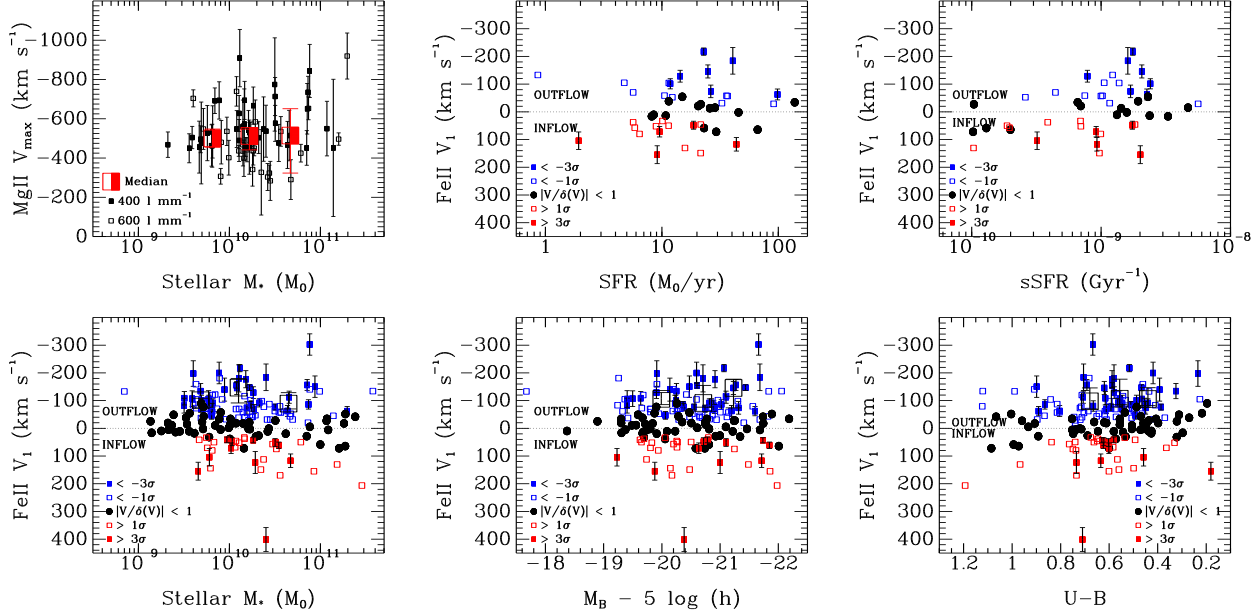


FIG. 13.— Range of Doppler shifts measured vs. galaxy properties. The outflow velocities projected along our sightline show no correlation with stellar mass, SFR, specific SFR, B -band luminosity, or $U - B$ color. *Top Left*: Maximum blueshift of Mg II $\lambda 2796$ absorption trough vs. stellar mass. Large symbols mark the median values and the $\pm 34\%$ range. *Bottom Left*: Doppler shift of Fe II absorption troughs vs. stellar mass. Large symbols denote the median values of the spectra with significant ($> 3\sigma$) blueshifts. *Top Center*: Doppler shift of Fe II absorption troughs vs. star formation rate. Large symbols denote the median values of the spectra with significant ($> 3\sigma$) blueshifts. *Bottom Center*: Doppler shift of Fe II absorption troughs vs. B -band luminosity. Large symbols denote the median values of the spectra with significant ($> 3\sigma$) blueshifts. *Top Right*: Doppler shift of Fe II absorption troughs vs. specific SFR. Large symbols denote the median values of the spectra with significant ($> 3\sigma$) blueshifts. *Bottom Right*: Doppler shift of Fe II absorption troughs vs. $U - B$ color. Large symbols denote the median values of the spectra with significant ($> 3\sigma$) blueshifts.

color. The median velocities of both the 3σ outflows and the 1σ outflows show no systematic trend with any of these galaxy properties. We examined similar plots using the velocities of the Doppler component and found no correlations with the Doppler component. In the SFR and sSFR plots, the errorbars on the median are quite large owing to the small number of galaxies in each bin. This large uncertainty combined with the relatively small range in SFR (~ 1 dex) could hide any underlying correlation between V_1 and SFR.

To increase the SFR baseline, we compare V_{max} measurements to nearby dwarf galaxies and extremely luminous starbursts in Fig. 14. First, we note that our median $V_{max}(\text{Mg II})$ measurements are consistent with the Weiner et al. (2009) measurements at slightly higher redshift. Second, when lower mass galaxies are included, the envelope describing the maximum outflow velocity increases with SFR. Excluding the galaxies with *dominant central objects*, or DCOs, because their high velocities may be related to AGN (Heckman et al. 2011), the slope is consistent with the $V \propto \text{SFR}^{0.35}$ relation measured previously for local starbursts (Martin 2005).

The true scatter in the $V_{max} - \text{SFR}$ scaling may be even larger than it appears in Fig. 14. Small Doppler shifts would go undetected unless the spectral resolution is very high, and echelle resolution has only been obtained for the nearby dwarf galaxies. Hence, the absence of data in the lower right corner of this plot is in part a selection effect. Moreover, projection effects only make the measured Doppler shifts lower than the outflow velocity, so the upper limit rather than the median is most interesting. The low-redshift galaxies shown in these plots are all starburst galaxies, and their SFR surface densities are typically higher than the outflow threshold (Heckman

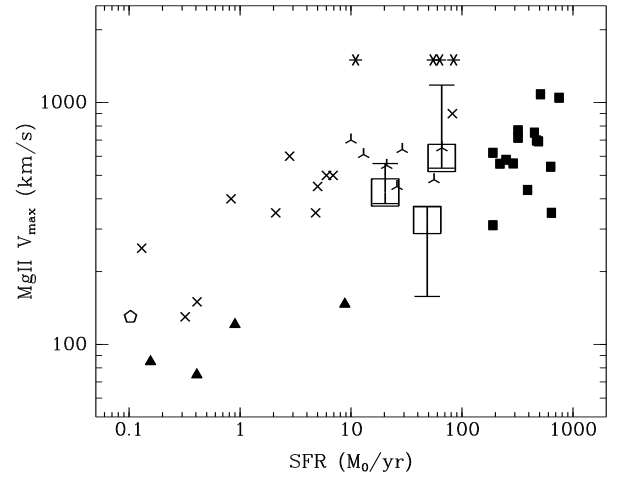


FIG. 14.— Maximum blueshift of low-ionization absorption vs. SFR. Large symbols show the median values among the LRIS galaxies and the Weiner et al. (2009) measurement of composite spectra. The legend denotes the sample and the lines used to measure the maximum blueshift of the absorption trough. Measurements for local galaxies from Schwartz & Martin 2004 (filled triangle), Martin 2005 (filled square), Grimes et al. 2009 (crosses), Heckman et al. 2011 (trefoil), and Chen et al. 2007; Vázquez et al. 2004 (NGC 1705 with SFR from Marlowe et al. 1997). Over many orders of magnitude in SFR, absorption tends to be found at higher velocities in galaxies with higher star formation rates even though this trend cannot be seen among the $z \sim 1$ Mg II results alone.

et al. 2003; Kornei et al. 2012). From this viewpoint, we argue that the absence of large Doppler shifts in dwarf galaxies – i.e., the paucity of points in the upper left of Figure 14 – is the most important feature of this scaling relation. Considering the multi-phase nature of winds,

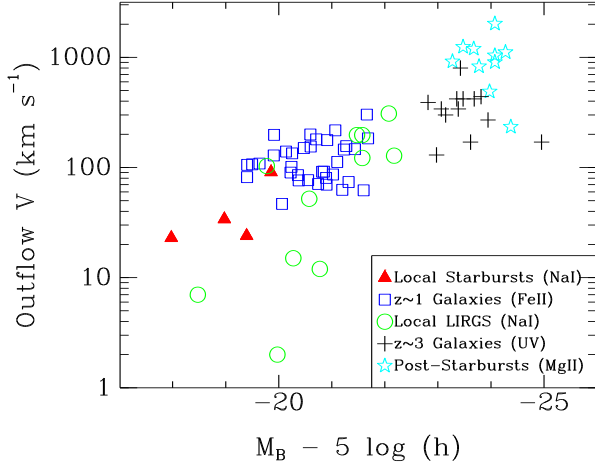


FIG. 15.— Outflow velocity of individual galaxies vs. absolute B -band magnitude. The legend identifies the samples and the transition(s) used to measure Doppler shift. The 3σ outflows in the LRIS sample have velocities intermediate to local starburst galaxies (Schwartz et al. 2004) and local luminous infrared galaxies (Heckman et al. 2000). Local post-starburst galaxies (Tremonti et al. 2007) and high-redshift galaxies (Pettini et al. 2001) show larger outflow velocities but also have significantly larger luminosities.

however, the apparent lack of high-velocity outflow in dwarf galaxies may be limited to warm, low-ionization gas. Based on Figure 4 of Hopkins et al. (2012), we suspect that most of the mass in a dwarf starburst outflow may be in the hot phase where the flow is moving at more than a few hundred km s^{-1} . If the highest velocity gas is in fact un-observable in low-ionization lines, then outflow velocity may not increase appreciably with SFR as argued, for example, based on the measured temperatures of the X-ray emitting gas (Martin 1999).

Figure 15 compares our $V_1(\text{Fe II})$ measurements for the outflow sample to other populations with starburst-driven outflows. Each of these samples includes spectra in which the resonance absorption lines show no significant blueshift relative to the galaxy, but we plot only the outflow galaxies. Since the different surveys have different criterion for the minimum detectable Doppler shift, the absence of points in the lower right corner is not significant; but the maximum outflow speeds of each population likely represent the “down-the-barrel” view of their outflows. Taken together, these measurements show outflow speed increases with B -band luminosity. Since B -band luminosity is correlated with SFR, this result provides evidence for higher outflow velocities in galaxies with higher SFRs.

6. GAS INFLOWS

In Section 1 we discussed gas inflows in the context of a popular model whereby the gas accretion rate regulates the galactic SFR (Dekel & Birnboim 2006; Kereš et al. 2009a; Kereš et al. 2009b; Bouché et al. 2010; Davé, Finlator, & Oppenheimer 2012). Testing this theory requires observations of the gas inflows that reach galactic disks. Cosmological simulations agree that the infalling gas which fuels star formation is *cold*, in the sense that its temperature never exceeded $10^{5.5}$ K, and that these cold flows gradually disappear at halo masses exceeding $10^{12} M_\odot$ due to the formation of virial shocks which increase the gas cooling time (Kereš et al. 2005; Dekel &

Birnboim 2006; Ocvirk, Pichon, & Teyssier 2008; Kereš et al. 2009; Brooks et al. 2009; van de Voort et al. 2011a). The densest gas in these cold flows has a low covering factor but threads filaments of lower density gas with cross-sections much larger than a galaxy (Kimm et al. 2010; Faucher-Giguère et al. 2011; Fumagalli et al. 2011). These inflowing streams carry significant angular momentum that cause them to co-rotate with the galaxy and form a warped, extended disk; hence cold flows may be recognized kinematically by a velocity offset in the same direction as the rotation of the central disk (Stewart et al. 2011a, 2011b).

In contrast to the accretion rate onto *halos*, which is robustly predicted, the rate of gas accretion onto *galaxies* depends sensitively on feedback processes (van de Voort et al. 2011b). Winds transport supernova ejecta into the circumgalactic medium (Martin, Kobulnicky, & Heckman 2001), so these metals mark gas that was once in a galaxy. The mixing between these metals and cold flows is challenging to resolve in numerical simulations, so the metallicity of accreting gas near galaxies remains quite uncertain. At least in some models, however, recycling of the metals carried to large distances by winds substantially increases the metallicity of the infalling gas (Oppenheimer et al. 2008; Davé et al. 2011b). In other simulations, in contrast, the cold flows are not even detectable in metal lines owing to their low metallicity (Kimm et al. 2011; Fumagalli et al. 2011; Goerdt et al. 2011).

The obvious difference between galactic outflows and inflows is the kinematics of the absorption-lines they imprint on galaxy spectra. Blueshifted (redshifted) lines in galaxy spectra necessarily mark outflowing (inflowing) gas because the absorbing material must lie on the near side of the galaxy. Near-UV spectra are equally sensitive to redshifted and blueshifted Fe II absorption. Because blueshifts turn out to be more common, composite spectra miss the redshifted absorption, and spectra of individual galaxies turn out to be critical for identifying inflows (Sato et al. 2009; Rubin et al. 2012). Inflow detections apparently require surveys of roughly a hundred or more galaxies. Both the measurements presented here (9 spectra out of 208) and recent work by Rubin et al. (2012) identify inflowing metals towards a few percent of $z \sim 1$ galaxies.

These infalling streams may not arise from cold flows; the metals may mark gas recycled through galactic winds, tidally stripped gas, and/or material condensing out of hot halo gas. To provide some basis for distinguishing among these processes, in Section 6.2 and Section 6.3 we individually examine the spectra of 3σ inflow galaxies and estimate physical properties of the inflowing gas. In particular, we find evidence that the inflowing gas detected in front of the galaxies marks an inflowing stream which subtends a larger solid angle than the galaxy on the sky. We then return to the discussion of the source of the inflow in Section 6.4 focusing primarily on the cold inflow model due to recent interest in, and theoretical predictions for, this particular scenario.

6.1. Inflow Confirmation

We identify a net inflow of low-ionization gas by a statistically significant redshift of the Fe II absorption troughs, $V_1(\text{Fe II}) \geq 3\sigma(V_1)$. The uncertainty in this fitted centroid velocity does not take errors in the galaxy

redshift determination into account. We reviewed the redshift determination and other sources of systematic error individually for the 11 galaxies with 3σ inflows and identified possible systematic errors in two of the three cases described here.

All but one (22028473) of the inflow galaxies have strong emission lines in our LRIS spectrum; and, as described in Section 2.2, we measure the centroids of the emission lines to within $\pm 19 \text{ km s}^{-1}$. Among these inflow galaxies, the average difference between this LRIS redshift and the DEIMOS redshift from DEEP2 is 45 km s^{-1} with neither survey yielding systematically higher (or lower) redshifts. The magnitude of this discrepancy is consistent with the internal error of 41 km s^{-1} reported by DEEP2 from multiple observations of galaxies and presumably arises from velocity gradients across galaxies. For the inflow galaxy 22028473, however, the galaxy redshift comes from the [O II] emission in the DEEP2 DEIMOS spectrum because our LRIS spectrum does not cover optical, nebular lines. The fitted Doppler shift of the Fe II absorption, $41 \pm 10 \text{ km s}^{-1}$ in Table 6, is comparable in magnitude to the systematic error in the redshift determination. Although correcting this error is equally likely to (a) double the inflow speed or (b) negate the inflow detection, we drop this object from the inflow sample because it is not a significant ($> 3\sigma$) detection when the error in the galaxy redshift is considered.

Our adopted LRIS redshift for 22005270 exhibits one of the largest discrepancies from the DEEP2 redshift, 69 km s^{-1} . The velocity gradient between apertures 2 and 4 exceeds this discrepancy, so systematic differences in slit placement may well be the cause. The $H\beta$ emission line in our spectrum of 22005270 appears very slightly redshifted, but we attribute this shift to residuals from a sky line 93 km s^{-1} redward of $H\beta$. We keep this object in the inflow sample. The LRIS redshift accurately determines the systemic velocity for the purposes of comparing the velocities of the galaxy and the resonance absorption. Even if we adopted the extremely conservative viewpoint that the redshift uncertainty was 60 km s^{-1} , the projected infall velocity of $401 \pm 43 \text{ km s}^{-1}$ still yields a 3σ inflow detection.

We do remove 22036194 from the inflow sample because of the systematic error introduced in our Fe II series fit by intervening absorption. Our 22036194 spectrum was recorded at a position angle of 25° , so the slit passes near the $z = 0.913$ galaxy 22035919 at an angular separation of $7''.1$. Intervening Mg II absorption from a foreground galaxy near this redshift appears slightly redward of the interstellar Fe II $\lambda 2344$ absorption trough in our 22036194 spectrum. The net, blended absorption trough is stronger and redder than the other lines in the Fe II series and therefore systematically biased the fit. Rejection of the Fe II $\lambda 2344$ transition yields a fitted Fe II absorption velocity consistent with the interstellar gas in 22036194. We note, however, that 22035919 is unlikely the source of the intervening absorption due to the strength of the line and the $\gtrsim 50 \text{ kpc}$ impact parameter. We detect prominent emission lines (near $z \sim 0.831$), in fact, from another galaxy closer to the 22036194 sightline in our 2D spectrum and suggest this object is the source of the intervening Mg II absorption.

With 22028473 and 22036194 rejected, the 3σ inflow

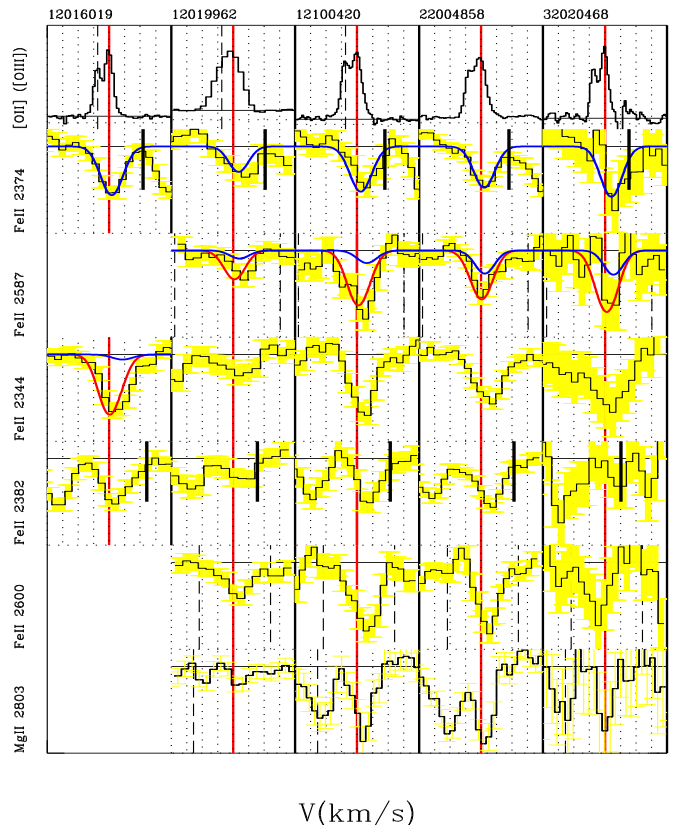


FIG. 16.— Resonance absorption lines (bottom 6 rows) redshifted with respect to nebular emission lines (top row) define inflow galaxies; see also Fig. 17. The single-component fit to the Fe II series is superposed on the Fe II $\lambda 2374$ profile; and the two-component fit to the Fe II series is plotted on the Fe II 2587 profile. A bold vertical bar marks the maximum velocity of absorption measured in the Fe II $\lambda 2383$ and Mg II 2803 troughs. The tick marks on the velocity scale are separated by 300 km s^{-1} . The solid (red) vertical line marks the systemic velocity, and dashed vertical lines denote the wavelengths of other transitions. (Note that there is an airglow line at -735 km s^{-1} blueward of the Mg II $\lambda 2796$ line in 12019996 that affects the blue wing of $\lambda 2796$ blueward of -359 km s^{-1} .) The low-ionization absorption is clearly redshifted with respect to the nebular emission in the same spectrum, although the significance of the inflow in 22028473 is marginal (see text for details).

sample contains 9 galaxies. Figures 16 and 17 illustrate the 3σ redshifts of the Fe II absorption troughs relative to the nebular emission. The joint fits to the Fe II series find a significant redshift because the absorption troughs of multiple transitions show a net redshift. The redshifted absorption does not appear to be unique to the Fe II lines; the Mg II 2803 absorption trough (row 7 of these figures) often has a net redshift as well. Table 6 provides the measured properties of the redshifted absorption troughs. Table 4 summarizes the quality of the individual spectra and galaxy redshift, B -band luminosity, color, stellar mass, and (when available) SFR.

6.2. Spatial Extent of Infalling Gas

We can, given adequately strong emission or absorption lines, measure velocity gradients along each slitlet. For illustration, we selected the four galaxies with large velocity gradients along the slit. Figure 18 shows the positions of these slitlets on images, the two-dimensional blue spectra around Fe II $\lambda 2600$, and the two-dimensional red spectra near nebular emission lines. The [O II]

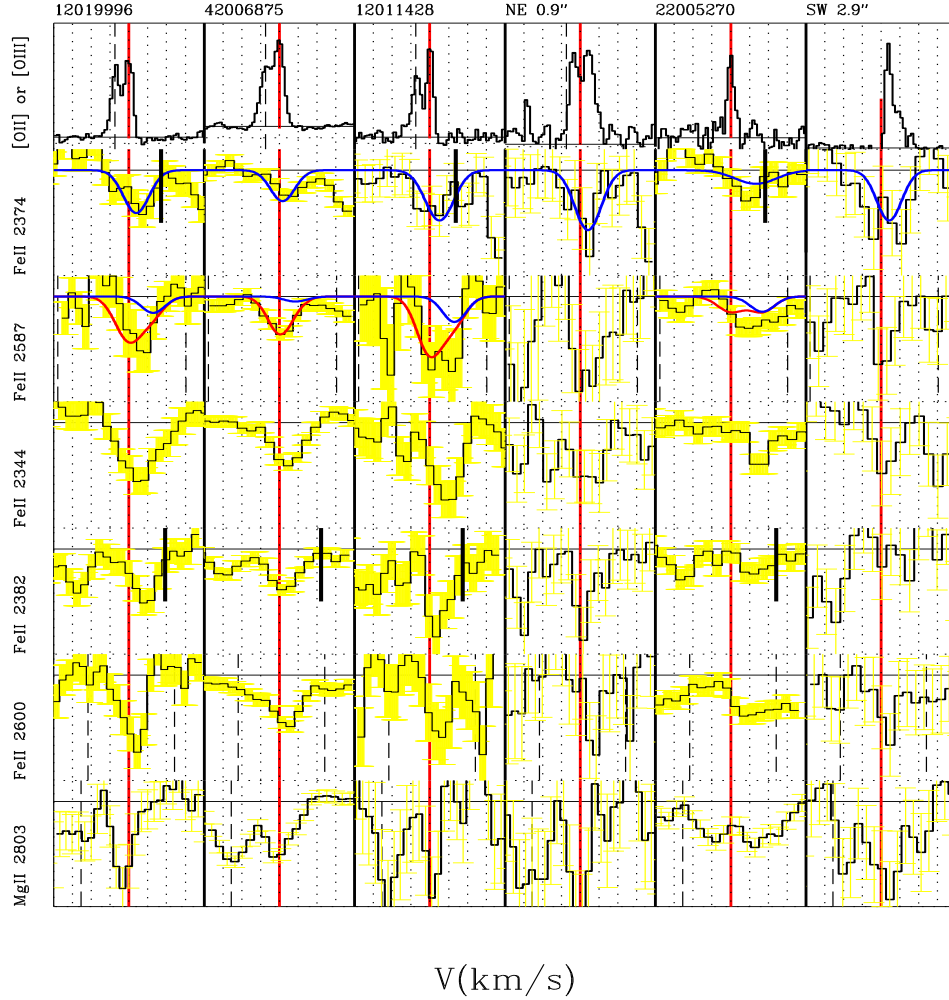


FIG. 17.— Same as Fig. 16 but for the other four inflow galaxies. Spectra extracted $0''.85$ northeast of 12011428 and $2''.94$ SW of 22005270, also shown, have Fe II Doppler shifts of 123 ± 47 and 129 ± 62 km s^{-1} , respectively, and nebular emission that is Doppler shifted with respect to the center of each galaxy. Remarkably, the velocity of this off-center emission is similar to the infall velocity of the low-ionization gas detected in Fe II absorption.

emission lines are clearly tilted along the slits crossing 12011428, 12019996, and 42006875 as is the [O III] $\lambda 5007$ emission along the 22005270 slit. We obtain additional insight about the inflows by investigating whether the emission or absorption anywhere along the slit is at the same velocity as the redshifted Fe II absorption discovered in the galaxy spectra (i.e., extracted from apertures centered on the galaxy). We now consider the two-dimensional spectra of each of these galaxies in further detail.

12011428:— Along the slit that crosses 12011428, the line emission is not continuous. To the north of 12011428, a second blob of [O II] emission is detected $1''.14$ (9.6 kpc) away along the slit. The image shows a hint of faint, extended R -band emission in this direction. An [OII] emission-line spectrum extracted at this location exhibits a redshift of 125 ± 15 km s^{-1} . The emission redshift on this side of the galaxy is remarkable because resonance absorption is seen at a similar velocity, 154 ± 32 km s^{-1} , in the galaxy spectrum (extracted from an aperture centered on the galaxy continuum). This coincidence in velocity space may indicate that the infalling stream crossing the center of the galaxy reaches the galaxy near the

star-forming knot 9.6 kpc away. Further evidence supporting a structural connection between the redshifted emission and absorption is found in the grism (blue) spectrum extracted on the northern side of the galaxy (aperture marked in green in Figure 18). The Fe II resonance absorption remains redshifted in the off-center spectrum, and we find no spatial gradient in the absorption velocity across the 12011428 slit. The infalling gas apparently covers 12011428, and one side of the galactic disk shares the redshift of this infalling stream.

22005270:— Along the slit that crosses 22005270, the line emission is not continuous in the two-dimensional spectrum shown in Figure 18. Roughly $3''.5$ southwest of 22005270, where the slit passes near galaxy 22005066, we detect a spatially extended blob of [O III] emission ($1''.6$ or 12.2 kpc across). Further along this slit, we extracted another spectrum $4''.3$ (33 kpc) southwest of 22005270 because the [O III] emission-line profile is double-peaked; the stronger, longer wavelength maximum at 346 km s^{-1} and a weaker component at -158 km s^{-1} . The large emission redshift near 22005066 is remarkable because Fe II resonance absorption is seen at a similar velocity in the spectrum of 22005270. In

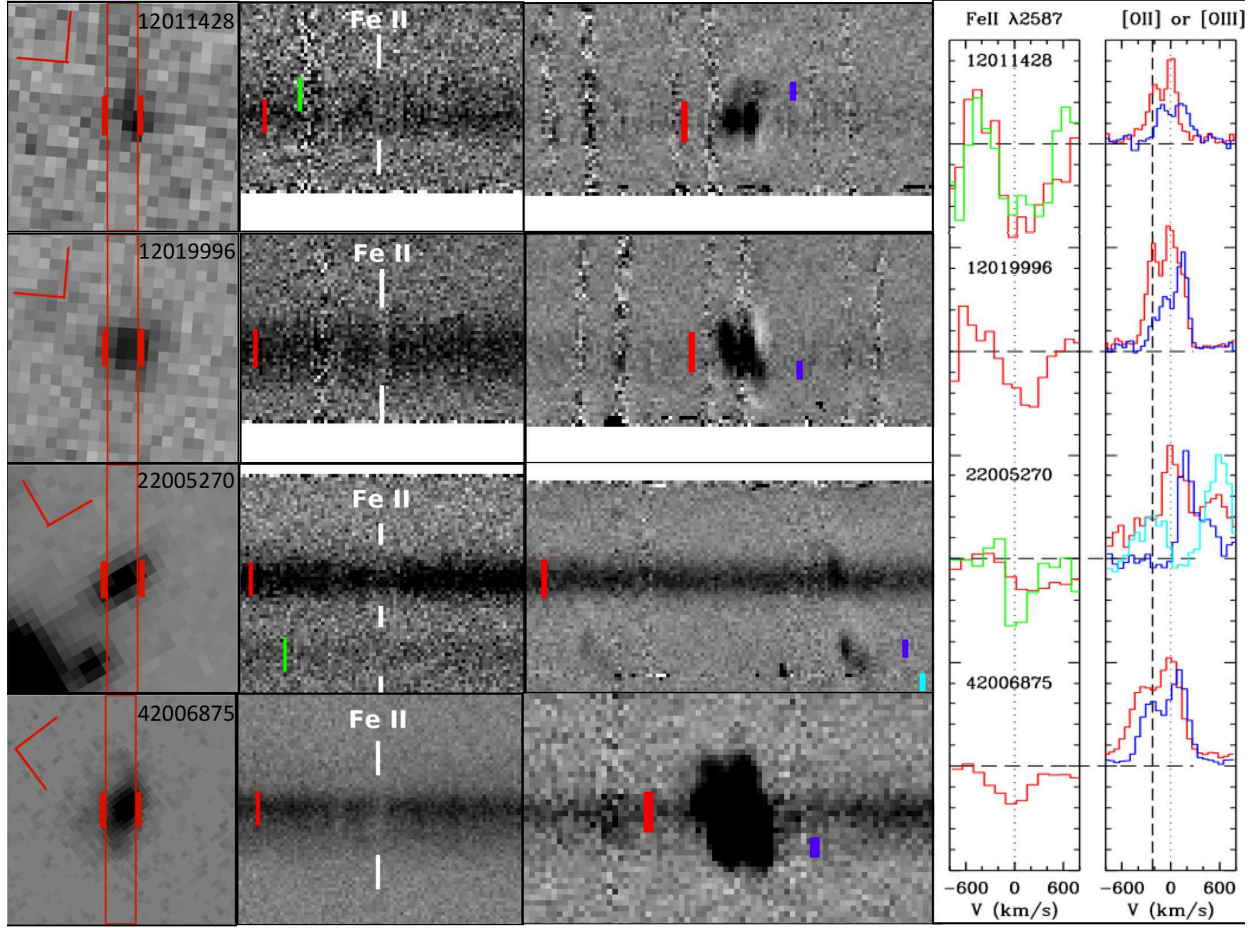


FIG. 18.— Velocity gradients in the two-dimensional LRIS spectra of inflow galaxies. *First Column:* DEEP2 (CFHT, *R*-band) image with the $1''.2$ by $9''.0$ slitlet and central extraction aperture marked. The compass rose marks north and (to the left of that) east. The slit across 22005270 passes near a galaxy identified as 22005066 in the DEEP2 photometric catalog. *Second Column:* Two-dimensional LRIS spectra near Fe II $\lambda 2600$ (marked with red arrow). Wavelength increases from left to right, and the width of the region shown is approximately 183\AA (83 pixels). We denote the central apertures and the apertures used for the off-center spectra shown in *Column 4* and Figure 17. *Third Column:* Two-dimensional LRIS spectra near the [O II] $\lambda\lambda 3726, 3729$ doublet (or, in the case of 22005270, near [O III] $\lambda 5007$). Wavelength increases from left to right, and the width of the region shown is approximately 81\AA . We mark the central apertures and the off-center apertures where we extracted the emission-line profiles shown in *Column 5*. The tilt of the emission lines reflects the rotation of dense gas in these galaxies and, in 22005270, the relative motion of a satellite galaxy. In all 4 spectra, the gradient in the emission velocity along the slit is as large as the redshift of the Fe II absorption measured ‘down-the-barrel’ in the centered aperture. The infalling gas seen towards the centers of these galaxies is apparently part of more extended structure kinematically related to the outer disks and satellites.

fact, the spectrum of 22005270 shows the largest Fe II redshift at $401 \pm 43 \text{ km s}^{-1}$. Within the uncertainties, this absorption velocity is marginally consistent with the emission component at $346 \pm 19 \text{ km s}^{-1}$. Further evidence for a connection between the redshifted [O III] emission near 22005066 and the redshifted absorption in the 22005270 spectrum is apparent upon re-inspection of the primary spectrum towards 22005270. In both Figure 17 and Figure 18, the bright [O III] emission in the 22005270 spectrum falls at zero velocity by definition, but a weak redshifted emission component is detected at 341 km s^{-1} , a redshift similar to the centroid velocity of the Fe II absorption. We show the extracted blue spectrum where the slit passes near 22005066 in Figure 17. The continuum S/N ratio in this spectrum is low relative to the blue spectrum of 22005270; but we see a net

redshift of the Fe II and Mg II absorption. These coincidences in velocity space indicate that the infalling gas seen in absorption towards 22005270 is part of a physical structure covering both 22005270 and 22005066 and therefore at least 33 kpc across.

12019996:— The tilt of the [O II] emission in the 12019996 spectrogram shows the usual signature of a rotating disk. The emission extends $0''.68$ (5.6 kpc) to the south where the Doppler shift reaches $102 \pm 10 \text{ km s}^{-1}$. The velocity gradient between the central aperture and the receding side is nearly as large as the $117 \pm 25 \text{ km s}^{-1}$ redshift of the Fe II absorption in the central aperture. Separate blue spectra were extracted for the two spatial halves of 12019996, and the absorption found to be at the same wavelength (Doppler shift) in both. Apparently the infalling gas marked by the red-

shifted resonance absorption extends all the way across the 12019996 disk. The lack of rotation suggests the infalling material lies significantly in front of the galaxy, as gas close to the galaxy would likely rotate with the disk.

42006875:— In the 42006875 spectrum, the tilt of the [O II] emission shows the usual signature of a rotating disk. Across the 42006875 slit, the relative redshift of the emission reaches 68 km s^{-1} $1''.4$ (10 kpc) to the northwest of the center of the galaxy. The velocity gradient between the center of the galaxy and the receding side is as large as the $51 \pm 14 \text{ km s}^{-1}$ redshift of the Fe II absorption in the galaxy spectrum. In 42006875, the Mg II absorption trough is near systemic velocity but the 2803 line has a red wing. The two-dimensional spectrum shows evidence that the infalling gas is part of a spatially extended structure, and that this structure may meet the disk roughly 10 kpc southeast of the galactic center.

To summarize, the LRIS spectra cover nebular emission lines in all 9 inflow galaxies. We have described the discovery of line emission near the redshift of the Fe II resonance absorption in 4 of these: 12011428, 12019996, 22005270, and 42006875. How do the emission-line kinematics compare to the redshift of the Fe II absorption in the galaxy spectrum in the other 5 spectra? The two-dimensional spectra of 32020468 and 12100420 do not resolve the line emission spatially. The absence of spatially extended emission is not surprising in light of their compact morphology in ground-based images, and 12100420 also looks compact in an HST image. Yet, as illustrated in the spectra shown in Figure 16, the Fe II absorption is redshifted $123 \pm 40 \text{ km s}^{-1}$ in 32020468 and 71 ± 18 in 12100420. In 12100420, the Mg II absorption also displays a net redshift; but in 32020468, the Mg II absorption is detected a low significance near the systemic velocity. In the remaining 3 galaxies – 12016019, 12019962, and 22004858 – the [O II] emission along the slitlets is spatially resolved and very slightly tilted. Despite the small gradient in the velocity of the emission, however, the spectra of these galaxies exhibit significantly redshifted resonance absorption. The Mg II absorption trough also exhibits a net redshift in 22004858. Hence, none of these 5 spectra show line emission at redshifts near the Fe II absorption redshift. It would be valuable to obtain spectra at other position angles and determine whether or not these galaxies have any extended emission at the redshift of the Fe II absorption as in the case of the four objects in Figure 18.

6.3. Properties of Infalling Gas

6.3.1. Which Galaxies Have Infalling Metals?

Nine of the 208 spectra show very significant (3σ) redshifts of the Fe II absorption relative to the host galaxy. The low fraction of unambiguous inflows appears to be consistent with the 6 inflows identified recently by Rubin et al. (2012) among ≈ 100 objects. Here, we examine the properties of these 9 galaxies and their enriched infall. We cannot exclude a higher inflow fraction at lower velocities and less significant equivalent widths; however, the results presented for inflows in Figure 9 indicate not more than 20% of the spectra show inflows with Doppler shifts larger than the systematic error of 41 km s^{-1} in the determination of the systemic velocity.

In the SFR – stellar mass plane shown in Figure 11, the masses of 4 of these 5 inflow galaxies fall in the high mass tertile. Given the small number of objects, however, this excess is hardly significant and not supported by the full sample in which 4 of the 9 inflow galaxies have stellar masses less than $\log M / M_{\odot} = 10.20$, the median stellar mass of the LRIS sample. We have only measured the SFRs for 5 of the galaxies with Fe II redshifts (that lie in the AEGIS field). Three (two) of these 5 galaxies have specific SFRs lower (higher) than the average shown in Figure 11, hence inflows do not depend strongly on specific SFR. We found 3/69, 2/68, and 4/71 galaxies with redshifted Fe II absorption, respectively, in the low, middle, and high redshift tertiles of the LRIS sample. In spite of the limited sample size, we therefore conclude that inflow galaxies may sample the full range of SFR, specific SFR, stellar mass, and redshift.

The galaxies with spectra showing redshifted Fe II absorption do not have unusual properties in any way, aside from having infalling gas along the sightline to them. Since the galaxies with detected inflows do not share some physical property, we argue that most galaxies may have inflows and attribute the low incidence of measured redshifts to the geometry of the infalling streams. Specifically, we find 3-6% sightlines towards $z \sim 1$ galaxies show redshifted Fe II, so the covering fraction of the inflows is quite small.

6.3.2. Velocity

In Table 6, we summarize the inflow speeds fitted to centroids of the Fe II absorption troughs. Except for the extreme case of 22005270, the fitted 1-component velocities are less than 200 km s^{-1} and therefore consistent with Rubin et al. (2012). The gas moves at speeds of material bound to galaxies. Evidence for high velocity gas can be seen in the absorption-line profiles shown in Figures 16, 17, and 18. The largest inflow velocity is detected via the Mg II absorption trough in 22005270. In the red wings of the Fe II line profiles, absorption at velocities exceeding 600 km s^{-1} is detected in 12016019, 12019962, 12100420, 22004858, 22005270, and 42006875. Modeling the contribution of the ISM via two-component fitting increases the estimated inflow velocity. The median inflow velocity increases from 71 km s^{-1} in the single-component fits to 191 km s^{-1} in the two-component fits.

6.3.3. Inclination

Rubin et al. (2012) found that 5 of their 6 inflow galaxies have highly inclined ($i > 55^\circ$), disk-like morphologies. They interpreted the high inclinations as evidence that rotation dominates the kinematics of the infalling gas but pointed out a paradox – i.e., that the absorbing gas must be located on only the receding side of these galaxies. Our observation of the large spatial extent of infalling gas solves this problem because it suggests a scenario where an inflowing stream crosses in front of the galaxy before meeting up with the extended disk.

Kornei et al. (2012) show the morphologies of five of the LRIS inflow galaxies. The axis ratio was not well measured for 12011428. The measurements for 12100420, 12019962, and 12019996 indicate $i < 55^\circ$ however, and only 12016019 is consistent with a large inclination of

$\sim 61^\circ$. Hence, it remains unclear whether high inclination is a necessary condition for the detection of enriched infall.

6.3.4. Infalling Mass

The (median) equivalent widths of the Fe II $\lambda 2374$ and 2261 lines suggest the total Fe II column density, ISM plus inflow, typically lies in the range $15.08 \leq \log N(\text{Fe}^+)(\text{cm}^{-2}) \leq 15.85$. For purposes of illustration, we conservatively choose solar metallicity gas, no depletion of Fe onto grains, and an ionization fraction of 100% singly ionized iron. The total hydrogen column density is then

$$\log N(H)(\text{cm}^{-2}) \approx 19.58 + (\log N(\text{Fe}^+) - 15.08) - \log(Z/Z_\odot). \quad (13)$$

The implied column is $\log N(H) = 19.58$ for solar metallicity infall, but lower metallicities are plausible and raise the inferred hydrogen column.

The galactic ISM clearly produces some of the Fe II equivalent width since our sightline directly intersects a galaxy. Although a true measurement of the inflowing column in ionized iron requires much higher spectral resolution, the potential impact of the ISM on the equivalent width of the inflowing component can be illustrated with two-component fits to the absorption trough as outlined in Section 3.3.2. For the Doppler component fitted to the Fe II absorption, we integrated the equivalent widths of the $\lambda 2374$ and $\lambda 2261$ profiles to obtain the lower and upper bounds, respectively, on $N_{\text{Dop}}(\text{Fe}^+)$ in Table 6. The median bounds provide a very rough estimate of typical inflow column $14.4 \leq \log N_{\text{Dop}}(\text{Fe}^+)(\text{cm}^{-2}) \leq 15.15$. The total hydrogen column of the inflowing column is therefore typically larger than

$$\log N(H)(\text{cm}^{-2}) \approx 18.90 + (\log N(\text{Fe}^+) - 14.40) - \log(Z/Z_\odot). \quad (14)$$

Gas columns larger than those associated with galactic disks and damped Lyman- α systems, $\log N_H(\text{cm}^{-2}) \approx 20.3$, seem unlikely. Hence, we expect the metallicity of the redshifted gas is greater than roughly $0.04 Z_\odot$.

6.4. Comparison of Inflow Properties to Models

Many properties of the infalling gas are consistent with the cold flow scenario. The velocity components along our sightlines are largely consistent with virial motion, the exception being the extremely large redshift towards 22005270 which is associated with the satellite galaxy 22005066. The two-dimensional spectra provide spatial information about the inflow in 3 other objects, and in those the redshift of the infalling gas matches the projected velocity on one side of a rotating, gas disk. This association could reflect a stream crossing in front of each galaxy and connecting to the outer disk in the manner predicted by Stewart et al. (2011a, b). The low incidence of redshifted Fe II absorption in spectra of $z \sim 1$ galaxies would also be expected for cold flows.

To have any chance of detecting a cold flow in a metal line, the sightline must run along the filament (e.g., see Figure 2 in Kimm et al. 2010), and the chance of such a favorable orientation is small. While differences in the radiative transfer calculations produce some variation in

the average covering fraction among these models, galaxies with covering fractions of more than a few percent, as originally suggested by Dekel et al. 2009a, are now thought to be quite rare (Kimm et al. 2009). Numerical simulations suggest that only a few percent of the sightlines passing within 100 kpc of a massive galaxy at $z \sim 2$ intersect dense ($\log N_H(\text{cm}^{-2}) > 20.3$), inflowing gas (Kimm et al. 2010; Faucher-Giguère et al. 2011; Fumagalli et al. 2011). It must be acknowledged, however, that these high columns represent the cool gas threading the filaments rather than the smooth component of the cold streams, which dominates the cross section of neutral hydrogen absorption below $\log N_{HI}(\text{cm}^{-2}) = 18$ within R_{vir} (Fumagalli et al. 2011). At $z < 2$, less than half the cross section in the range $19 < \log N_{HI}(\text{cm}^{-2}) < 20$, and less at higher columns, is likely due to streams (Fumagalli et al. 2011).

Theory predicts the disappearance of cold flows in halos more massive than roughly $10^{12} M_\odot$. The halo masses of many of the galaxies in the high stellar mass tertile of the LRIS sample are likely above $10^{12} M_\odot$ based on either their clustering properties (Coil et al. 2008) or halo abundance matching (Behroozi, Conroy, and Wechsler 2010). In the LRIS sample, we did not find any change in the inflow fraction with increasing stellar mass; however, this sample excludes red sequence galaxies. As can be seen by comparing the density of red sequence and blue cloud galaxies in Figure 1, the fraction of red galaxies increases quite quickly among galaxies with stellar masses $\log M/M_\odot > 10.3$, the typical stellar mass in a $10^{12} M_\odot$ halo at $z \sim 1$ indicated by abundance matching (Behroozi et al. 2010). Whether or not the fraction of inflow galaxies declines with mass in an unbiased sample cannot be determined from our data since we do not measure the inflow fraction towards red galaxies. Likewise, the lack of any evolution with redshift might be limited to blue cloud galaxies which compose the LRIS sample.

According to some models (Kimm et al. 2011; Fumagalli et al. 2011), detection of the inflows via a metal line definitely implies these are not cold accretion flows. From our perspective, however, the metallicity of the cold inflows near galaxies remains a highly uncertain quantity in the models due to the unrealistic treatment of metal recycling via galactic winds. The circulation of metals might significantly enrich the cold flows before the infalling gas is incorporated into the galactic disk.

In this recycling scenario, the distinction between cold flows and infalling relic outflows may become blurred. Numerical simulations including outflows have suggested that the covering factor of high column density (DLA-like) gas increases with halo mass, due in large part to the kinematics of outflowing gas (Hong et al. 2010; Faucher-Giguère et al. 2011). Given the lack of a strong scaling relation between outflow velocity and stellar mass, we expect a larger fraction of the outflowing material to fall back onto the more massive galaxies. Hence, the recycling of outflows should produce an increasing inflow column as stellar mass increases.

The distinction between the increasing (decreasing) inflow column with stellar mass due to wind recycling (cold flows) may provide a means to discriminate the primary origin of infalling metal-enriched gas. This proposal further emphasizes that inflow fraction measure-

ments should include red sequence galaxies. Although we expect only star-forming galaxies to drive outflows, the galaxies may migrate across the color - magnitude diagram (due to the cessation of star formation) before the bulk of the outflow slows down and turns around (due to the gravitational attraction of the galaxy). The first inflow galaxies identified appeared to support this scenario; their optical colors placed them on the red sequence, but their UV-optical colors indicated they were forming stars a few 100 Myr prior (Sato et al. 2009). A subsequent study of 13 K+A galaxies, however, discovered 2 inflow galaxies (Coil et al. 2011) suggesting an inflow fraction similar to our result for blue cloud galaxies.¹⁶ Finally, mergers also bring gas into galaxies. The association of the galaxy 22005066 with the redshifted Fe II absorption in 22005270 may reflect this scenario. Because 22005066 is the less luminous of the two galaxies, we would expect a tidal stream to pull gas out of 22005066 onto 22005270.

In summary, cold flows, mergers, and wind recycling are all expected to contribute to gas infall. The low incidence of infall suggests that whichever process dominates, the covering fraction of the infalling streams is low. Much larger samples of individual spectra will be needed to further distinguish among these mechanisms on a statistical basis.

7. SUMMARY & IMPLICATIONS

Our understanding of galaxies will be greatly improved once we understood what controls the flow of matter between galaxies and the circumgalactic medium. Empirical constraints are essential in this regard because there are many physical processes that may be important and these processes can be nonlinear – e.g., the cooling rate or the interplay between mechanical and radiative feedback.

In this paper, we used unusually deep spectroscopy of galaxies at $0.4 < z < 1.4$ to investigate which galaxies have low-ionization outflows. The blue sensitivity of LRIS and collecting power of the Keck I telescope made it possible to detect NUV absorption lines in spectra of individual galaxies. These galaxies are typical blue cloud galaxies and have higher SFRs than do most galaxies today. We have fit a series of Fe II absorption lines to describe the bulk flow (to within $\pm 40 \text{ km s}^{-1}$) and constrain the Fe II column density (to within an order of magnitude). These Doppler shifts have been compared to the most sensitive tracer of high-velocity gas in the spectra, the Mg II $\lambda\lambda 2796, 2803$ doublet, which is frequently detected out to impact parameters of 70 kpc in galaxy halos.

Among spectra of star-forming, blue-cloud galaxies, we measure Fe II blueshifts of at least $-50, -100$, and -200 km s^{-1} , respectively, in 45%, 20%, and 2.5% of them. We show that this outflow fraction is roughly 3 times higher in galaxies with $21 < \text{SFR} (msunyr) < 98$ than in galaxies with $0.9 < \text{SFR} (M_{\odot} \text{ yr}^{-1}) < 10$. Additional evidence of larger blueshifts in star-forming galaxies is demonstrated by comparing the average spectra of the sample divided at the median SFR. We detect the

most significant outflows in spectra of individual galaxies with specific SFR larger than 0.8 Gyr^{-1} ; and galaxies with $-8.80 < \log \text{sSFR} (\text{ yr}^{-1}) < -8.25$ are up to 5 times more likely to show blueshifted Fe II absorption than those with $-10.18 < \log \text{sSFR} (\text{ yr}^{-1}) < -9.16$. This trend implies a slow increase in outflow fraction with increasing redshift. Since the outflow fraction varies most significantly with specific SFR, our results confirm the expectation that the blueshifts of the Fe II lines identify outflows powered by massive stars.

We have also examined how stellar mass and related galaxy properties affect the outflow fraction. We find no variation of Fe II Doppler shift with stellar mass, blue luminosity, or $U - B$ color. The Mg II equivalent width increases towards higher stellar mass, B -band luminosity, and redder color in both composite and individual spectra. The presence of Mg II emission in the lowest mass, least luminous, and bluest galaxies, coupled with unphysical equivalent width ratios between transitions of the same ion, strongly suggest that resonance emission partially fills the intrinsic absorption troughs. The higher dust and interstellar gas content in more massive galaxies may reduce the amount of scattered emission that escapes; evidence favoring this interpretation includes the larger reddening and stronger (interstellar) absorption at the systemic velocity in more massive galaxies. In summary, we find no compelling evidence for a change in outflow properties among blue cloud galaxies over a substantial range in stellar mass, which spans the halo mass floor and mass ceiling required by equilibrium SFR models. At stellar masses greater than $\log M_{*}/M_{\odot} \gtrsim 10.3$, these blue cloud galaxies do of course become an increasingly smaller fraction of the entire stellar-mass-selected population.

It is interesting that the outflow fraction of spectra with blueshifted Fe II absorption is much less than 100%. The outflow is highest in galaxies with higher SFR and specific SFR, but overall this variation is remarkably insensitive to galaxy parameters. We argue that these outflows have a solid angle much less than 4π steradians. This geometry is reminiscent of the bipolar outflows emanating from nearby starbursts (Heckman et al. 1990).

Based on this geometrical consideration, we can describe the typical outflow properties. The de-projected outflow velocity is measured directly when our sightline is parallel to the outflow axis. If most of the galaxies have similar outflow properties, then the largest blueshifts we measure, roughly 200 km s^{-1} , characterize the typical outflow speed. Using bounds on the column density of outflowing Fe II, the mass loss rates in the warm phase are comparable to the average SFR for favorable but plausible assumptions about the launch radius, ionization fraction, and depletion. If these SFR's persist for $\sim 1 \text{ Gyr}$, then the low-ionization outflows would remove roughly a few by $10^{10} M_{\odot}$ of warm gas, a significant baryonic mass.

The most surprising aspect of this work was the discovery of 9 galaxies with robust redshifts of low-ionization metals lines. Since these galaxies do not have unusual properties, the inflows are likely a common property of blue galaxies at $z \sim 1$. These infalling streams subtend a small solid angle, have typical velocities up to $100\text{--}200 \text{ km s}^{-1}$ (in two-component fits) and present cross-sections with radii of at least 30 kpc, and share the ro-

¹⁶ The galaxies in our LRIS sample that show redshifted Fe II absorption do not have the spectral signatures of K+A galaxies nor the colors of green-valley galaxies. They are normal blue cloud galaxies and are not post-starburst galaxies.

tation of the gas disk. Their hydrogen column density is not constrained because their metallicity is not known; but we can say that for metallicities in the range of 1 to $0.1 Z_{\odot}$ these streams would have total hydrogen gas columns of $\log N(H) (\text{cm}^{-2}) > 18.9$. These flows may originate from tidal forces generated by galaxy interactions or multiphase cooling of hot halo gas; but such models need to be projected into the quantities we observe in order to test these explanations. We emphasize that aside from metallicity, the properties of these inflows are consistent with recent predictions for cold flows of accreting gas; and the metallicity of cold flows within a few tens of kpc of the galaxy is not a robustly modeled parameter in our opinion due to possible mixing of primordial inflow and recycled wind material.

This research was supported by the National Science Foundation through grants AST-0808161 and AST-

1109288 (CLM), the David & Lucile Packard Foundation (AES and CLM), the Alfred P. Sloan Foundation (ALC), and a Dissertation Year Fellowship at UCLA (KK). We are grateful to the DEEP2 and AEGIS teams for providing both the galaxy sample and ancillary data on galaxy properties. We thank Donald Marolf, Andrey Kravtsov, Norman Murray, Dawn Erb, and Nicolas Bouché for discussions that improved this work. The Aspen Center for Physics provided a stimulating environment for completing much of the writing; and this research was partially supported by the National Science Foundation under Grant No. NSF PHY05-51164. We also wish to recognize and acknowledge the highly significant cultural role that the summit of Mauna Kea has always had within the indigenous Hawaiian community. It is a privilege to be given the opportunity to conduct observations from this mountain.

Facilities: Keck

APPENDIX

OUTFLOW FRACTION CALCULATION

As an example of how to calculate the outflow fraction, or more precisely the fraction of spectra with blueshifted resonance absorption, from data, we will use the results of our single-component fitting to the Fe II series of absorption lines. For each spectrum, the fitted Doppler shift, V_1 , and its uncertainty, δV_1 , describe the mean and standard deviation of the distribution of Doppler shifts that would be obtained after many observations.

Let $P_i(V \leq V_{crit})$ represent the probability that the absorption lines in a particular spectrum have a Doppler shift bluer than V_{crit} . The probability, $P_i(V \leq V_{crit})$, is the fractional area of this distribution with Doppler shifts $V \leq V_{crit}$. Since this distribution is well described by a Gaussian function of width $\sigma \equiv \delta V_1$ (Section 3.1), we simply compute $P_i(V \leq V_{crit})$ from an expression closely related to the normal error integral.

The expression for the entire integral depends on the relation of V_{crit} and V . We adopt a sign convention that outflow velocities are negative. When a spectrum has a low Doppler shift relative to the outflow threshold, $V_{crit} \leq V_1$, the chance that the true value of the Doppler shift is faster than V_{crit} is small and given by

$$P_i(V \leq V_{crit} | V_1, \delta V_1) = 0.5 - Q. \quad (\text{A1})$$

When the fitted Doppler shift is bluer than the outflow threshold, $V_{crit} \geq V_1$, the chance that the true Doppler shift is faster than V_{crit} is much more significant; and the total integral is

$$P_i(V \leq V_{crit} | V_1, \delta V_1) = 0.5 + Q. \quad (\text{A2})$$

The function

$$Q(t) = \frac{1}{\sqrt{2\pi}} \int_0^t e^{-z^2/2} dz = \frac{1}{2} \text{erf}(t). \quad (\text{A3})$$

describes the integral over a portion of a Gaussian distribution, where we have defined the dimensionless variable t as

$$t \equiv |V_{crit} - V_1| / \delta V_1. \quad (\text{A4})$$

For each discrete value of the threshold velocity, we compute the outflow fraction by adding the outflow probabilities $P_i(V \leq V_{crit})$ of all the spectra. We normalize this sum by the number of spectra, N_{spec} to obtain the outflow fraction

$$P_{out}(V_{crit}) = N_{spec}^{-1} \sum_{i=1}^{N_{spec}} P_i(V \leq V_{crit}). \quad (\text{A5})$$

The probability of finding a Doppler shift redder than V_{crit} is $1 - P_{out}$. For positive values of V_{crit} , the fraction of spectra with $V > V_{crit}$ obtained from $1 - P_{out}$ describes the frequency of redshifted velocities in the sample.

Error bars are calculated directly from the probability distribution. For a sample of N_{spec} objects, we compute the probability of finding 0, 1, 2, ..., $N_{spec} - 1$, N_{spec} objects with $V \leq V_{crit}$. In practice, our code uses a subroutine that starts with the first spectrum in the list, calculates the probability of finding 0 or 1 objects with $V_1 \leq V_{crit}$, and then proceeds to calculate probabilities for larger samples in an iterative fashion advancing through lists of 2, 3, 4, ... objects until the probabilities are obtained for the full list of N_{spec} objects. The sum of the first $i + 1$ values in this sequence yields the cumulative probability that the number of outflows with $V_1 \leq V_{crit}$ is less than or equal to N_i , where $i = 0$ to N_{spec} . The boundaries of the 68.27% confidence interval are found by interpolating between the N_i values to estimate the number of spectra where the cumulative probability that $V_1 \leq V_{crit}$ is 0.1587 (lower bound) and 0.8413 (upper bound).

REFERENCES

- Behroozi, P. S., Conroy, C., & Wechsler, R. H. 2010, *ApJ*, 717, 379
- Bell, E. F. et al. 2003, *ApJS*, 149, 289
- Bell, E. F. et al. 2005, *ApJ*, 625, 23
- Bouché, N. et al. 2006, *MNRAS*, 371, 495
- Bouché, N. et al. 2010, *ApJ*, 718, 10001
- Brooks, A. M. et al. 2009, *ApJ*, 694, 396
- Bundy, K. et al. 2006, *ApJ*, 651, 120
- Bregman, J. N. 1980, *ApJ*, 236, 577
- Chabrier, G. 2003, *PASP*, 115, 763
- Chen, Y.-M. et al. 2010, *AJ*, 140, 445
- Chevalier, R. A. & Clegg, A. W. 1985, *Nature*, 317, 44
- Churchill, C. et al. 2003, *AJ*, 125, 98
- Coil, A. L. et al. 2008, *ApJ*, 672, 153
- Coil, A. L. et al. 2011, *ApJ*, 743, 46
- Cooper, J. et al. 2008, *ApJ*, 674, 157
- Cooper, J. et al. 2009, *ApJ*, 703, 330
- Cresci, G. et al. 2009, *ApJ*, 697, 115
- Croton, D. J. et al. 2006, *MNRAS*, 365, 11
- Davé, R., Oppenheimer, B. D., & Finlator, K. 2011a, *MNRAS*, 415, 11
- Davé, R., Finlator, K., & Oppenheimer, B. D. 2011b, *MNRAS*, 416, 1354
- Davé, R. Finlator, K., & Oppenheimer, B. D. 2012, *MNRAS*, 421, 98
- Davis, M. et al. 2003, *SPIE*, 4834, 161
- Davis, M. et al. 2007, *ApJ*, 660, L1
- De Young, D. S., & Heckman, T. M. 1994, *ApJ*, 431, 598
- Dekel, A. et al. Birnboim, Y. 2006, *MNRAS*, 368, 2
- Dekel, A. et al. 2009a, *Nature*, 457, 451
- Dekel, A. et al. 2009b, *ApJ*, 703, 785
- Elbaz, D. et al. 2007, *A&A*, 468, 33
- Ellison, S., et al. 2000, *AJ*, 120, 1175
- Erb, D. K. et al. 2006, *ApJ*, 644, 813
- Erb, D. K. et al. 2012, submitted to *ApJ*
- Faber, S. M. 2007, *ApJ*, 665, 265
- Faucher-Giguère, C.-A. & Kereš, D. 2011, *MNRAS*, 412, L118
- Fumagalli, M. et al. 2011, *MNRAS*, 418, 1796
- Fujita, A. et al. 2009, *ApJ*, 698, 693
- Goerdt, T. et al. 2012, *arXiv1205.2021*
- Granato, G. L. et al. 2004, *ApJ*, 600, 580
- Heckman, T. M. et al. 1990, *ApJS*
- Heckman, T. M. et al. 2000, *ApJS*, 129, 493
- Heckman, T. M. 2002, *ASP Conference Series 254: Extragalactic Gas at Low Redshift*, 292
- Hong, S. et al. 2010, *arXiv:1008.4242*
- Hopkins, A. M. & Beacom, J. F. 2006, *ApJ*, 651, 142
- Hopkins, P. F., Quataert, E., & Murray, N. 2012, *MNRAS*, 421, 3522
- Hopkins, P. F. et al. 2007, *ApJ*, 659, 976
- Houck, J. C. & Bregman, J. N. 1990, *ApJ*, 352, 506
- Jones, T., Stark, D. P., & Ellis, R. S. 2012, *ApJ*, 751, 51
- Kauffmann, G., et al. 2003, *MNRAS*, 346, 1055
- Kennicutt, R. C. 1998, *ARA&A*, 36, 189.
- Kereš, D. et al. 2005, *MNRAS*, 363, 2
- Kereš, D. et al. 2009a, *MNRAS*, 396, 2332
- Kereš, D. & Hernquist, L. 2009b, *MNRAS*, 396, 2332
- Kimm, T. et al. 2011, *MNRAS*, 413, 51
- Kobulnicky, H. A. & Gebhardt, K. 2000, *AJ*, 119, 1608
- Lilly, S. J. et al. 1996, *ApJ*, 460, L1
- Lu, L. 1991, *ApJ*, 379, 99
- Madau, P. et al. 1996, *MNRAS*, 283, 1388
- Marchesini, D. et al. 2009, *ApJ*, 701, 1765
- Marinacci, F. et al. 2011, *MNRAS*, 415, 1534
- Marlowe, A. et al. 1997, *ApJS*, 112, 285
- Martin, C. L. 1999, *ApJ*, 513, 156
- Martin, C. L. 2005, *ApJ*, 621, 227
- Martin, C. L. Kobulnicky, H. A. & Heckman, T. M. 2002, *ApJ*, 574, 663
- Martin, C. L. et al. 2010, *ApJ*, 721, 174
- McGaugh, S. S. et al. 2010, *ApJ*, 708, 14
- Mendez, A. J. et al. 2011, *ApJ*, 736, 110
- Meyer, D. M. & York, D. G. 1987, *ApJ*, 315, 5
- Morton, D. C. 2003, *ApJS*, 149, 205
- Mostek, N. et al. 2012, *ApJ*, 746, 124
- Nestor, D. et al. 2006, *ApJ*, 643, 75
- Newman, J. A. et al. 2012, *arXiv:1203.3192*
- Noeske, K. G. 2007a, *ApJ*, 660, L43
- Noeske, K. G. 2007b, *ApJ*, 660, L47
- Ocvirk, P., Pichon, C., Teyssier, R. 2008, *MNRAS*, 390, 1326
- Oke, J.B., et al. 1995, *PASP*, 107, 375
- Oppenheimer, B. et al. 2008, *ApJ*, 679, 1574
- Oppenheimer, B. et al. 2010, *MNRAS*, 406, 2325
- Oppenheimer, B. et al. 2012, *ApJ*, 420, 829
- Pettini, M. et al. 2000, *ApJ*, 528, 96
- Pettini, M. et al. 2001, *ApJ*, 554, 981
- Phillips, A. C., Miller, J., Cowley, D., Wallace, V. 2006, *SPIE*, 6269, 56
- Prochaska, J. X., Kasen, D., & Rubin, K. 2011, *ApJ*, 734, 24
- Press, W. H., Teukolsky, S. A., Vetterling, W. T., & Flannery, B. P. 1992, *Numerical Recipes*, Press Syndicate of the Cambridge University (New York, NY)
- Rix, S. A. et al. 2004, *ApJ*, 615, 98
- Rix, H.-W. et al. 1997, *MNRAS*, 285, 229
- Rubin, K. H. R. et al. 2012, *ApJ*, 747, 26
- Rubin, K. H. R. et al. 2011a, *ApJ*, 728, 55
- Rubin, K. H. R. et al. 2010b, *ApJ*, 719, 1503
- Rubin, K. H. R. et al. 2010a, *ApJ*, 712, 574
- Rupke, D. et al. 2005, *ApJS*, 160, 115
- Savage, B. D. & Sembach, K. R. 1996, *ARA&A*, 34, 279
- Scannapieco, E. & Oh, S. P. 2004, *ApJ*, 608, 62
- Schaye, Y., et al. 2003, *ApJ*, 596, 768
- Schawinski, K. et al. 2007, *MNRAS*, 382, 1415
- Schwartz, C. M. & Martin, C. L. 2004, *ApJ*, 610, 201
- Schwartz, C. M. et al. 2006, *ApJ*, 646, 858
- Shapley, A. E. et al. 2003, *ApJ*, 588, 65
- Shapley, A. E. et al. 2006, *ApJ*, 651, 688
- Simcoe, R. A. 2011, *ApJ*, 738, 159
- Simcoe, R. A. et al. 2006, *ApJ*, 637, 648
- Somerville, R. S. et al. 2008, *MNRAS*, 391, 481
- Songaila, A., & Cowie, L. L. 1996, *AJ*, 112, 335
- Spitzer, L. Jr., 1978, *Physical Processes in the Interstellar Medium*, John Wiley & Sons, Inc., (New York, NY)
- Springel, V., Di Matteo, T., & Hernquist, L. 2005, *MNRAS*, 361, 776
- Steidel, C. S. et al. 2003, *ApJ*, 592, 728
- Steidel, C. S. et al. 2004, *ApJ*, 604, 534
- Steidel, C. S. et al. 2010, *ApJ*, 717, 289
- Stewart, K. R. et al. 2011b, *ApJ*, 738, 39
- Stewart, K. R. et al. 2011a, *ApJ*, 735, 1
- Tinker, J. L. & Chen, H.-W. 2008, *ApJ*, 679, 1218
- Tremonti, C. et al. 2004, *ApJ*, 613, 898
- Tremonti, C. et al. 2007, *ApJ*, 663, 77
- Weiner, B. J. et al. 2006, *ApJ*, 653, 1027
- Weiner, B. J. et al. 2009, *ApJ*, 692, 187
- Willmer, C. N. 2006 *ApJ*, 647, 853
- van de Voort, F. et al. 2011a, *MNRAS*, 414, 2458
- van de Voort, F. et al. 2011b, *MNRAS*, 415, 2782
- Yan, R. et al. 2009, *MNRAS*, 398, 735
- Zhang, D. & Thompson, T. A. 2010, *arXiv:1005.4691*

TABLE 1
KECK/LRIS OBSERVATIONS

Field	R.A. (J2000.0)	Decl. (J2000.0)	Mask PA ($^{\circ}$)	Grism / Grating (1 mm^{-1})	Dichroic	Conditions Cloud Cover & Seeing($''$)	Exposure Time LRIS-B/LRIS-R (s)	Date
msc42_1	02 28 56.8	+00 33 39	120.0	400 / 800	d680	Clear to Mostly Cloudy & 0.9-1.6 ^b	11340 / 11100	2007 Oct 6-7
msc42_5	02 30 35.6	+00 28 17	143.0	400 / 800	d680	Mostly Cloudy to Light Cirrus & 0.7-0.9 ^c	26883 / 25400	2008 Sep 28-29
msc12_d	14 17 09.8	+52 31 18	165.0	400 / 800	d680	Clear to Mostly Cloudy & 0.6-2.0	18500 / 18000	2008 June 5-6
msc12_8	14 18 19.4	+52 34 33	5.0	400 / 800	d680	Clear to Partly Cloudy & 0.6-2.0	28800 / 26940	2009 June 18-21 ^a
msc12_ee	14 18 46.8	+52 38 59	170.0	600 / 600	d560	Clear to Partly Cloudy & 0.6-2.0	11520 / 10800	2009 June 18-21 ^a
msc22_bb	16 51 09.2	+34 58 15	25.0	600 / 600	d560	Clear to Mostly Cloudy & 0.6-2.0	18400 / 17950	2008 June 5-6
msc22_6	16 51 28.8	+34 48 09	60.0	400 / 800	d680	Clear to Partly Cloudy & 0.6-2.0	30760 / 23100	2009 June 18-21 ^a
msc32_aa	23 29 19.5	+00 07 38	82.0	600 / 600	d560	Mostly Cloudy to Light Cirrus & 0.7-0.9	11070 / 10800	2008 Sep 28-29
msc32_1	23 30 18.9	+00 12 53	80.0	400 / 800	d560	See Conditions Above ^{b,c}	25810 / 24182	2007 Oct 6-7 & 2008 Sep 28-29

^aThe red spectra obtained in 2009 June were obtained with a new detector. Shorter exposure times were used for individual frames due to high cosmic ray rate, but the high density of cosmic rays still compromised the final sensitivity.

TABLE 2
PROPERTIES OF COMPOSITE SPECTRA

Feature Spectrum (1)	V_1 (Fe II) (km s ⁻¹) (2)	EW(λ 2374) (Å) (3)	V_{max} (Mg II) (km s ⁻¹) (4)	EW(λ 2796) (Å) (5)
Lowest Mass ($8.85 \leq \log(M_*/M_\odot) < 9.85$)	-28 ± 8	1.26	-649 ± 86	0.61 ± 0.01
Intermediate Mass ($9.85 \leq \log(M_*/M_\odot) < 10.35$)	-32 ± 6	1.47	-770 ± 103	1.40 ± 0.03
Highest Mass ($10.35 \leq \log(M_*/M_\odot) \leq 11.29$)	-23 ± 8	1.59	-713 ± 119	1.63 ± 0.05
Bluest ($0.189 \leq U - B < 0.519$)	-32 ± 8	1.31	-693 ± 86	0.72 ± 0.02
Bluer ($0.519 \leq U - B < 0.662$)	-27 ± 6	1.48	-649 ± 91	1.17 ± 0.02
Blue ($0.662 \leq U - B \leq 0.907$)	-26 ± 7	1.52	-888 ± 173	1.85 ± 0.07
Lowest Luminosity ($-17.67 \geq M_B - 5 \log h > -20.03$)	-23 ± 9	1.19	-666 ± 88	0.72 ± 0.02
Intermediate Luminosity ($-20.03 \geq M_B - 5 \log h > -20.79$)	-18 ± 7	1.56	-667 ± 88	1.08 ± 0.01
Highest Luminosity ($-20.79 \geq M_B - 5 \log h > -22.19$)	-39 ± 6	1.65	-782 ± 92	1.79 ± 0.03
Lowest SFR ($0.86 \leq SFR(M_\odot \text{ yr}^{-1}) < 12.24$)	26 ± 10	1.48	-629 ± 104	0.81 ± 0.04
Highest SFR ($12.24 \leq SFR(M_\odot \text{ yr}^{-1}) < 97.81$)	-38 ± 8	1.47	-755 ± 91	1.88 ± 0.02
Lowest sSFR ($1.00 < sSFR^{-1}(Gyr) \leq 15.08$)	19 ± 10	1.55	-779 ± 136	1.59 ± 0.06
Highest sSFR ($0.178 < sSFR^{-1}(Gyr) \leq 1.00$)	-24 ± 9	1.41	-610 ± 81	0.92 ± 0.02
3 σ FeII Outflow	-119 ± 6	1.47	-901 ± 99	1.59 ± 0.02
3 σ FeII Inflow	95 ± 8	1.89	-559 ± 113	1.25 ± 0.07

NOTE. — Col. 1 – Composite spectrum. Col. 2 – Doppler shift of the Fe II absorption measured as described in Section 3.3. Col. 3 – Equivalent width of the Fe II λ 2374 absorption trough. Col. 4 – Maximum blueshift, V_{max} , of Mg II λ 2796 absorption measured as described in Section 3.4. Col. 5 – Equivalent width of the Mg II λ 2796 trough from 0 to V_{max} .

TABLE 3
CORRELATION COEFFICIENT AND SIGNIFICANCE AMONG PROPERTIES OF INDIVIDUAL GALAXIES

Quantity	$V_1(\text{Fe II})^a$	$W(\lambda 2374)^a$	$W(\lambda 2796)^c$	V_{max}^c	$W2796/W2374$
M_*	0.010 (1.28)	0.044 (0.56)	0.320 (1.87)	-0.305 (1.78)	0.377 (2.20)
$M_B - 5 \log h$	0.019 (0.25)	-0.050 (0.64)	-0.338 (1.97)	0.097 (0.56)	-0.250 (1.46)
$U - B$	0.116 (1.48)	0.020 (0.25)	0.443 (2.58)	-0.205 (1.20)	0.462 (2.69)
z	-0.068 (0.88)	0.196 (2.50)	0.066 (0.38)	0.143 (0.84)	-0.139 (0.81)
SNR	-0.024 (0.31)	-0.081 (1.03)	-0.165 (0.96)	-0.059 (0.34)	-0.148 (0.86)
$V_1(\text{Fe II})$	n/a	0.159 (2.03)	-0.1421 (0.83)	0.160 (0.93)	-0.020 (0.11)
$W(\lambda 2374)$	0.159 (2.03)	n/a	0.451 (2.63)	-0.033 (0.19)	-0.129 (0.75)
$V_{max}(\text{Mg II})$	0.160 (0.93) ^c	-0.033 (0.19)	-0.451 (2.63)	n/a	-0.332 (1.94)
$W(\lambda 2796)$	-0.142 (0.83) ^c	0.451 (2.63)	n/a	-0.451 (2.63)	0.774 (4.51)
SFR	-0.138 (0.92) ^b	-0.067 (0.44) ^b	0.086 (0.19) ^d	0.257 (0.57) ^d	0.143 (0.32)
sSFR	-0.377 (2.50) ^b	0.116 (0.77) ^b	-0.257 (0.58) ^d	0.086 (0.19) ^d	-0.314 (0.70)

NOTE. — We computed the Spearman rank-order correlation coefficient, r_S , between the continuum S/N ratio near Fe II and various galactic properties. To determine whether a significant correlation was present, we examined the variance in the sum-squared difference of ranks, D , which is approximately normally distributed as described in chapter 14 of Press et al. (1992). The value in parentheses is the number of standard deviations from the null hypothesis that the quantities are uncorrelated.

^aSample of 165 with measured FeII Doppler shift V_1 .

^bSample of 45 with measured FeII Doppler shift V_1 and extinction-corrected, ultraviolet SFR.

^cSample of high S/N ratio spectra with measured maximum Mg II blueshift V_{max} .

^dSample of high S/N ratio spectra with measured $V_{max}(\text{Mg II})$ and extinction-corrected, ultraviolet SFR.

TABLE 4
PROPERTIES OF GALAXIES WITH NET Fe II DOPPLER SHIFTS

Object	Grism ($l\text{ mm}^{-1}$)	SNR	Redshift Source	z	$M_B - 5 \log h$ (AB mag)	U-B	$\log M_*$ (M_\odot)	SFR ($M_\odot\text{ yr}^{-1}$)
(1)	(2)	(3)	(4)	(5)	(6)	(7)	(8)	(9)
12008197	400	12.2	L	0.9802	-21.19	0.804	10.63 [†]	98
12008550	400	9.86	L	1.3024	-21.22	0.620	10.08 [†]	25
12011836	400	9.38	L	0.9270	-19.90	0.579	10.26 [†]	14
12012777	400	11.68	L	1.2742	-21.06	0.516	10.11 [†]	23
12013242	400	8.83	L	1.2867	-21.31	0.450	10.19	26
12011428*	400	4.6	L	1.2840	-19.87	0.180	9.65	9
12015177	600	5.3	L	0.9860	-20.23	0.487	9.69	12
12016019*	400	11.57	L	1.0846	-20.71	0.622	10.03 [†]	19
12019542	600	3.73	D	1.2784	-21.68	0.705	10.40 [†]	40
12019962*	400	10.1	L	0.6444	-19.22	0.458	9.77 [†]	2
12019996*	400	7.36	L	1.2812	-21.71	0.634	10.67 [†]	43
12100420*	400	8.60	L	1.1995	-20.63	0.601	10.01 [†]	10
22004858*	400	15.00	L	1.2686	-21.84	0.624	10.54	...
22005216	400	9.27	L	0.9130	-19.49	0.556	9.59	...
22005270*	400	10.57	L	0.8308	-20.38	0.710	10.40	...
22006172	400	10.65	L	0.8328	-21.10	0.707	10.65	...
22006207	400	9.42	L	1.2709	-20.59	0.419	9.88	...
22029066	600	10.45	L	0.7852	-21.59	0.891	11.29 [†]	...
22029224	600	8.66	L	0.8603	-20.90	0.611	10.27	...
22036854	600	7.29	L	0.9373	-20.85	0.564	10.32	...
22036912	600	6.66	L	0.8099	-21.02	0.864	10.86	...
32010773	600	9.23	L	0.8039	-19.91	0.234	9.60 [†]	...
32011098	600	5.01	L	0.9561	-20.22	0.546	9.77 [†]	...
32011099	600	6.51	L	0.8832	-20.06	0.492	9.80	...
32011192	600	9.51	L	0.8478	-20.60	0.587	10.07 [†]	...
32011682	600	8.79	L	0.8359	-20.36	0.511	10.23 [†]	...
32016857	600	8.32	L	0.9391	-20.81	0.440	9.81 [†]	...
32017112	600	5.85	L	1.0084	-20.89	0.665	10.23 [†]	...
32020468*	400	3.16	L	1.2355	-21.00	0.734	10.28 [†]	...
32022156	600	4.60	L	1.0434	-20.70	0.580	10.10 [†]	...
42006781	400	10.98	D	1.2859	-20.74	0.546	9.68 [†]	...
42006915	400	25.09	L	0.8945	-20.55	0.386	10.50 [†]	...
42014101	400	8.39	L	0.7494	-20.47	0.899	10.94 [†]	...
42014154	400	9.75	L	0.8427	-19.40	0.465	9.77 [†]	...
42014585	400	8.17	D	1.2705	-20.91	0.588	10.18	...
42014618	400	17.64	L	1.0130	-20.37	0.592	9.81	...
42014718	400	9.21	L	1.1904	-21.27	0.692	10.85 [†]	...
42014732	400	16.01	L	0.7502	-19.40	0.453	9.50 [†]	...
42021266	400	11.66	L	0.9765	-19.63	0.616	9.50	...
42022173	400	8.15	D	1.3112	-20.25	0.324	9.68	...
42022307	400	20.72	D	1.2595	-21.43	0.466	10.22	...
42026243	400	3.30	L	1.3456	-21.66	0.667	10.88 [†]	...
42033991	400	6.48	L	0.8714	-20.13	0.392	9.94 [†]	...
42006875*	400	19.18	L	0.8696	-21.10	0.602	10.50 [†]	...

NOTE. — (1) - Object identification from DEEP2. The Fe II absorption in these spectra is Doppler shifted (relative to the galaxy) at a significance level greater than 3σ . Inflows (redshifts) are denoted by *; the objects 22028473 and 22036194 have been dropped per the discussion in § 5.1. (2) - Blue grism where 400 l mm^{-1} and 600 l mm^{-1} imply FWHM of 435 km s^{-1} and 282 km s^{-1} , respectively. (3) - Continuum SNR between 2400 and 2500 Å. (4) - Source of redshift. The flag L/D indicates (L)RIS (the spectra presented here) or (D)EIMOS, DEEP2 redshift, respectively. (5) - Redshift. (6) - DEEP2 absolute magnitude (Willmer et al. 2006). (7) - DEEP2 color (Willmer et al. 2006). (8) - Stellar mass from SED fitting (Bundy et al. 2006). Galaxies with an SED fit that includes K-band photometry (most certain) are denoted by [†]; the other fits are based on BRI photometry. (9) - Star formation rate derived from dust-corrected UV continuum luminosity. Values have been converted to a Chabrier initial mass function.

TABLE 5
OUTFLOW PROPERTIES

Object	W(2374) (Å)	W(2261) (Å)	$\log N(Fe^+)$ (cm^{-2})	V_1 ($km\ s^{-1}$)	b_{ISM} ($km\ s^{-1}$)	V_{DOP} ($km\ s^{-1}$)	$\log N_{ISM}(Fe^+)$ (cm^{-2})	$\log N_{DOP}(Fe^+)$ (cm^{-2})	$V_{max}(\lambda 2374)$ ($km\ s^{-1}$)	$V_{max}(\lambda 2796)$ ($km\ s^{-1}$)
(1)	(2)	(3)	(4)	(5)	(6)	(7)	(8)	(9)	(10)	(11)
12008197	1.21 ± 0.23	0.21	14.89 - 15.75	-62 ± 19	126	-93 ± 43	14.80 - 15.34	14.58 - 15.93	...	-466 ± 120
12008550	1.05 ± 0.19	0.17	14.83 - 15.66	-145 ± 23	77	-322 ± 135	14.69 - 15.27	14.32 - 15.79	-547 ± 93	
12011836	2.14 ± 0.32	0.27	15.14 - 15.86	-128 ± 21	114	-465 ± 142	15.00 - 15.65	14.42 - 15.01	-697 ± 117	-667 ± 94
12012777	2.13 ± 0.19	0.18	15.13 - 15.68	-217 ± 13	95	-443 ± 70	15.07 - 15.89	14.79 - 15.59	-704 ± 122	-909 ± 146
12013242	1.14 ± 0.23	0.24	14.86 - 15.81	-73 ± 22	121	-97 ± 45	14.89 - 15.48	14.78 - 15.81
12015177	2.34 ± 0.32	0.33	15.17 - 15.94	-101 ± 18	91	-106 ± 49	14.95 - 15.64	14.72 - 15.77	-418 ± 51	...
12019542	0.72 ± 0.30	0.39	14.66 - 16.02	-183 ± 60^4	69	-311 ± 273	14.51 - 15.04	14.51 - 15.04
22005216	0.98 ± 0.26	0.25	14.80 - 15.82	-106 ± 28	59	-450 ± 146	14.90 - 15.76	14.20 - 14.66	...	-504 ± 56
22006172	1.57 ± 0.28	0.27	15.00 - 15.86	-112 ± 21	118	-95 ± 47	14.84 - 15.41	14.80 - 15.80	-588 ± 178	-514 ± 128
22006207	0.76 ± 0.15	0.16	14.69 - 15.63	-199 ± 39	76	-34 ± 35	14.57 - 15.11	14.68 - 16.06	-487 ± 84	-693 ± 94
22029066	1.85 ± 0.20	0.27	15.07 - 15.86	-62 ± 16	152	-209 ± 46	14.93 - 15.49	> 14.05	-396 ± 115	-919 ± 117
22029224	1.09 ± 0.19	0.22	14.84 - 15.77	-69 ± 16	117	-146 ± 53	14.81 - 15.37	14.37 - 14.94	...	-450 ± 39
22036854	2.08 ± 0.24	0.24	15.12 - 15.81	-91 ± 14	58	-121 ± 37	14.91 - 15.81	14.55 - 15.30	-444 ± 46	...
22036912	0.84 ± 0.21	0.34	14.73 - 15.96	-86 ± 16	167	-238 ± 87	14.80 - 15.29	14.14 - 14.49	-297 ± 53	-653 ± 58
32010773	0.63 ± 0.17	0.19	14.60 - 15.70	-197 ± 46	45	-189 ± 126	14.45 - 15.03	14.13 - 14.60	-511 ± 95	-703 ± 43
32011098	0.59 ± 0.31	0.33	14.58 - 15.94	-89 ± 29	87	-78 ± 101	14.54 - 15.04	14.56 - 15.57
32011099	1.79 ± 0.25	0.23	15.06 - 15.79	-46 ± 13	72	-97 ± 24	15.06 - 16.12	14.65 - 15.30	-356 ± 69	-463 ± 105
32011192	1.85 ± 0.19	0.22	15.07 - 15.77	-154 ± 9	97	-154 ± 38	14.96 - 15.65	14.74 - 15.30	-527 ± 86	-739 ± 74
32011682	1.30 ± 0.20	0.23	14.92 - 15.79	-85 ± 11	96	-246 ± 60	14.90 - 15.55	14.18 - 14.68	-317 ± 71	-521 ± 62
32016857	0.88 ± 0.18	0.20	14.75 - 15.73	-91 ± 15	97	-227 ± 82	14.75 - 15.32	14.42 - 15.53	-297 ± 84	...
32017112	1.25 ± 0.25	0.30	14.90 - 15.90	-80 ± 18	99	-255 ± 106	14.80 - 15.38	14.24 - 14.88
32022156	0.95 ± 0.34	0.43	14.78 - 16.06	-180 ± 48	74	-318 ± 182	14.82 - 15.49	14.41 - 14.98	-355 ± 42	-436 ± 27
42006781	2.07 ± 0.17	0.15	15.12 - 15.60	-70 ± 13	59	-143 ± 28	15.00 - 16.11	14.06 - 14.42	-565 ± 77	-495 ± 68
42006915	1.29 ± 0.10	0.097	14.92 - 15.41	-76 ± 10	206	-322 ± 75	14.67 - 15.08	13.91 - 14.03	-621 ± 117	-576 ± 91
42014101	1.08 ± 0.35	0.32	14.84 - 15.93	-150 ± 38	107	-281 ± 251	14.65 - 15.17	14.48 - 15.29	-514 ± 68	-480 ± 66
42014154	0.84 ± 0.22	0.25	14.73 - 15.82	-105 ± 30	63	-315 ± 163	14.77 - 15.46	13.93 - 14.42
42014585	1.63 ± 0.27	0.27	15.02 - 15.86	-177 ± 30	61	-297 ± 85	14.96 - 15.94	14.55 - 15.20	-579 ± 155	-456 ± 47
42014618	1.29 ± 0.14	0.15	14.92 - 15.60	-76 ± 13	121	-115 ± 33	14.83 - 15.39	14.43 - 15.67	-548 ± 107	...
42014718	2.06 ± 0.31	0.30	15.12 - 15.90	-156 ± 19	199	-219 ± 77	14.96 - 15.49	14.84 - 15.90	-712 ± 216	-651 ± 128
42014732	0.91 ± 0.17	0.16	14.76 - 15.63	-81 ± 26	79	-52 ± 43	14.59 - 15.13	14.47 - 15.33	-450 ± 82	...
42021266	1.06 ± 0.20	0.19	14.83 - 15.70	-108 ± 24	76	-388 ± 152	14.75 - 15.37	14.28 - 15.26	-590 ± 163	...
42022173	0.81 ± 0.21	0.23	14.71 - 15.79	-134 ± 27	106	-125 ± 85	14.67 - 15.20	14.70 - 15.85
42022307	1.15 ± 0.09	0.10	14.87 - 15.43	-146 ± 10	165	-381 ± 79	14.71 - 15.18	14.20 - 14.66	-554 ± 62	-529 ± 50
42026243	...	0.70	... - 16.27	-302 ± 38	93	-476 ± 201	15.17 - 16.22	15.03 - 16.29	...	-843 ± 135
42033991	1.39 ± 0.46	0.40	14.95 - 16.03	-139 ± 41	132	-369 ± 319	14.69 - 15.19	14.52 - 15.36	-466 ± 136	...

NOTE. — (1) DEEP2 survey identification. (2) Rest-frame equivalent width of Fe II 2374 absorption from direct integration of the trough. Error estimated from bootstrap resampling. (3) Upper limit (1σ) on Fe II 2261 equivalent width. Computed from an assumed linewidth that is twice the FWHM of the line response function and the continuum S/N ratio. (4) Limits on Fe II column density. For optically thin absorption, the linear portion of the curve-of-growth gives $N(Fe\ II) = 6.40 \times 10^{14} cm^{-2} W_{2374}$, which we adopt as a lower bound. We derive an upper bound, $N(Fe\ II) = 9.06 \times 10^{15} cm^{-2} W_{2261}$, by taking the 3σ upper limit on the Fe II 2261 equivalent width. (5) Doppler shift of the single velocity component model fitted to Fe II absorption as described in Section 3.3. (6) Doppler parameter of the systemic component in the two-component fits to the Fe II series. We adopt characteristic velocities of gas in the galaxy as probed by cooling radiation from H II regions. Specifically, we require the FWHM of the absorption optical depth profile match that of [OII] measured previously by Weiner et al. (2006), which gives $b_{sys} = \sqrt{2}\sigma([OII])$. (7) Doppler shift of the Doppler component fitted to Fe II lines in two-component model described in Section 3.3.2. (8) Limits on Fe II column density of ISM component in two-component fits. The model line profile for Fe II 2261 and 2374 were integrated and the above formulae, from comment #4, applied. (9) Limits on Fe II column density of Doppler component in two-component fits. The model line profile for Fe II 2261 and 2374 were integrated and the above formulae, from comment #4, applied. (10) Velocity of maximum Fe II 2374 absorption for $I + \delta(I) = 1$. (11) Velocity of maximum Mg II 2796 absorption for $I + \delta(I) = 1$.

TABLE 6
INFLOW PROPERTIES

Object	W(2374)	W(2260)	$\log N(Fe^+)$	V_1	b_{ISM}	V_{DOP}	$\log N_{ISM}(Fe^+)$	$\log N_{DOP}(Fe^+)$	$V_{max}(\lambda 2374)$	$V_{max}(\lambda 2382)$
(1)	(\AA) (2)	(\AA) (3)	(cm^{-2}) (4)	(km s^{-1}) (5)	(km s^{-1}) (6)	(km s^{-1}) (7)	(cm^{-2}) (8)	(cm^{-2}) (9)	(km/s) (10)	(km/s) (11)
12011428	2.14 ± 0.48	0.44	15.1 - 16.0	154 ± 32	86	392 ± 124	15.14 -16.19	14.71 -15.49	416 ± 0.9	523 ± 0.1
12016019	2.44 ± 0.20	0.19	15.1 - 15.7	48 ± 14	97	258 ± 40	15.17 -16.15	> 13.58	655 ± 34	723 ± 0.6
12019962	1.88 ± 0.34	0.32	15.0 - 15.9	104 ± 31	113	122 ± 97	14.68 -15.20	13.86 -15.15	621 ± 9	472 ± 1
12019996	1.69 ± 0.31	0.30	15.0 - 15.9	117 ± 24	158	386 ± 138	14.92 -15.47	14.56 -15.57	510 ± 3	577 ± 5
12100420	1.86 ± 0.28	0.26	15.0 - 15.8	71 ± 18	109	190 ± 45	15.14 -15.98	14.37 -14.82	539 ± 1	641 ± 1
22004858	1.94 ± 0.14	0.14	15.0 - 15.6	61 ± 11	151	71 ± 18	15.03 -15.63	14.76 -15.53	...	737 ± 2
22005270	0.98 ± 0.23	0.25	14.8 - 15.8	401 ± 43	145	505 ± 588	14.39 -14.71	14.37 -14.81	546 ± 2	724 ± 9
32020468	2.36 ± 0.69	0.62	15.1 - 16.2	123 ± 39	95	164 ± 79	15.21 -16.33	14.82 -15.97	465 ± 1	311 ± 3
42006875	1.01 ± 0.12	0.12	14.8 - 15.5	51 ± 14	62	256 ± 50	14.87 -15.66	13.86 -14.21	...	663 ± 3

NOTE. — (1) DEEP2 survey identification. (2) Rest-frame equivalent width of Fe II 2374 absorption from direct integration of the trough. Error estimated from bootstrap resampling. (3) Upper limit (1σ) on Fe II 2261 equivalent width. Computed from an assumed linewidth that is twice the FWHM of the line response function and the continuum S/N ratio. (4) Limits on Fe II column density. For optically thin absorption, the linear portion of the curve-of-growth gives $N(\text{Fe II}) = 6.40 \times 10^{14} \text{ cm}^{-2} W_{2374}$, which we adopt as a lower bound. We derive an upper bound, $N(\text{Fe II}) = 9.06 \times 10^{15} \text{ cm}^{-2} W_{2261}$, from the 3σ upper limit on the Fe II 2261 equivalent width. (5) Doppler shift of the single velocity component model fitted to Fe II absorption as described in Section 3.3. (6) Doppler parameter of the systemic component in the two-component fits to the Fe II series. We adopt characteristic velocities of gas in the galaxy as probed by cooling radiation from H II regions. Specifically, we require the FWHM of the absorption optical depth profile match that of [OII] measured previously by Weiner et al. (2006), which gives $b_{sys} = \sqrt{2}\sigma([OII])$. (7) Doppler shift of the *Doppler component* fitted to Fe II lines in two-component model described in Section 3.3.2. (8) Limits on Fe II column density of ISM component in two-component fits. The model line profile for Fe II 2261 and 2374 were integrated and the above formulae, from comment #4, applied. (9) Limits on Fe II column density of Doppler component in two-component fits. The model line profile for Fe II 2261 and 2374 were integrated and the above formulae, from comment #4, applied. (10) Velocity of maximum Fe II 2374 absorption for $I + \delta(I) = 1$. (11) Velocity of maximum Mg II 2796 absorption for $I + \delta(I) = 1$.